Nanomanufacturing of Carbon Nanocomposites for Energy Storage and Environmental Applications

By

Mengya Li

Dissertation

Submitted to the Faculty of the

Graduate School of Vanderbilt University

in partial fulfillment of the requirements

for the degree of

DOCTOR OF PHILOSOPHY

in

Mechanical Engineering

August 10, 2018

Nashville, Tennessee

Approved:

Cary L. Pint, Ph.D.

Greg Walker, Ph.D.

Leon Bellan, Ph.D.

Shihong Lin, Ph.D.

Yaqiong Xu, Ph.D.

Piran Kidambi, Ph.D.

To my dear parents, for their love, understanding, and support.

ACKNOWLEDGEMENTS

I would like to express my deepest appreciation to my PhD advisor, Dr. Cary Pint, for welcoming me to your group to start my journey in energy storage research. I couldn't have learned how to do research without your inspiration and guidance. Thanks for your support and understanding throughout my PhD. And thank you for taking so much time and efforts in helping me with publications and attitude towards research. Besides research, I also learned a lot in developing personal skills such as creativity, leadership, and communication from you. I would also like to thank my committee members: Dr. Greg Walker, Dr. Leon Bellan, Dr. Shihong Lin and Dr. Yaqiong Xu, Dr. Piran Kidambi for important and helpful feedbacks on my research which make me keep improving myself.

I would like to thank my previous and current labmates, Dr. Rachel Carter, thanks for being such a sweet friend, so grateful for your great help and support in my career development. Anna Douglas, CEO of SkyNano, thanks for baking the best desserts that always make me want to cry, and thanks for the warmest guestroom in Knoxville. Dr. Nitin Muralidharan, thanks for the introduction of all the amazing Indian food and being my gym buddy for a short while. Dr. Landon Oakes, thanks for your help and always being a nice listener. Dr. Adam Cohn, thanks for your insightful comments and all the nice jokes. Dr. Keith Share, thanks for the always positive attitude that inspires me. Kate Moyer, thanks for the great experience being neighbor in the graduate student office. Janna Eaves, for the amazingly organized party and really helpful coding techniques. Dr. Andrew Westover, thanks for introducing me to the lab and conversations in Mandarin. I would also like to thank Dr. Rizia Bardhan, for generously letting me using Raman and their lab. Thanks for my labmates-in-law, May Ou, for the most amazing time with you

and Pickle exploring Nashville and traveling around. Naiya Soetan, thanks for your help with a lot of nanoparticles synthesis. Eden Paul, thanks for the good old hang-out time. Special thanks to Dr. Anthony Hmelo, Dr. Dmitry Koktysh, and everyone else at VINSE for their help on research. Thanks for a lot of amazing people Siruo Zhao, Pengchuan Wang, and those I met at 2018 Battery Gordon Research Conference, especially Will Gent, Fufuo Ma, Jesse Ko, and any many other professors, postdocs and graduate students, who have helped me with my career. Last but not least, I would like to thank Xinnan Du, for being the best friend to share happiness and sorrow, and give me the most support since high school. And thanks to my friends Xin Zhang, Lin Yang, Yuchen Zhang, Tianjiao Wang, Chenbo Feng, Kan Li, Becca Creed, Nima Sarli, Haotian Sun, Siyuan Jiang, Jackson Meng, Rebecca Gurrola, Andria Remirez, Jie Wan, Shan Jiang, Siyang Che, Claire Marvinney, Alice Leach, Kristin Engerer and many more, it's my pleasure to meet all of you in grad school.

Finally, I would like to express my sincere appreciation to my parents, who inspired me to pursue a research career and support me for many years studying abroad. Without their understanding, I could not have overcome a lot of life barriers. Thanks for always willing to travel overseas for almost 20 hours to visit me in the past four years.

TABLE OF CONTENTS

Page

LIST OF FIGURES

Figure **Page**

LIST OF TABLES

Table **Page**

LIST OF PUBLICATIONS

Portions of this dissertation have been drawn from the following publications:

1. M. Li, R. Carter, A. P. Cohn and C. L. Pint, ” Interconnected foams of helical carbon nanofibers grown with ultrahigh yield for high capacity sodium ion battery anodes,” *Carbon*, 2016, **107**, 109-115.

2. M. Li, A. S. Westover, R. Carter, L. Oakes, N. Muralidharan, T. C. Boire, H. J. Sung and C. L. Pint, “Noncovalent Pi-Pi Stacking at the Carbon Electrolyte Interface: Controlling the Voltage Window of Electrochemical Supercapacitors,” *Acs Appl Mater Inter*, 2016, **8**, 19558-19566.

3. M. Li, R. Carter, L. Oakes, A. Douglas, N. Muralidharan and C. L. Pint, “Role of carbon defects in the reversible alloying states of red phosphorus composite anodes for efficient sodium ion batteries,” *Journal of Materials Chemistry A*, 2017, **5**, 5266-5272.

4. M. Li, R. Carter, A. Douglas, L. Oakes and C. L. Pint, “Sulfur Vapor-Infiltrated 3D Carbon Nanotube Foam for Binder-Free High Areal Capacity Lithium-Sulfur Battery Composite Cathodes,” *ACS Nano*, 2017, **11**, 4877-4884.

5. M. Li, N. Muralidharan, M. Li, R. E. Carter, N. Galioto and C. L. Pint, “Ultralow Frequency Electrochemical–Mechanical Strain Energy Harvester using 2D Black Phosphorus Nanosheets,” *ACS Energy Letters*, 2017, **2**, 1797-1803.

6. M. Li, N. Muralidharan, K. Moyer and C. L. Pint, “Solvent Mediated Hybrid 2D Materials: Black Phosphorus-Graphene Heterostructured Building Blocks Assembled for Sodium Ion Batteries,” *Nanoscale*, 2018, **10**, 10443-10449.

7. M. Li, N. Muralidharan, P. R. Kidambi and C. L. Pint, *“*Carbon Nanotube Foam for Efficient Electrochemical Removal of Chromium (VI) from Aqueous Solution*”* in preparation.

CHAPTER 1

INTRODUCTION

1.1 Motivation

Various types of carbon nanomaterials such as nanodiamonds, graphene, and carbon nanotubes have opened new frontiers in research. Arranging in different dimensions, carbon nanomaterials possess specific electrical,[1-4] mechanical,[5-7] and chemical properties[8-10] at the nanoscale, which have made them functional in a variety of applications such as transistors,[11-13] photovoltaics,[14-16] sensors,[17-19] etc. However, carbon nanomaterials alone may not meet device specifications. Hence other types of functional nanomaterials should be incorporated to fabricate nanocomposites for improved performance. Besides, with the inherent ultralow density frameworks,[20-21] manufacturing of carbon nanomaterials faces multiple scalability challenges.[22] Therefore, it is crucial to design efficient manufacturing approaches for fabricating carbon nanocomposites in a scalable fashion for wider applications.

1.2 Carbon Nanocomposites for Energy Storage

1.2.1 Need of Energy Storage

The energy consumption worldwide is projected to increase from about 350 quadrillion Btu in 1990 to exceed 800 quadrillion Btu in 2040 according to the U.S. Energy Information Administration. Among traditional energy sources, fossil fuels provide the largest amount of energy (see Figure 1.1), but they are being depleted quickly and can cause severe environmental problems upon burning, such as greenhouse gases, which contribute to climate changes, water pollution, and air pollution.

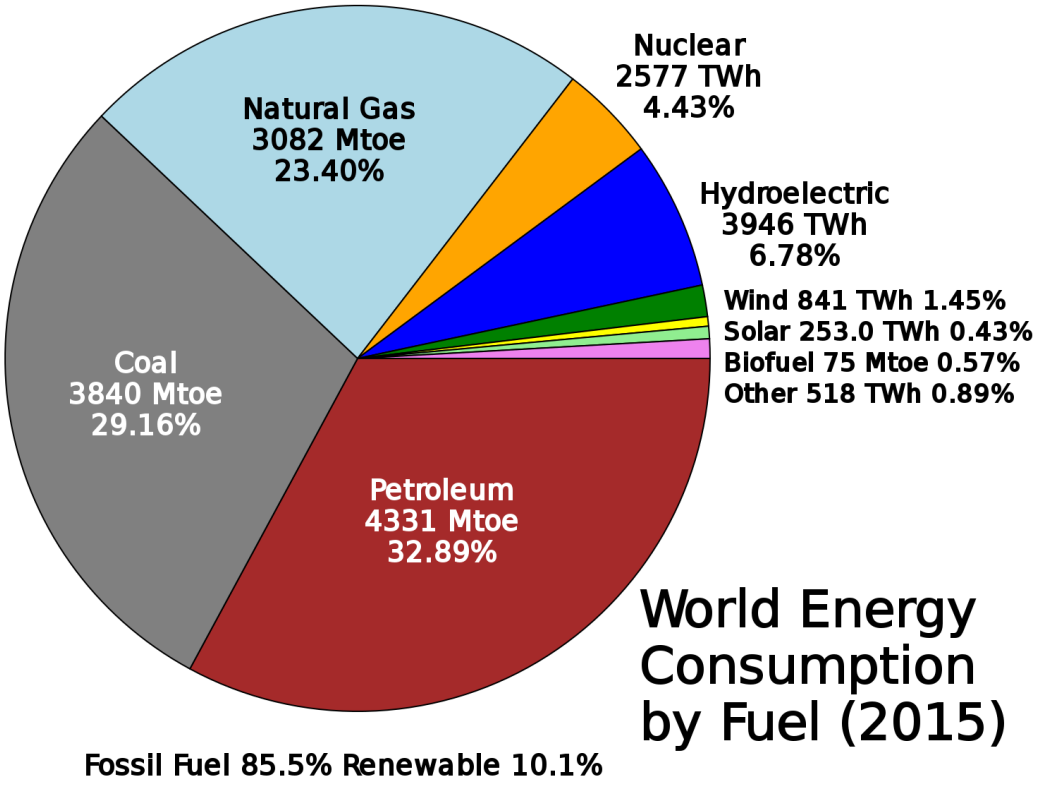

Figure 1.1 World energy consumption breakdown by energy sources in 2015.[23]

1.2.2 Current Status and Challenges

Research interests in carbon nanomaterials have been developing since the discovery of graphene in 2004. After the lithium-ion secondary battery was invented by John Goodenough and later commercialized by Sony in early 1990s, researchers have been investigating the application of carbon nanomaterials for energy storage. Carbon nanomaterials such as graphene and carbon nanotubes have high electrical conductivity, high surface area, and tunable surface chemistry, and thus can be favorable in multiple kinds of energy storage systems such as capacitive[24-25] and electrochemical energy storage.[26-28] In a conventional lithium-ion battery (see Figure 1.2) that is composed of graphite anode and lithium cobalt oxide cathode, the theoretical capacity of graphite is

only ~372 mAh/g. Despite research efforts focused on modifying the surface chemistry, doping, or defects of graphitic carbon, the achieved capacity and corresponding energy density is still far behind DOE's target (500 Wh/kg). Moreover, traditional methods of producing carbon nanomaterials such as vapor deposition method are still costly. Recently, electrochemical growth of carbon nanotubes from ambient carbon dioxide has been developed.[29-32] The concept of turning greenhouse gases into valuable carbon nanotubes at low-cost and high efficiency will encourage an enormous revisitation of carbon nanomaterials for many applications. As an alternative to lowering the production cost, researchers may also synthesize nanocomposites combining carbon nanomaterials with other promising electrochemical storage materials such as sulfur,[33-34] tin,[35-37] and phosphorus[38-40] to suit high-energy applications.

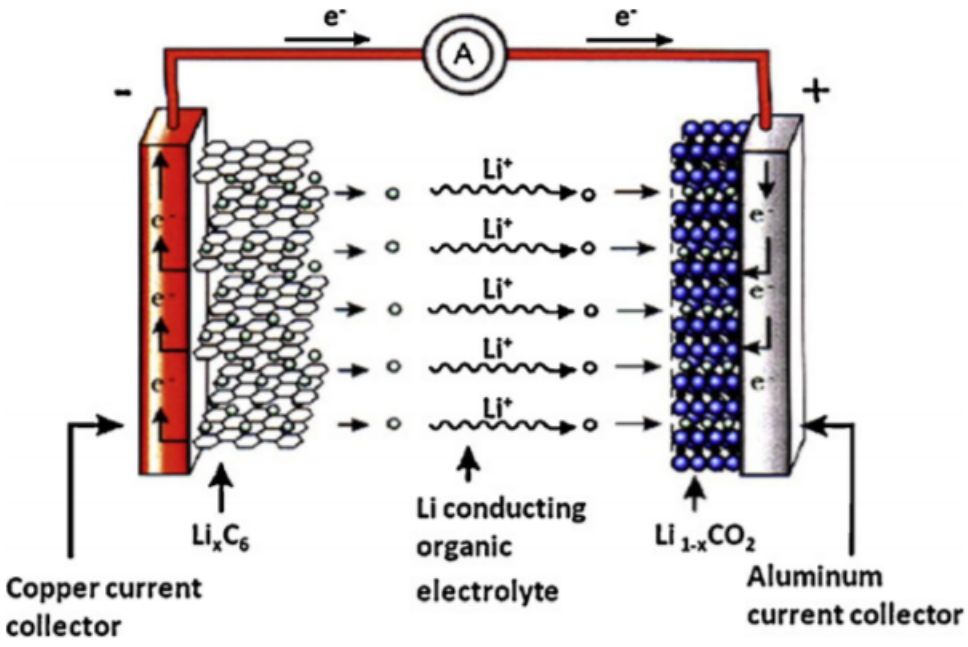

Figure 1.2 Scheme of a common lithium-ion battery.[41]

1.3 Carbon Nanocomposites for Environmental Applications

1.3.1 Heavy Metal Pollution

Heavy metals such as lead (Pb), chromium (Cr), and cadmium (Cd), are elements commonly found in nature. In many industries, waste effluents usually contain at least one or several heavy metal ions that can be harmful to the ecosystem and human body if not been managed properly. Among those, Cr has demanded serious attention due to the extreme toxicity of hexavalent chromium Cr (VI). Since Cr (VI) is soluble in water and has high mobility, lack of proper management will cause Cr (VI) to diffuse into soil and plants. Existence of Cr (VI) has been detected the tanning, paint, and welding industries, and studies have shown that exposure to Cr (VI) can cause respiratory tract irritation or lung cancer.

1.3.2 Current Status and Challenges

Carbon nanomaterials have been widely used for heavy metal removal in wastewater streams. Several strategies have been reported for wastewater treatment such as adsorption,[42-43] filtration,[44-45] and reduction.[46-47] The removal efficiency of heavy metal ions is strongly related to pH,[48] temperature,[49] concentration,[50] contact time,[51] etc. Adsorption and filtration are absolute physical processes, and the removal efficiency is directly related to the surface area of different carbon nanomaterial adsorbents. The reduction process usually involves chemical reactions and has been demonstrated with Cr (VI) removal capacity close to 100%, however, it is considered an energy intensive process compared to adsorption and filtration.Therefore, it is important to design approaches that can enable carbon nanomaterials to efficiently remove heavy metal from aqueous solution with high removal efficiency and low energy input. Moreover,

incorporating other nanomaterials to make nanocomposites can potentially improve the removal efficiency and charge efficiency of heavy metal removal.

1.4 Nanomanufacturing of Carbon Nanocomposites

Despite the fact that carbon nanomaterials have many potential applications for energy storage and environmental management due to their unique physical and chemical properties, there are still challenges in manufacturing, since the macroscale assembly of these nanostructures often compromises these desirable properties. Thus, scalable techniques to assemble appropriate carbon nanomaterials with other energy storage candidates into composites have become crucial. Meanwhile, most high-energy materials themselves have a series of problems for real application. Low electrical conductivity and large volume expansion due to conversion or alloying mechanisms are always expected. Such volume expansion can result in delamination or fracture of electrodes and loss of electrical contact, which can further result in severe pulverization and capacity fade.[52-54] By incorporating carbon nanomaterials in nanocomposites, the conductivity of electrodes can be greatly improved. With comprehensive understanding of the reaction mechanism and proper structural design, carbon materials can serve as structural confinement to prevent the undesirable volume expansion, thus prolonging cycle life and stabilizing capacity. In addition, to be able to achieve large-scale fabrication, less energy intensive techniques, simple fabrication process, and low-cost supplementary materials need to be developed.

Moreover, 3D free-standing CNT sponges with large porosity and hierarchical pores involve all the desired features that promise macro-scale manufacturing and engineering for composite electrode materials with ultrahigh loading. The hierarchical

porous structure promises mass-transfer, high surface area and chemically reactive sites. The freestanding nature of 3D CNT sponges can also ensure structural integrity during further processing and direct fabrication into electrode materials freeof binder materials and current collectors, which improves energy density and reduces the cost of battery manufacturing. The ultralight weight characteristics of 3D CNT sponges are also preferable for applications in portable devices, electric vehicles, and aircrafts. For next-generation energy storage devices, if the above two approaches can be combined effectively to make battery electrodes, the areal loading of active materials and energy density of the battery can both be improved and far surpass the properties of 1D raw powder-like CNTs and 2D pre-formed CNT films.

1.5 Organization of dissertation

This dissertation contains 6 main chapters.

Chapter 2 investigates the interactions at carbon-ionic liquid interface of a solid-state supercapacitor, which can lead to significant modification of the operation voltage of the device. This chapter highlights the importance of understanding chemical properties at supercapacitor interfaces to engineer voltage and energy capability.

Chapter 3 introduces a novel synthesis of interconnected foams of helical carbon nanofibers (CNFs) with ultra-high yield and desired structural, morphological, and physcial properties for stable sodium storage.

Chapter 4 illustrates the reaction mechanism between different carbon nanomaterials and different state sodium-phosphorus alloying products, that provide insights into building better red phosphorus-carbon composite anodes for high-capacity and high-energy sodium ion batteries (SIBs). This presents a mechanistic roadmap to guide the design of

red P-carbon composite anodes toward high theoretical sodium ion capacity (2596 mAh/g) while simultaneously addressing chemical interactions that compromise performance stability.

Chapter 5 demonstrates the broad capability to exploit interactions at different length scales in 2D materials to manufacture macroscopic functional materials containing hybrid black phosphorus/graphene (BP/G) heterostructured building blocks using electrophoretic deposition (EPD). This chapter provides insightful discussions on how controllable co-processing of 2D materials can enable material control for stacking and building block assembly relevant to broad future applications of 2D materials.

Chapter 6 demonstrates a strategy to produce high areal loading and areal capacity sulfur cathodes by using vapor phase infiltration of low-density carbon nanotube (CNT) foams, revealing high specific capacity, high sulfur areal loading, and high areal loading. This chapter highlights a new technique broadly adaptable to a diverse group of nanostructured building blocks where pre-formed low-density materials can be vapor infiltrated with sulfur and mechanically compressed to exhibit simultaneous high areal and gravimetric storage properties. This provides a route for scalable, low-cost, and high energy density sulfur cathodes based on conventional solid electrode processing routes.

Chapter 7 presents an electrochemical reduction process for hexavalent chromium (Cr (VI)) removal using compressed CNT foam electrodes. Besides achieving high removal efficiency of >90%, this work also discusses the importance of consideration of total energy input and charge efficiency of the system, and provides future insights in how to achieve high Cr (VI) removal efficiency while maintain low energy input and high charge efficiency, which is further meaningful for a sustainable environment.

Chapter 8 summarizes all the work and provides future outlooks.

CHAPTER 2

GRAPHENE COATED POROUS SILICON FOR SOLID-STATE SUPERCAPACITORS

2.1 Introduction

Electric double-layer capacitors (EDLCs) have commanded significant interest in recent years owing to the advanced capability to synthesize nanostructures with extraordinary surface area and electrochemical stability, such as graphene, carbon nanotubes, and other carbon-based nanomaterials.[24, 55-57] Whereas a battery or pseudocapacitor exhibits charge storage driven by reversible redox processes at the electrode-electrolyte interface, EDLCs, or more loosely termed supercapacitors, represent electrochemical energy storage through ions that assemble at the interface of a conductive material. The feature that distinguishes supercapacitor energy storage *versus* less-reversible Faradaic storage is the electrochemical voltage window that separates non-Faradaic capacitive ion storage at lower voltages from Faradaic processes occurring at high voltages. An EDLC is strictly required to operate within this voltage window, and its total maximum energy density can be approximated to scale with the square of the voltage window based on the formula adapted from energy stored in electrostatic capacitors.[58-59]

In this framework, research efforts aimed to improve the energy density or power capability of EDLC devices have connected materials with ultrahigh surface area, such as graphene, with wide voltage window electrolytes such as BF_4-containing ionic liquids.[60-63] These systems have been shown to operate over voltage ranges in excess of 4 V in some cases,[64] providing a significant boost in stored energy compared to materials employing organic-based electrolytes.[65-67] Energy density calculations based on active

electrode mass and assuming the validity of electrostatic capacitance equations yield energy densities above 80 Wh/kg for lightweight, high surface area materials such as graphene. However, studies carried out that employ identical electrolytes with apparently similar forms of carbon, such as single-walled carbon nanotubes (SWCNTs) and graphene, exhibit varying reported values for the maximum operating voltage of the devices[64-65, 68-70] – the feature upon which the energy density directly depends. For example, operating voltages that ranging from 2 to 4 V are reported for graphene and SWCNT electrodes coupled with 1-ethyl-3-methylimidizolium tetrafluoroborate ($EMIBF_4$) ionic liquid electrolytes.[71-73] Whereas the electrochemical window should vary as the electrode-electrolyte interface chemistry is modified, it is not as evident why this should occur for chemically-similar electrode-electrolyte interfaces. Until now, a full understanding of processes occurring at the electrode-electrolyte interface in EDLC devices remains elusive and challenged by the vast number of electrode materials and electrolytes that are usually the focus of research efforts in this area.

On this note, a significant research effort in battery systems has been devoted to studying the solid-electrolyte interphase (SEI) region that forms at the electrode-electrolyte interface and directs the charge storage via surface electrochemical redox processes.[74-75] This SEI layer is dependent on the chemical interaction of the electrolyte or solvent and the electrode material and can dominate the performance of electrodes produced with nanostructured materials. Whereas EDLCs operate in the absence of Faradaic reactions, the chemical nature of the interface between electrolytes and electrodes in supercapacitors remains an area that is difficult to study and poorly understood. However, in an analogous manner to batteries, this interface directly

mediates the onset of chemical processes that defines the total energy storage capability of the device.

In this work, we demonstrate that non-covalent pi-pi interactions[76] between EMIBF4 ionic liquid electrolytes and a carbon electrode surface can impact charge transfer processes that dictate the operating voltage window of the device. This builds from an observation that electrolytes produced by combining EMIBF4 ionic liquids with polyethylene oxide (PEO) lead to enhancements of the non-Faradaic electrochemical window. We characterize this effect using ex-situ Raman spectroscopy and electrochemical impedance spectroscopy, and based on these results we propose this being due to steric hindrance from the PEO of imidazole pi-pi stacking at the carbon-electrolyte interface. This observation underlines the importance of understanding chemical interfaces even in devices that store charge in the absence of chemical redox processes.

2.2 Methods

2.2.1 Porous silicon templated 3-D interconnected graphene fabrication

To generate controlled materials to be tested for electrochemical supercapacitors, porous silicon materials providing high surface area were used as catalytic templates for the growth of few-layered coatings of carbon, with few-layered properties similar to graphene.[77-81] This leads to as-grown carbon material interfaces that are assembled on a high surface area support that can be tested in the absence of chemical or liquid processing effects, which are known to leave residues on carbon materials.[82] Porous silicon was produced using highly boron-doped silicon wafers and electrochemical etching in an AMMT porous Si etching system. The etching process lasted for 180

seconds under a current density of 45 mA/cm^2 in a 3:8 (v:v) hydrofluoric acid (HF) (50% H_2O by volume)and ethanol solution. Scanning electron microscopy (SEM) confirmed that the resulting porous silicon film has a porosity of ~75% and a height of ~4 μm. The porous silicon was rinsed with ethanol and stored in an Ar glove box for further carbon or graphene growth. The growth process was performed by chemical vapor deposition (CVD) in a Lindberg Blue 1" tube furnace with the porous silicon piece placed at the center of the tube. The furnace was ramped up to 650 ℃ in the presence of constant gas flow of 1 SLM of Ar and 200 SCCM of H_2. 10 SCCM acetylene was added when the temperature reached 650 ℃ and the furnace was immediately ramped up to 750 ℃ and held for 10 minutes. Finally, the furnace was ramped up to 850 ℃ and held for another 10 minutes, the acetylene and H_2 were then turned off and the furnace was cooled down to room temperature under Ar flow. The resultant conformal coating of graphene like carbon was characterized through SEM and TEM (Figure 2.1a) and this was found similar to that reported in previous studies carbon growth on silicon.[77-80, 83] Samples were cut into ~1 cm x 1 cm pieces for supercapacitor testing.

2.2.2 Solid-state supercapacitor fabrication

Ionic liquid-containing polymer electrolyte was synthesized by first mixing 8 g propylene carbonate (PC) and 0.5 g polyethylene oxide (PEO, 900,000 M.W.) in glass containers and heated on a hot-plate at 55 ℃ until the mixture became uniform, viscous and translucent. $EMIBF_4$ was then added to the solution in quantities of 4.5, 1.16, 0.5, and 0.21 g to form PEO-$EMIBF_4$ solutions with 90, 70, 50 and 30 wt% $EMIBF_4$. As PC was evaporated during the following procedure, only PEO and $EMIBF_4$ remained in the

electrolyte. The resulting polymer electrolyte mixtures were sandwiched between two ~1 cm x 1 cm pieces of porous silicon to form a symmetric device.[81] Electrolyte infiltration and PC evaporation were achieved by placing the device in a vacuum oven at 50 ℃ overnight until the polymer had fully cured as evidenced by the polymer turning from translucent to opaque white. The 100 wt% $EMIBF_4$ device was fabricated by adding 1 drop of pure $EMIBF_4$ to wet a Celgard 1180 separator and place in between two pieces of porous electrodes. 0 wt% $EMIBF_4$ (pure PEO) control device was fabricated by directly pouring the PEO in PC solution onto porous electrode pieces, sandwiching, and vacuum infiltrating as discussed previously.

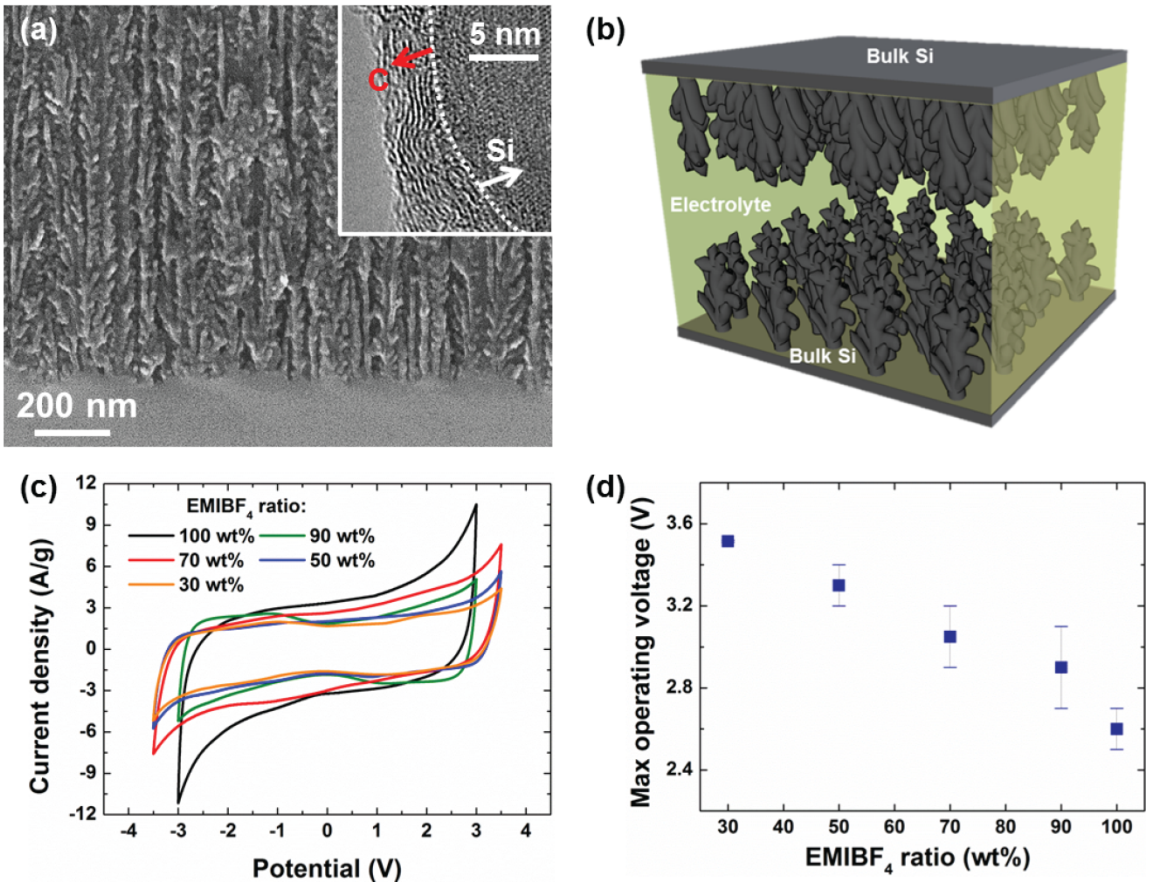

Figure 2.1. (a) SEM with inset TEM image of the porous silicon material with the carbon layer interfaced with the electrolyte; (b) Schematic illustration of the supercapacitor

device; (c) CV comparison and (d) corresponding electrochemical voltage window of devices with different ratios of $EMIBF_4$ and PEO in the electrolyte.

2.2.3 Electrochemical tests of solid-state supercapacitor

Galvanostatic charge/discharge, cyclic voltammetry (CV), and electrochemical impedance spectroscopy [80] were performed on a Metrohm Autolab Multichannel analyzer. Each device was placed in an MTI split flat cell. The devices were then pretreated using galvanostatic charge/discharge measurements at 1.5 A/g from 0 V to 2.5 V, after which CV scans were performed at a rate of 100 mV/s to different upper voltage limits ranging from 2.0 to 4.5 V. EIS measurements were performed under a frequency range of 1 MHz to 10 mHz around zero bias with a signal amplitude of 10 mV. The equivalent circuit model for each device was built by fitting the impedance data using the Autolab's NOVA testing and analysis software. After EIS measurements, rate tests were performed by galvanostatic charge/discharge measurements for three cycles each at several current densities ranging from 2.5 to 24 A/g. The voltage range is from 0 V to just under each device's estimated electrochemical window. To calculate the effective mass of electrode materials, the carbon mass was directly measured after coating using a semi-microbalance, and porosity, surface area, and height of porous silicon were used to determine silicon mass based on the known density of silicon. As the carbon layer is the active storage interface, calculations isolate both the graphene material mass as well as the combined carbon-silicon material mass for normalized performance assessment.

2.2.4 Cross-sectional Raman spectroscopy

To carry out *ex-situ* cross-sectional Raman spectroscopy, solid-state supercapacitors with

different $EMIBF_4$ ratios (> 0 wt%) were first tested *via* 5 galvanostatic charge/discharge cycles at 1.5 A/g with a voltage range from 0 V to 2.5 V. Then the device was cleaved and placed normal to an incident laser beam for Raman studies. Raman spectroscopy of solid-state supercapacitor cross sections were taken by using a Renishaw inVia MicroRaman system with 532 nm laser excitation. Area mapping of the porous silicon region was carried out in each device to enable statistical certainty in the reported measurements.

2.2.5 Other characterizations

Differential scanning calorimetry (DSC) tests were performed on pure $EMIBF_4$ and $EMIBF_4$ with carbonized porous silicon in a sealed Al pan. The sample pan and reference pan were set in the differential scanning calorimeter (TA Instruments). The samples were all heated up to 100 °C from room temperature and cooled down to -100 °C and go back to room temperature at a rate of 10 °C /min and repeated for two cycles. Ar gas was flown during measurement. Fourier-transform

2.3 Results & Discussion

Solid-state devices were fabricated by infiltrating graphene coated porous silicon electrodes with polymer electrolytes composed of PEO and $EMIBF_4$. A scheme showing the configuration of the supercapacitor device is in Figure 2.1b. The use of this electrode material is based on highly reliable device-to-device performance from the templated silicon that enables fundamental studies, and freedom from any chemical processing residues or effects that often challenge the robust repeatability of supercapacitors produced with freestanding graphene electrodes. To compare performance, the mass ratio

of PEO-$EMIBF_4$ in the electrolyte was varied, which was observed to have a significant effect on the measured device properties. Cyclic voltammetry (CV) measurements were performed using a scan rate of 100 mV/s. In the latter case, chemical processes are dictated by an activation energy that leads to an exponential rise in current at the onset of irreversible, Faradaic chemical processes. We estimated the electrochemical window by taking the voltage value above which drastic increase in current would be seen. CV results shown in Figure 2.1c indicate that the electrochemical window is strongly correlated to the PEO-$EMIBF_4$ ratio, with CV curves ranging from 100 wt% $EMIBF_4$ to 30 wt% $EMIBF_4$. Although $EMIBF_4$ is well-known for its electrochemical window near 4 V, the electrochemical window of our porous silicon templated graphene devices with pure $EMIBF_4$ electrolyte is near 2.7 V. However, as PEO is combined with $EMIBF_4$ and when the PEO concentration increases, the electrochemical window also increases (Figure 2.1d). In all cases, the trend of PEO-$EMIBF_4$ modification of the electrochemical window is evident outside of device-to-device variation that is based on measurements of at minimum 3-5 devices. For 30 wt% $EMIBF_4$ device, the electrochemical window of the supercapacitors reaches ~3.5 V. A pure $EMIBF_4$ device exhibited an electrochemical window of ~ 1.3 V and for 50 wt% EMIBF4 device, the electrochemical window is measured to be 1.4 V – which is within the measurement error, implying no change to the electrochemical window. This control comparison indicates that the observed increase in the electrochemical window with increasing polymer ratios is directly related to the interface between the carbon coating and the PEO-$EMIBF_4$ electrolyte.

To further assess the origin of this effect we performed electrochemical impedance spectroscopy [80] on several devices with PEO polymer electrolytes having 90,

70, 50, and 30 wt% $EMIBF_4$. All of the polymer based devices exhibited two semicircles in the high-frequency regime in the Nyquist plot shown in Figure 2.2a, which is represented by an equivalent circuit model shown in Figure 2.2b. The first semicircle is attributed to an electrolyte pinhole effect, which is commonly observed in polymer-based electrolytes due to tiny microvoids that form in the electrolyte,[84-85] and corresponds to R_1 in Figure 2.2b. Consistent with this notion, the device with 100 wt% $EMIBF_4$ on the other hand exhibited only one semicircle since the electrolyte is a pure ionic liquid. The second semicircle in the polymer based devices and the only semicircle in the 100 wt% $EMIBF_4$ device represents the charge transfer process that occurs between ions in the electrolyte and the double-layer and is denoted as the charge transfer resistance (R_{ct}), whose value generally corresponds to the diameter of this semicircle. Based on the depressed semicircles in each process, we used a constant phase element (CPE) in the equivalent circuit model instead of a double layer capacitor (C_{dl}) to achieve better fitting. The low-frequency sloped line in the Nyquist plot is represented by the Warburg impedance which is related to ion diffusion and transport through the electrolyte to the electrode/electrolyte interface. Finally, we also represent both leakage behavior caused by self-discharge (R_{leak}) and the bulk solution resistance (R_s) of the electrolyte in the equivalent circuit model in Figure 2.2b. The values obtained by fitting the data for varying levels of PEO relative to EMIBF4 ionic liquid in electrolytes are shown in Table 2.1.

$EMIBF_4$ ratio	**100 wt%**	**90 wt%**	**70 wt%**	**50 wt%**	**30 wt%**
R_s (Ω)	4.1	27.5	14.5	26	27
R_1 (Ω)	0	6	9.2	10.2	11.1
R_{ct} (Ω)	25.2	38.4	70.2	76.3	115
Warburg (mMho)	45	58	56	61	54

R_{leak} (Ω)	1.00E+06	1.00E+06	1.00E+06	1.00E+06	1.00E+06
χ^2	0.136	0.031	0.068	0.017	0.031

Table 2.1. Numeric values of different parts in the equivalent Randle circuit for devices with different $EMIBF_4$ ratios.

As we have shown that the carbon-electrolyte interface is the most important toward understanding the effect of the PEO on the observed variations in the electrochemical window, the value of R_{ct} gives insight into how the resistance changes with different concentrations of PEO in the electrolyte. Shown in Figure 2.2c is R_{ct} plotted as a function of $EMIBF_4$ concentration in a PEO-$EMIBF_4$ solid state electrolyte. Notably, the value of R_{ct} exhibits a significant dependence on the $EMIBF_4$ (PEO) concentration in the electrolyte and varies from ~26 Ω to ~115 Ω in a consistent manner when the electrolyte is varied from pure $EMIBF_4$ to 30 wt% $EMIBF_4$. Importantly, such a trend is not evident in R_s, which increases significantly upon the addition of polymer (4.3 Ω to 27.5 Ω), but does not vary consistently or widely across the different PEO-$EMIBF_4$ concentrations studied. This indicates that the presence of PEO plays a role to strongly influence the carbon-electrolyte interface and that this role can be distinguished from resistive contributions from the polymer solid state electrolyte itself.

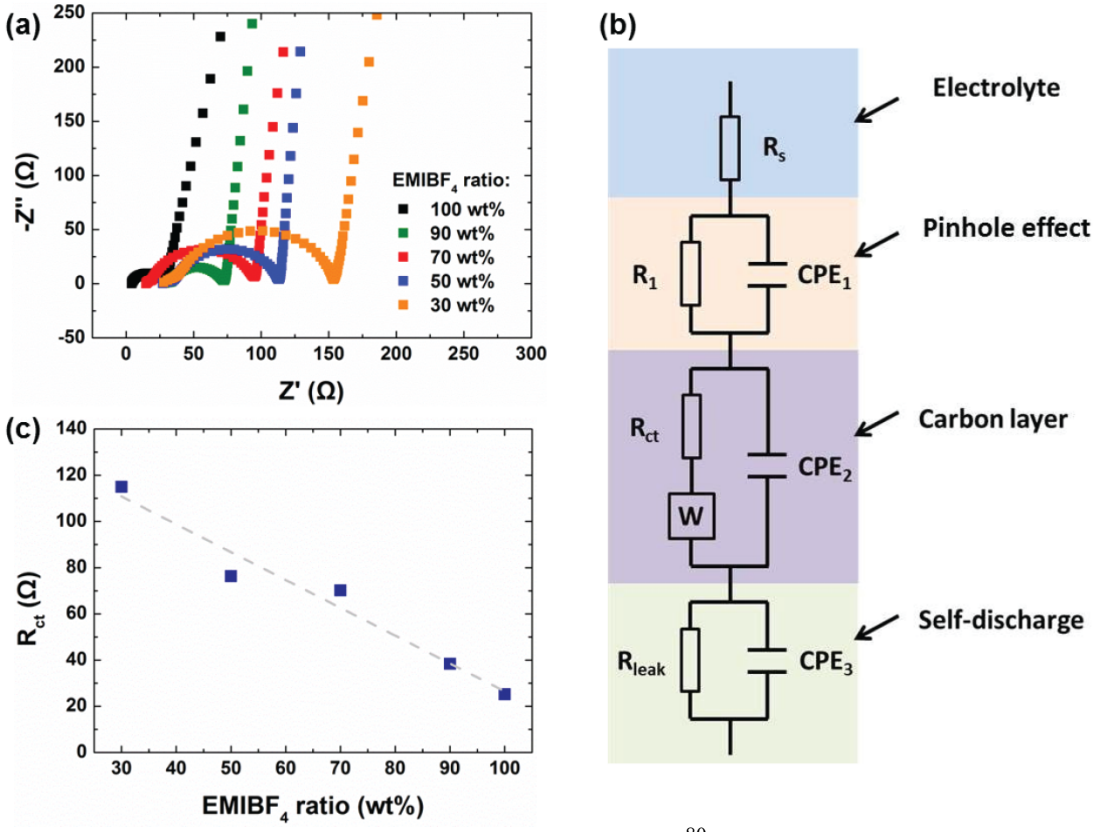

Figure 2.2. Electrochemical impedance spectroscopy [80] of supercapacitor devices with varying $EMIBF_4$ ratios; (a) Nyquist plot of the supercapacitor devices; (b) illustration of the equivalent circuit utilized to analyze the measured EIS characteristics, and (c) charge transfer resistance (R_{ct}) as a function of $EMIBF_4$ ratio with the gray dotted line indicating fitted trend of R_{ct} with different $EMIBF_4$ ratios (with adjusted R^2=0.95).

In order to address how the electrochemical window is correlated to this electrode-electrolyte interface, we utilized cross-sectional Raman spectroscopy on the coated porous silicon electrodes to specifically address the chemical and physical changes to the carbon layer that arise from different polymer-ionic liquid interfaces. Since the carbon-electrolyte interface is correlated to the varying electrochemical window, Raman spectroscopy can identify changes to the carbon material based on the

Raman spectroscopic signatures of carbon. For each device, large area maps of the cross section of the porous region of the electrodes were performed in order to develop a statistical representation of the Raman characteristics of the electrodes. As shown in Figure 2.3a, the resulting Raman spectra exhibits a D-band that corresponds to defects-activated or sp^3 hybridized carbon species (1344 cm^{-1}) and an in-plane vibrational mode that corresponds to the stretch mode of planar C-C species (1604 cm^{-1}).[86] Notably, the D band of this material is broader than planar graphene, which can be partly attributed to the 3-D nanoscale curvature of the surface that requires defects to mediate the conformal curvature of the few-layered carbons. To address the effect of differing polymer-ionic liquid ratios on the carbon material interface, the ratio of the D and G peak intensities was calculated based on maps over the porous region. Interestingly, despite the fact that each device was cycled inside the electrochemical window in the absence of Faradaic reactions, and each device contains the same starting carbon material, the I_D/I_G ratios showed a consistent linear decrease with increasing PEO concentration relative to $EMIBF_4$ (Figure 2.3b). Previous reports, including a recent report using molecules with imidazole groups,[87] have demonstrated that pi-pi stacking or non-covalent functionalization on the carbon surface is correlated with a weak increase of the D band due to the greater out-of-plane or sp^3 configuration of carbon atoms.[87-89] Since $EMIBF_4$ contains imidazole groups that give rise to pi-pi stacking between aromatics and the carbon surface, this explains the observed trend in the Raman spectra in Figure 2.3b. In the case of pure $EMIBF_4$, a greater effect of pi-stacking on the observed Raman spectra is observed as evidenced by a greater I_D/I_G ratio. When PEO is present, the PEO chains provide a steric hindrance at the electrode-electrolyte interface that inhibits pi-stacked

configurations (Figure 2.4). The observation that the I_D/I_G ratio scales linearly with PEO concentration reflects the linear proportionality between the number of PEO chains near the electrode surface and the effect of these chains on steric hindrance of the pi-stacked $EMIBF_4$. This explanation is further confirmed by control experiments that utilize the same electrode structure and electrolyte, but using a porous silicon-electrolyte interface instead of a carbon-electrolyte interface. In these experiments, no increase of the electrochemical voltage window was observed with increasing PEO concentration, supporting the important role of non-covalent interactions on the voltage window of the carbon-electrolyte electrochemical interface. Also, no change in the Raman spectra is observed while changing the PEO-$EMIBF_4$ ratio when there is only porous silicon-electrolyte interface. Recent simulations have also confirmed the potential for pi-stacking on charge transfer energetics from ionic liquids and solid surfaces, even though this has not been experimentally realized.[90] Notably, comparison of Raman data, charge transfer interface resistances, and the voltage window as a function of PEO concentration all result in a linear relationship, strongly supporting the correlation between pi-pi stacking at the carbon-electrolyte interface and the measured voltage window of the device.

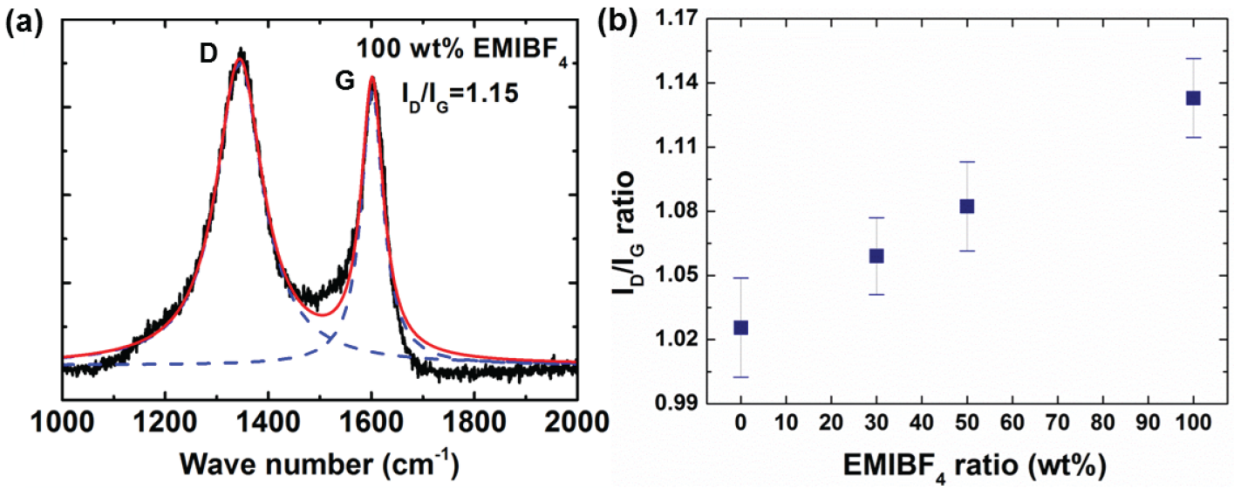

Figure 2.3. (a) Representative cross-sectional Raman spectra of the carbon-electrolyte interface showing the D and G modes of the carbon. (b) I_D to I_G intensity ratios for devices with different $EMIBF_4$ ratios.

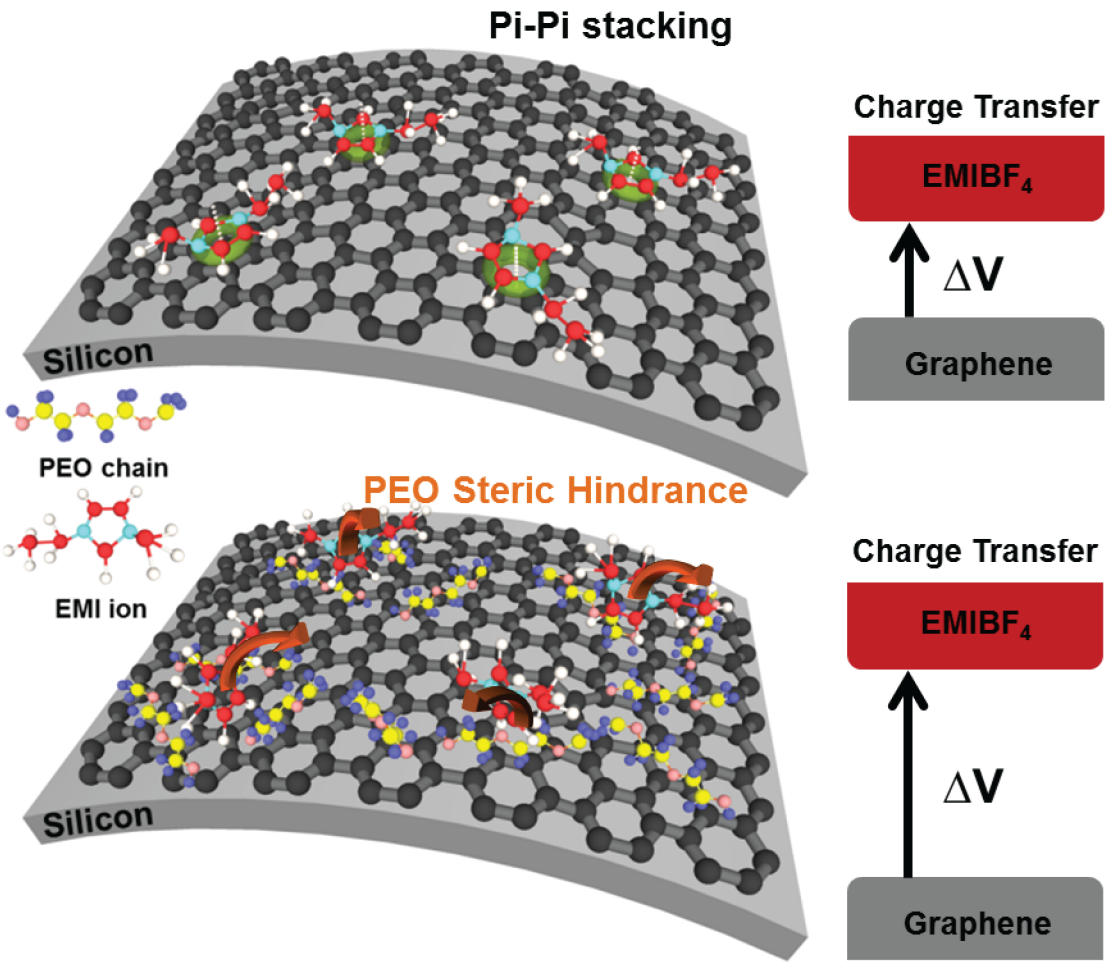

Figure 2.4. Schematic illustration of (top left) pi-stacking between EMI^+ ions and a silicon-supported carbon surface. (bottom left) Illustration of the role that PEO polymer plays in disrupting the pi-stacked configuration of electrolyte at the carbon-electrolyte interface through steric hindrance. In both cases, energy diagrams on the right represent the observation that pi-stacked configuration lead to lower operating voltage windows (ΔV) than cases where the PEO sterically inhibits pi-stacking.

This effect of pi-stacking is also evident based on the measured device performance of supercapacitors with varying concentrations of PEO. Shown in Figure 2.5a is the specific capacitance as a function of the total charging rate for galvanostatic charge-discharge measurements. In all cases, these numbers are normalized to both (1) the mass of carbon active storage interface, and (2) the combined carbon – porous silicon mass (total mass). Notably, the carbon materials remain supported by the porous silicon template to maintain a high level of consistency among device results. As a result, dissolving the porous silicon would activate additional surface area for double layer storage and would improve performance over that shown in Figure 2.5a. However, since the porous silicon templated devices exhibit an *identical* porous structure in all cases, evident trends can be associated to scale with the total concentration of PEO in the electrolyte. The decrease of capacitance with higher PEO concentrations can be understood through the conventional capacitor relationship of $C = \varepsilon\varepsilon_0 A/d$. In this case, the presence of PEO at the electrode-electrolyte interface can adversely impact both the dielectric constant of the double layer as well as the average distance of the Stern layer from the electrode surface due to pi-stacking effects. Therefore, this result is consistent

with the outcome of Raman and EIS analysis that implies that pi-stacking at the electrode-electrolyte interface plays a role in the double layer formation. Notably, due to the ideal structure of porous silicon materials that template the carbon layer, the specific capacitance is accessible at extraordinarily high rates greater than 20 A/g_{carbon}.

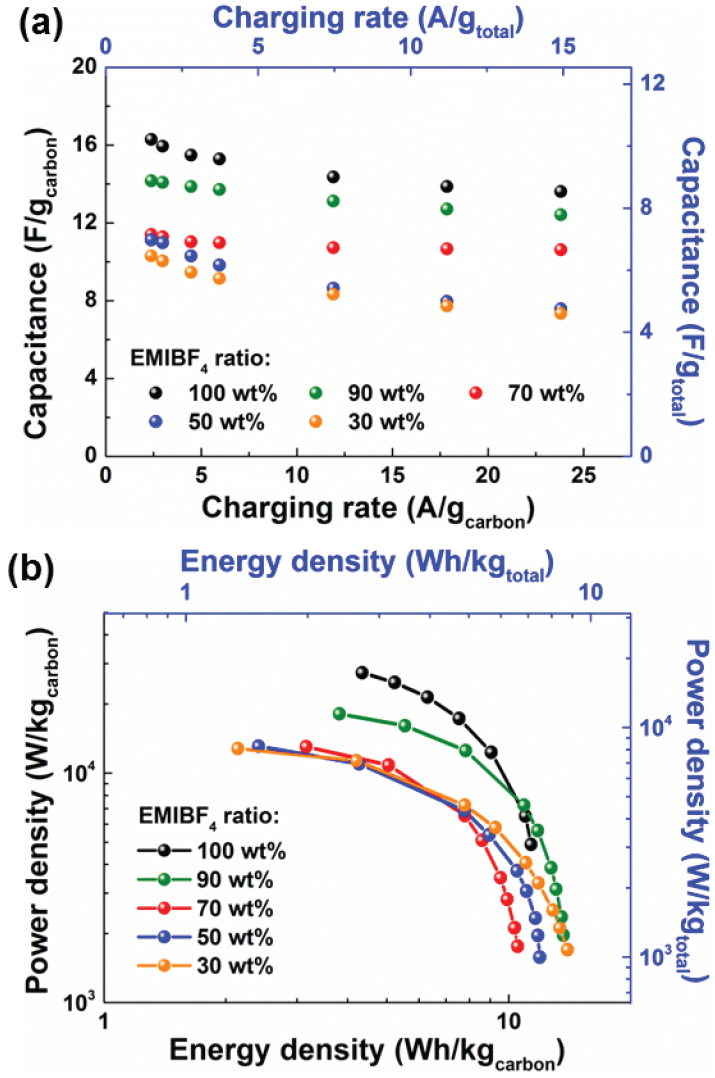

Figure 2.5. (a) Specific capacitance as a function of the charging rate for electrochemical supercapacitors having identical electrode structure, but with varying PEO-$EMIBF_4$ electrolyte ratios; (b) Ragone curve calculated based on eq (1) for identical device configurations as that in (a).

To better understand the impact of pi-stacking on the energy and power capability of these devices, we characterized the energy density and power density based on galvanostatic charge-discharge data taken at different rates (Figure 2.5b). To characterize the energy density, we integrated the discharge curve using

$$E = I_c \int_0^t V(t)dt \qquad (1)$$

where I_c is the charging current and *V(t)* is the discharge profile as a function of time. We then calculated the power density by using P=E/Δt where Δt is the total discharge time. In the case of ideal device performance, the energy density approximation of $E = \frac{1}{2}CV^2$ holds true. However, recent efforts have demonstrated that this relationship can significantly overestimate the energy density for any (real) non-ideal device by up to a factor of 2,[78, 81] leaving eq (1) to provide the *exact* energy density measured from the device. From Figure 2.5b, two regimes can be identified in terms of energy-power performance. The first regime involves a large energy density that is enabled by extending the voltage window to the highest values due to steric hindrance effects at the electrode-electrolyte interface. The second regime involves a large specific capacitance but lower voltage window due to the ideal pi-stacked interface between $EMIBF_4$ and carbon that minimizes the distance between the Stern layer and the carbon surface. However, the effect of steric hindrance to increase the voltage window and the role of pi-stacking to increase specific capacitance leads to a maximum energy density that is approximately the same for both extreme cases – near 10 Wh/kg based on the total silicon and carbon mass. Nonetheless, this highlights the notion that the energy and power performance of an electrochemical supercapacitor can be tuned by modifying the carbon-

electrolyte non-covalent interactions – a powerful tool in future efforts engineer and control the performance of electrochemical capacitor devices.

2.4 Conclusion

Our work reveals that non-covalent interactions at the carbon-electrolyte interface can strongly impact the operating voltage, and hence the total energy and power density of an electrochemical supercapacitor. Specifically, *ex-situ* Raman spectroscopy maps and impedance spectroscopy analysis elucidates the role of pi-pi stacking between imidazole species in the ionic liquid and the carbon surface – an effect that is shown to be only notable for carbon-ionic liquid interfaces. Pi-pi stacking effects lead to a stronger chemical interaction between the carbon and electrolyte, leading to a lower barrier for charge transfer reactions and a lower operating voltage of the device. Steric hindrance due to the incorporation of PEO chains near the electrode-electrolyte interface disrupt the pi-stacked configurations, and enhance the electrochemical window by over 25%. Such effects are also found to lower the specific capacitance due to the increased distance of the stern layer from the carbon surface. Our results indicate for the first time that pi-pi stacking at the electrolyte-carbon interface can influence performance of electrochemical capacitors, and this is enabled by the precision of porous silicon fabrication that enables templating of interconnected 3-D graphene structures with a natively high surface area. The understanding of interfacial processes on electrochemical capacitor performance enables practical tools that can be leveraged to design and optimize high performance in practical electrochemical capacitor templates. Such ideas can open a new paradigm for graphene or carbon based supercapacitors where high performance at industry scales is dictated by understanding of fundamental interfacial processes that control key

parameters as opposed to the iteration toward systems that exhibit high performance but lack the foundation of understanding to enable repeatability at large scales.

CHAPTER 3

HELICAL CARBON NANOFIBERS FOAM GROWN WITH ULTRAHIGH YIELD FOR HIGH CAPACITY SODIUM-ION BATTERIES

3.1 Introduction

As emerging technological areas such as electric vehicles and robotics are evolving to incorporate portable and rechargeable energy storage systems, the demands on cost, safety, and performance of battery technology are rapidly increasing. Sodium-ion batteries (SIBs) stand out as a promising platform to replace lithium-ion batteries due to the significantly increased earth abundance of sodium compared to lithium that can enable battery technology to penetrate grid-scale storage applications. However, numerous challenges in transitioning from lithium-ion to sodium-ion storage systems have been isolated.[91-92] Chiefly, as the radius of sodium ions is nearly 1.3X larger than that of lithium ions, simply using the same host electrode materials (crystalline carbons and metal oxides) leads to poor performance for SIBs. Studies have shown the maximum sodium capacity of graphitized carbon anodes to be < 35 mAh/g, which is over 10X lower than that possible with the same materials using lithium ions.[93]

Despite a number of studies centered on the sodium storage capability of carbons, the sodium storage mechanism in these materials remains controversial and a dynamic area of ongoing research. Early studies highlighted a house of cards type model consisting of two key storage modes for sodium in carbons: (1) storage of ions in between graphene layers which corresponds to the sloping voltage profile during sodiation; (2) ions filling the micro/nanopores ("pore-filling") in the carbons at lower potentials [94-97]. More recent experiments have highlighted the sodium storage behavior of a series of psuedographite materials derived from sustainable sources, such as banana

peels, emphasizing the critical optimization of porous nanodomains, defects, and intercalation for sodium storage [98-100]. These studies propose that the nanodomains in the carbon are critical to enable high capacity filling of the Na^+, which is correlated with the higher voltage component of the insertion curve. Lotfabd *et al.* carefully study the storage mechanism, observing no signature of reversible pore filling and a dilated interlayer spacing associated with sodium intercalation [100]. On the other hand, Bommier *et al.* carefully study defect-controlled hard carbons and conclude the (higher voltage) sloping voltage profile during sodium insertion is correlated to the defect content of the material, and similarly propose a surface reaction that leads to pore-filling of turbostratic nanodomains at lower voltages [101]. Alternatively, other routes have highlighted the mechanism for solvent cointercalation [102-103] of Na^+ species in carbon materials that enables extraordinary cycling and rate capability while still maintaining up to 150 mAh/g sodium storage capacities, as recently demonstrated for few-layered graphene [104]. Whereas researchers have reported a variety of carbon nanomaterials, usually based from defect-containing and/or hard carbons, to have attractive sodium storage properties [105-113], the engineering of carbon nanostructures to enable optimize sodium ion storage properties remains an area ripe for discovery and understanding. Further, a comprehensive understanding of sodium storage in carbons, which is likely to be dependent on the chemistry and physical characteristics of the carbons, remains elusive.

On another front, the growth, assembly, and energy applications of carbon nanomaterials in three-dimensional self-organized structures has been primarily centered on the science and applications of small diameter and high quality carbon nanotubes (CNTs) due to improved properties of these materials over their more defective

counterparts [114-115]. CNT-based interconnected solids or foams with elbows and defect-containing morphologies that stray from linear CNTs have been an emerging focus of recent research efforts [116-118]. The ability to engineer the defect content and structural properties of CNTs and carbon nanofibers (CNFs) in as-grown solids represents a research area that can extend the versatility of 3D foam structures of carbon nanomaterials to applications such as oil recovery, sensing, and other energy applications. Notably, based on recent advances in the understanding of sodium ion batteries [98, 101], such architectures should be ideally suited for this application.

Here we demonstrate the ability to pretreat nanoscale nickel materials using electrochemical oxidation to activate ultrahigh yield growth performance of high defect-content helical CNF materials. The CNF material can be directly incorporated as an anode into a sodium ion battery, exhibiting excellent sodium ion storage capacity and cycling capability attributed to a combination of defects and nanoporous regions in the carbons. Our efforts further use Raman spectroscopy to highlight the mechanistic benefit of the high-defect content tortuous bends in helical CNF materials to enable stable, high capacity anode cycling performance.

3.2 Methods

3.2.1 Preparation of CNF growth substrate

To grow helical CNF foams, commercially purchased Ni nanowires (Figure 3.1a) were soaked in 0.1 M NaOH (Sigma Aldrich) overnight (~18 h) and rinsed with deionized water (18 MΩ, obtained from a Millipore Milli-Q system). Electrochemical oxidation process [119-120] of pre-soaked Ni nanofoam was performed in deionized water initially under 30 V, using two same pieces of Ni nanofoams as both counter and working

electrode. 0.1 M NaOH was added dropwise and stirred mildly until the current reached to ~ 5 mA. Then DC potential was maintained for 30 min. After oxidation, the nanofoams were rinsed with deionized water until neutral pH was achieved. The working electrode was used for further characterization and as a high yield substrate for CNF growth. Figure 3.1b shows a SEM image of a representative electrochemically textured Ni material used as a precursor to grow helical CNFs. Notably, whereas our efforts build upon the use of Ni nanowires to optimize CNF yield, we observe this process to be universally applicable to any Ni material morphology to produce an oxidized and textured surface.

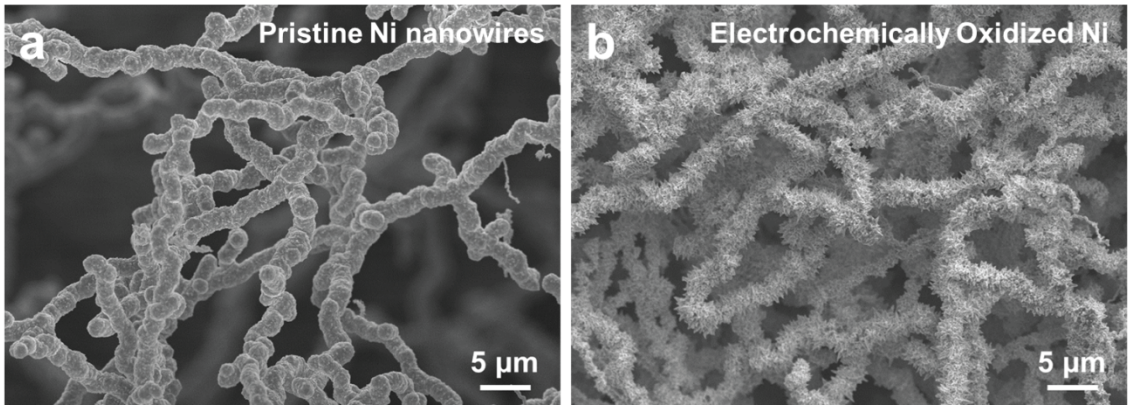

Figure 3.1. SEM images of (a) network of untreated Ni nanowires and (b) electrochemically oxidized network of Ni nanowires with a spiky surface that enables activation for high-yield helical CNF growth.

3.2.2 Helical CNF growth

A few mg (less than 1 mg) of the pretreated Ni nanowire material was placed into an alumina crucible, and placed into the central region of a chemical vapor deposition (CVD) system comprising a Lindberg Blue 1" tube furnace. To assess the ability for the oxidized Ni nanowires to maintain their textured surface morphology under reduction, we

first analyzed this point. The furnace was first ramped up to 500 ℃ under 400 sccm Ar. Then 200 sccm of H_2 were introduced and kept for 20 minutes for reduction of oxidized and textured surface of the pretreated Ni nanowires. Then H_2 was turned off and the furnace was cooled down to room temperature under Ar flow. To grow the helical CNFs, the growth process is performed by using the same set-up in Lindberg Blue 1" tube furnace. The furnace was ramped up to 500 ℃ again under 100 sccm Ar. Then 50 sccm H_2 and 2.5 sccm acetylene was introduced for 30 minutes for helical CNF growth. After growth process finished, H_2 and acetylene were turned off and the sample was cooled down to room temperature under Ar. As a control material, the same process was carried out on a Ni nanowire material with no electrochemical texturing, and hence a smooth surface morphology.

3.2.3 Material characterization and battery measurements

Scanning electron microscopy (SEM) imaging of the Ni nanowires, electrochemically oxidized Ni nanowires, and helical CNF materials was performed using a Zeiss Merlin Scanning Electron Microscope. Transmission electron microscopy (TEM) characterizations of CNFs were performed by using an FEI Osiris TEM. Raman spectroscopy of carbon nanofibers was conducted on a Renishaw inVia MicroRaman system with 785 nm laser excitation. *Ex-situ* Raman analysis was achieved by using a homemade air tight system with a glass slide on top as observation window.

To produce battery electrodes, the CNFs were mixed with conductive carbon black (TIMCAL SUPER C45) and poly(vinylidene difluoride) (PVDF, Alfa Aesar) as binder with mass ratio 80:10:10. Then the mixed electrode materials were dissolved in N-methyl pyrrolidinone (NMP) and sonicated for 1 h to form a slurry. The slurry was drop-casted

onto a stainless steel surface and dried in vacuum oven at 100 ℃ overnight. All electrochemical measurements were performed in CR 2032 type coin cells assembled in Ar-filled glove box. Sodium metal (Sigma Aldrich) was used as counter electrode. 1 M $NaPF_6$ (Strem, 99%) in ethylene carbonate (EC)/diethyl carbonate (DEC) (Sigma Aldrich, 99%/>99%) with volume ratio 4:6 was used as electrolyte. A Whatman grade GF/F glass fiber microfiber filter (Sigma Aldrich) was used as separator. Cyclic voltammetry (CV) measurements were performed on a Metrohm Autolab Multichannel analyzer from 0.01-3 V at a scan rate of 0.1 mV/s. Galvanostatic charge/discharge was performed on an MTI 8 channel battery analyzer between 0.01-3 V with a current density of 100 mA/g. Various current densities of 50, 100, 200, 500, and 1000 mA/g were applied for rate study.

3.3 Results & Discussion

The nucleation and growth of carbon nanotubes (CNTs) and carbon nanofibers (CNFs) is correlated to the formation of active nanostructured particles of catalytic metal on surfaces that support growth. Whereas numerous and broad efforts have been carried out to understand the types of catalyst materials and support layers to sustain catalytic growth of carbon nanostructures [114], the effect of surface morphology – especially with extreme nanoscale texturing, on such growth processes is not well understood. In this effort, we studied the growth of carbon nanostructures on electrochemically textured Ni nanostructures in order to explore the capability to directly grow an engineered carbon nanomaterial that can be incorporated as a sodium ion battery anode. Nanotextured Ni material used for helical CNF growth is shown in Figure 3.1a. During electrochemical oxidation in water, the electric field applied to the Ni nanowires leads to nucleation and

growth of pyramidal oxide nanocrystals on the surface of the Ni, leading to a uniform distribution of surface spikes (Figure 3.1b). Using such materials to grow carbon nanostructures is based on the premise that pretreatment of metal surfaces can be instrumental to enable or enhance catalytic activity from surface through mechanisms such as oxide surface reconstructions [121]. In this manner, we performed growth studies under conditions where the thermal reduction of the electrochemically pretreated "spiky" Ni nanowires maintains the spiky surface on a catalytic metal growth template that can hence impact the yield of catalytic growth.

To grow foams of helical CNFs, both the electrochemically textured and untreated Ni nanowire materials were used to compare the resulting growth performance. A key observation in our studies is that pretreated, oxidized Ni nanowires with spiky surface features lead to the growth of ultrahigh yield foams of carbon nanostructures. Whereas both the treated and untreated Ni materials lead to CNF growth, the size and mass of the CNF foam materials grown from the pretreated Ni templates are significantly greater than that observed from untreated Ni templates. As an example, with 0.48 mg spiky Ni nanostructures used in CVD growth, the resulting mass of bulk free-standing carbon foam composed of CNFs was 17.46 mg (3538 wt% increase). Similarly, with 0.83 mg untreated Ni materials in the same growth process, the mass of carbon foam was 13.49 mg (1525 wt% increase). The high yield of CNFs based on Ni template before and after CVD growth is visually shown in Figure 3.2b and Figure 3.2c. This trend was consistently observed in numerous experiments. Such increased yield with oxidative pretreatment has been observed with stainless steel and attributed to oxygen reconstruction on the surface to enhance growth yield [121]. In our case, whereas we

anticipate growth occurs from Ni metal surfaces, the electrochemically-induced reorganization of metal into a textured morphology increases the total amount of catalytic metal exposed to C_2H_2 precursor at the onset of nucleation, leading to overall greater catalytic activity from the same total mass of metal catalyst-containing materials. Specifically for battery applications, the ultrahigh yield of this process leads to a material that can be directly incorporated into a battery anode without need for further processing, as the carbon mass is significantly greater than that of the mass of the catalytic metals.

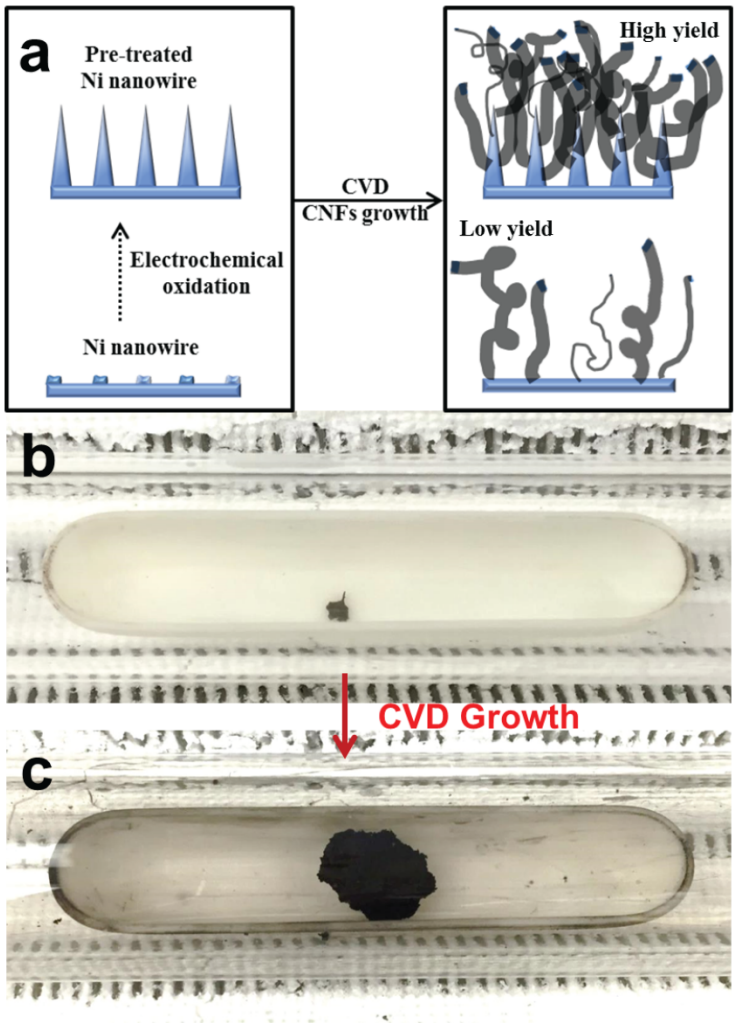

Figure 3.2. (a) Schematic illustration of the improved yield achieved from textured (pre-treated) Ni nanowire substrates. (b-c) Pictures of nanowires prior to growth (b) and after

growth (c) from pretreated textured Ni surfaces. This leads to an evident high yield of a compact foam of helical CNF materials.

To characterize nanocarbon materials in the foams during the growth process, SEM and Raman spectroscopic analysis was performed (Figure 3.3). Notably, both the electrochemically pretreated (spiky) and untreated Ni nanowires led to the catalytic growth of the same types of CNF materials based on SEM analysis and Raman spectroscopic characterization (Figure 3.3a-b) indicating growth conditions and not substrate pretreatment led to the resulting helical CNF materials. Overall, a wide distribution of CNF diameters were observed in SEM, with the majority of CNFs (> 80%) exhibiting arms or helical architectures representative of a high defect concentration in the carbon material. Raman spectroscopy analysis (Figure 3.3b) on foams grown from both pretreated Ni materials and untreated Ni materials indicates a similar intensity ratio and peak position of the D and G bands in both samples (*e.g.* $I_D/I_G \approx 1.6$), indicating a high defect content that is necessary for such arms and twists in the helical CNFs to form. A close-up view of a single representative helical CNF (Figure 3.3c) indicates the tortuous arrangement of carbon with nanopores at the high defect-containing elbow areas that are well-suited for sodium storage. High magnification TEM analysis of the graphitic ordering (Figure 3.3d) and the helical bends (Figure 3.3e) confirms a turbostratic arrangement of carbon in the form of CNFs with pores and ridges at elbows and bends in the materials. Overall, based on previous discussion on the mechanistic foundation of sodium storage processes in carbon materials, the high defect content of these materials combined with the accessible pores on the interior of the CNFs

makes these materials ideally suited for Na-ion batteries.

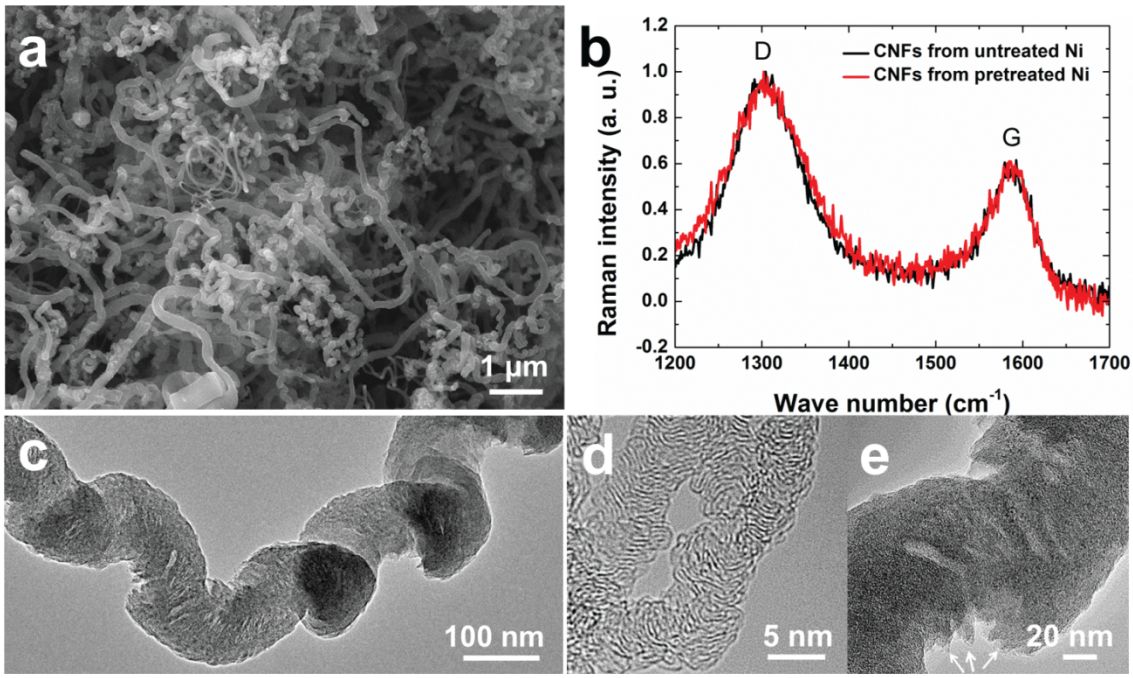

Figure 3.3. (a) Zoomed-out SEM image of as-grown CNFs showing fiber diameters and morphology. (b) Raman spectra from CNFs grown both from untreated Ni Nanowire materials and pretreated (oxidized) Ni nanowires. TEM images of (c) a single helical CNF, (d) CNF carbon material with small diameter features, and e) 'elbow' area of helical CNF.

To study the performance of these materials in batteries, coin cells were produced with foam materials in half-cell configurations with a Na metal counter electrode. Galvanostatic charge/discharge measurements were used to explore the sodium ion storage properties of CNFs. Figure 3.4a (solid lines) showed the 1st cycle charge/discharge comparison of CNFs grown from both pretreated (high-yield) and

untreated (low-yield) Ni nanostructures. For high-yield helical CNF foams, a high capacity of 1008 mAh/g upon initial discharge was measured with a reversible capacity of 283 mAh/g for the 2nd cycle (Figure 3.4a; dotted lines). The large irreversible capacity in the 1st cycle is attributed to the solid-electrolyte interphase (SEI) formation[108] due to the irreversible decomposition of electrolyte on the first cycle[105] and irreversible Na absorption at defect sites.[100] Following the first cycle, the charge-discharge performance exhibits a high Coulombic efficiency indicating a stable SEI layer formed in the first cycle. A similar observation was made for the CNFs grown from untreated Ni nanofoams (low-yield), except the total magnitude of capacity is lower due to the greater percentage of dense Ni metal in the nanofoam anode. In both cases, the majority of the sodium storage capacity can be attributed to the higher voltage sloping region in the charge-discharge curves. This region is correlated with the origin of irreversible capacity in sustainable pseudographite materials[100] and further associated with defects from controlled studies of hard carbons.[101] To further analyze the details of sodium storage electrochemistry, cyclic voltammetry measurements were carried out on helical CNF foam materials following the initial SEI formation. In these cases, similar results to that observed in galvanostatic data is apparent, with a sodium insertion/extraction redox couple that occurs generally below 0.5 V vs. Na/Na^+, with a sloping region below 1 V, and a strong contribution from the low-voltage insertion/extraction at lower voltages. Both materials show identical performance, except that the higher yield CNF foam leads to better specific storage capability due to a higher yield growth process. Notably, the origin of these electrochemical features remains a topic of controversy that has proven difficult to controllably establish likely due to the different chemical and physical

characteristics that carbon materials exhibit (*e.g.* defect density, crystallinity, nanodomain size and density, *etc.*). Recent work by Bommier *et al.*[101] proposes the high voltage sloping region to be correlated to the defect density of the carbons, and Lotfabd *et al.*[100] correlate this sloping region to irreversible capacity that is likely associated with defects. However, insertion at lower voltages has been correlated to underpotential (plating) deposition of metal into turbostratic nanodomains[101] or reversible intercalation into the carbons.[100] Across many studies, researchers observe a varying contribution to the reversible capacity associated with the higher voltage sloping characteristics and the lower voltage plateau. Recent studies have correlated the high voltage sloping characteristic to stable cycling performance with no capacity fade measured over 600 cycles.[32] From our data, we observe two apparent characteristics associated with insertion. Between ~ 1 V to 0.3 V vs. Na/Na^+, we observe a sloping profile that we associate with defect mediated storage that occurs at higher voltages due to the favorable energetics of sodium storage at defect sites. At lower voltages (< 0.3 V), we observe a distinct insertion characteristic attributed to underpotential deposition associated with filling of nanopores observed in helical CNFs through TEM analysis (Figure 3.3).

Cycling performances of CNFs are shown in Figure 3.4c. For helical CNFs grown with high yield (pretreated Ni nanowires) and cycled as batteries at 100 mA/g, Coulombic efficiency was higher than 95% after the 5th cycle and capacity retention ~98 % was maintained until 200 cycles. A similar observation was made for helical CNFs grown on untreated Ni materials, except with a lower total capacity during cycling consistent with other data. This implies that after stable SEI layer formation in these materials, the helical foams exhibit excellent cycling performance. Further, rate

capability measurements were performed at rates between 50 mA/g and 1000 mA/g, with a moderate stable capacity above 120 mAh/g at the fastest rates, indicating good rate performance.

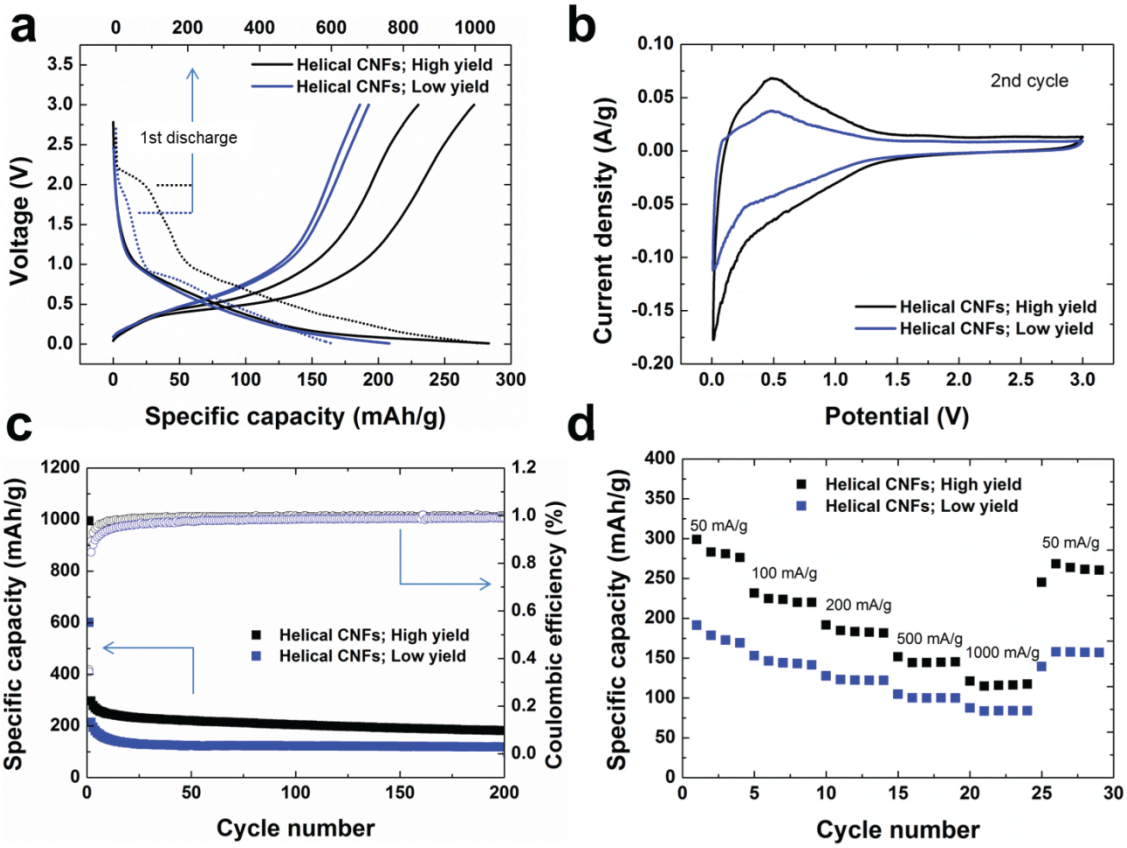

Figure 3.4. (a) Charge/discharge profiles of the 1st (dotted lines) and 2nd (solid lines) cycle at rate of 100 mA/g, (b) CV profiles showing the reversible storage performance of helical CNF anodes (100 mV/s), (c) cycling performance and Coulombic efficiency of helical CNFs at 100 mA/g, and (d) rate capability from charge-discharge tests at rates from 50 – 1000 mA/g.

To better understand the mechanistic sodium storage behavior of helical CNF foams, Raman characterization was performed on cells in the absence of air exposure

both before and after sodiation of the CNF materials. Prior to sodium insertion, the Raman modes of the helical CNFs match those shown in Figure 3.3b, with a similar D and G band intensity representative of a significant presence of sp^3 defective carbon in the CNFs. After sodiation, the D band exhibits a blue shift to a peak center of ~ 1315 cm^{-1} and G band red shifts to a peak center ~ 1590 cm^{-1}. There was no significant change in I_D to I_G ratio, indicating that sodiation does not lead to the notable formation of additional defect sites, but rather maintains the carbon coordination inherent to the pristine material. However, both the D and G bands exhibited peak broadening after sodiation. This similar behavior was observed in multiple subsequent tests. Similar qualitative peak shifting and broadening phenomena has been reported from *in-situ* Raman assessments of EMI^+ intercalation in activated carbon.[122] In this study, the D peak blue shift was explained as the disappearance of ring breathing modes at edges of crystalline domains, while the G peak red shift was explained through charge transfer. Notably, the peak shifts that are observed in our material are not generally consistent with that typically observed for both Li^+ and Na^+ intercalation in crystalline carbons,[104, 123-124] where ordered intercalation compounds evolve from dilute staging processes. Specifically, Raman modes of ordered stage 4 through stage 1 compounds in graphite materials are clearly distinguishable.[123] However, in contrast to this, our results for fully sodiated helical CNFs indicate only minor modification of the D and G band Raman signature that does not appear to reflect staging effects in a carbon intercalation compound (Figure 3.5). This would imply that the sodium storage in the helical CNFs does not appear to form an ordered intercalation compound of Na_xC_{1-x}. This is in general agreement with recent simulation studies that emphasizes positive formation energy for high capacity sodium intercalation compounds

in graphite indicating that, without some perturbation to the graphite lattice energetics, a high capacity staged sodium-graphite compound is thermodynamically prohibited.[125] However, Lotfabd *et al.*[100] describe an initial irreversible capacity associated with residual metal atoms maintaining positions at carbon defect sites that will provide local charge-transfer induced strain fields which may assist in overcoming energetic barriers of intercalation into pristine graphite. Whereas our results do not rule out staging associated with local sodium storage near or at defect sites, the high specific capacity (greater than that for NaC_8) and lack of an ordered staged compound is likely to indicate the role of the low-voltage pore filling in the storage mechanism of helical CNFs, as discussed by Bommier *et al*.[101] We therefore interpret this asymmetric Raman response and broadening to be a result of mechanical stresses and charge transfer at the carbon-sodium interface associated with the insertion and extraction of sodium from the material. Based on previous Raman studies [126-127] this response can be explained by local tensile stresses and charge transfer associated with sodium interfaces with carbon – either at defect sites or at filled pore sites. This leads to a system where capacities approaching ordered compounds such as LiC_6 can be achieved through a combination of defect sites that provide local storage and "on-ramps" to embedded pores, as well as micropore domains that facilitate local plating. Notably, this is also distinguished from co-intercalation[103] which does form ordered compounds containing Na^+, carbons, and solvent molecules with an appreciable storage capacity. Further studies building upon pioneering techniques, such as the scotch tape method [128], can lead to direct assessments of the interplay between defects, pores, intercalation and/or underpotential deposition processes that are likely strongly correlated to the physical and chemical properties of the carbon

materials that is evident from careful past studies. However, in this work we emphasize that helical CNF materials provide an excellent template for high capacity sodium storage, and combined with the versatility of controlled growth processes, can enable insight into the controversial and diverse intercalation mechanisms observed so far in a series of different carbon materials.

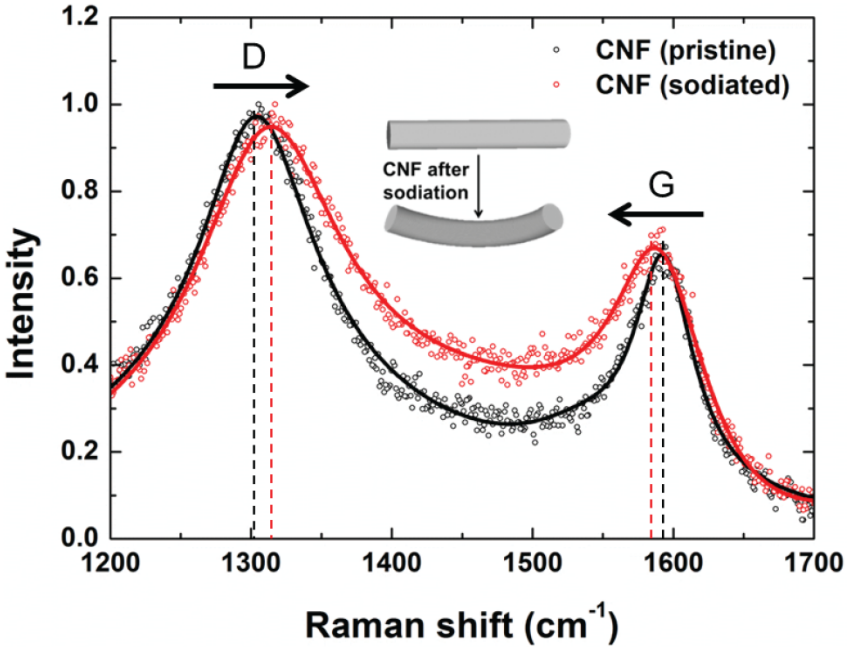

Figure 3.5. Raman analysis of helical CNFs before (black) and after (red) sodiation. The solid curves are Lorentzian fits. Data has been normalized to the D peak for clarity. Inset is a scheme highlighting one possible explanation for the observed shifts, noting this observation deviates from that expected from a highly ordered intercalation compound.

3.4 Conclusion

In summary, we have demonstrated an approach to electrochemically pretreat Ni nanowire precursors to form textured growth surfaces that yield solid foams of helical CNFs with ultrahigh yield. These helical CNFs provide a combination of defect sites and nanoporous regions in the bends and arms which activates their function for optimized

sodium storage. With ultrahigh yield growths, we demonstrate the ability to directly incorporate as-grown CNF foam materials as anodes in sodium ion batteries, with high reversible capacity exceeding 280 mAh/g and stable cycling performance for 200 cycles. We use Raman spectroscopy to assess the storage properties of this material, and highlight a mechanism of storage that is distinguished from conventional staging processes combining both pore filling and defect activated storage, in correlation with previous reports. This work provides a comprehensive connection between controlled, high-yield growth of carbon nanomaterials and direct incorporation of this material into sodium battery electrodes – an approach scalable to low-cost battery manufacturing processes.

CHAPTER 4

CARBON-RED PHOSPHORUS COMPOSITE ANODES FOR EFFICIENT SODIUM-ION BATTERIES

4.1 Introduction

Sodium ion batteries (SIBs) have attracted a great deal of focused research as an attractive alternative to Li-ion battery technology due to the low cost and earth abundance of sodium compared to lithium.[92, 129] However, unlike the diverse choices of anodes available in lithium batteries, a critical challenge for Na-ion battery chemistries resides in developing anode materials with high energy densities and appropriately low redox potentials *versus* Na/Na^+.[130-131] Among all anode materials reported for SIBs, phosphorus stands out as one of the most promising candidates due to the highest theoretical capacity (2596 mAh/g) delivered in a 3-electron involved alloying reaction to form Na_3P. Among the three common allotropes of phosphorus, red phosphorus (red P) is the most attractive for SIBs as a result of its relatively low cost and non-toxic nature. However, challenges exist in poor electrical conductivity and large volume expansion (~300 %) during sodiation. Recent efforts have focused on using carbon materials such as carbon black,[132] graphene,[133] carbon nanotubes (CNTs),[38] and mesoporous carbon to address the above issues.[134] Especially for carbon materials that can form three-dimensional conductive networks, have been demonstrated as good candidates to accelerate electron transfer process, alleviate volume change of alloying-type anodes, and prevent agglomeration of active materials for electrochemical energy storage devices.[135] However, despite the multitude of methods being used to make red P-carbon composites, mechanistic understanding of why carbon materials with similar graphitic nature exhibit varying electrochemical performances after mixing with red P still remains elusive. In spite of

some hypotheses, including enhanced binding between phosphorus and carbon atoms,[133, 136] successful confinement of red P,[137] and uniform distribution of red P into carbon matrix,[134] there is still a lack of fundamental understanding in the Na-red P alloying/dealloying process, and how carbon defects influence the reversibility of this reaction.

Outside of phosphorus anodes for SIBs, carbon scaffolds are also widely used for other battery electrodes to engineer the stability of insulating, high capacity active materials. One example is in the case of lithium-sulfur (Li-S) batteries where similarly low conductivity of sulfur, large volume expansion upon lithiation, and high-order polysulfide (Li_2S_n, $4 \leq n \leq 8$) dissolution present challenges that remain at the forefront of current research efforts.[138-139] Sulfur-carbon composites have been recently designed to overcome these challenges and achieve durable and high capacity battery performance.[139-145] To achieve stability, the carbon scaffold must be designed to enable high mass loading, enable physical confinement of polysulfides during the transition from soluble higher order polysulfides to insoluble low-order polysulfides, and enable strong polar sites to bind soluble polysulfides. Notably, carbon defect sites that include both dopants and sp^3 hybridized carbons have been demonstrated to play a beneficial role in binding soluble polysulfides and improving cycling performance.[146-151] Additionally, carbon nanomaterials such as nanospheres and nanofibers have been shown to enable sufficient surface area for deposition of low-order insoluble polysulfides and enable structural confinement within the scaffold.[152-156] Overall, research studies conducted in the past few years in Li-S batteries have documented the evident role that the scaffold can play in the battery chemistry, inspiring our efforts in this study to address the mechanistic

role of carbon interaction with red phosphorus to yield stable anodes with exceptionally high sodium storage capacity.

In this work we emphasize a mechanistic role for the carbon scaffold in phosphorus anodes that is opposite from that in Li-S batteries in that carbon defect sites lead to the growth of irreversible alloying products to accelerate capacity decay during cycling. By carefully controlling the defect density using sp^2 hybridized carbon SWCNTs and sp^3 hybridized SWCNHs combinations, our work demonstrates two distinct alloying regions – one denoted as the stable alloying region (0.40 and 0.15 V) that is not strongly influenced by the chemical properties of the carbon scaffolds, and the other denoted the unstable alloying region where defects facilitate the continuous formation of irreversible Na_3P products. This work provides mechanistic insight into concepts that must be taken account in the rational design of carbon-phosphorus scaffolds for sodium ion batteries and presents a platform to engage surface engineering routes[157] to improve and enable durable and high capacity sodium ion battery anodes.

4.2 Methods

4.2.1 Electrode preparation

The electrode was prepared by hand grinding commercial red phosphorus (red P) (99%, Sigma Aldrich) with single wall carbon nanohorns (SWCNHs) (Carbonium), single wall carbon nanotubes (SWCNTs) (HiPco purified, NanoIntegris), and SWCNT/SWCNH (50%/50%) with a mass ratio of 1:1 for 1h.

4.2.2 Electrochemical test

Pure red P, SWCNH-red P, SWCNT/SWCNH-red P, and SWCNT-red P were mixed

with sodium carboxymethyl cellulose (CMC) (Sigma-Aldrich, average Mw ~90,000) as binder and conductive carbon black (TIMCAL, SUPER C45) with a mass ratio of 7:2:1. Then the mixed electrode materials were dissolved in N-methyl-pyrrolidinone (NMP) and sonicated for 1h to form uniform slurry. The slurry was drop-casted onto a stainless steel surface and then dried in vacuum oven at 100 ℃ overnight. All electrochemical tests were performed in CR 2032 coin-type cells assembled in Ar-filled glovebox. 1 M $NaClO_4$ (Sigma-Aldrich, ≥98.0%) in ethylene carbonate (EC)/diethyl carbonate (DEC) (Sigma-Aldrich, 99%/>99%) with 1 to 1 volume ratio was used as electrolyte with additional 10 vol% 4-Fluoro-1,3-dioxolan-2-one (FEC) (Alfa Aesar, 98%) as electrolyte additive to help form stable solid-electrolyte interphase (SEI). A Whatman grade GF/F glass fiber microfiber filter (Sigma-Aldrich) was used as separator. Pure sodium was used as counter and reference electrode. Galvanostatic charge/discharge was performed between 0.001 and 2 V at a current density of 200 mA/g_{comp}. Rate studies were performed at current densities of 200, 400, 1000, and 2000 mA/g_{comp}.

4.2.3 Material Characterization

Scanning electron microscopy (SEM) images of SWCNH, SWCNT, SWCNH-red P, SWCNT/SWCNH-red P, and SWCNT-red P were acquired by a Zeiss Merlin Scanning Electron Microscope. Raman characterizations were performed by using a Renishaw inVia Raman spectrometer with a 532 nm laser. For characterizations of different alloying products, batteries were immediately opened inside the Ar filled glovebox during 2nd discharging process at different cut-off voltages of 0.30 V, 0.20 V, and 0.001 V, and electrodes were rinsed with DEC solvent carefully before transferring for ex-situ scanning transmission electron microscopy (STEM) study on a FEI Transmission

Electron Microscope.

4.3 Results & Discussion

To investigate the role of carbon defects and carbon nanostructure properties on the electrochemical reaction in red phosphorus composites, three distinct composite compositions were prepared using SWCNTs and SWCNHs. SWCNHs are all-carbon allotropes with a tubule structure and a conical cap at the end, and aggregate into spherical particles during synthesis with diameter between 60 to 120 nm, as shown in SEM image in Figure 4.1a. SWCNHs exhibit a significant presence of sp^3 hybridized carbon defects embedded into the sp^2 hybridized carbon matrix. In contrast, SWCNTs (HiPCO) are rolled graphene sheets with diameter typically below 1.0 nm that arrange in bundles as observed in SEM (Figure 4.1b). SWCNTs exhibit virtually no presence of sp^3 hybridized carbon and are therefore fully based on defect-free sp^2 hybridized carbon species. In a carbon-red P composite structure containing SWCNHs, increasing the ratio of SWCNHs relative to SWCNTs does not change the all-carbon nature of the material, but leads to a greater defect density and slightly decreases electrical interconnectivity due to the geometric characteristics of SWCNHs. To characterize the role that defects play in red P-carbon composites, we specifically compared films of SWCNTs, SWCNHs, and 1:1 composite SWCNT/SWCNH mixtures. Raman spectroscopy with 532 nm excitations (Figure 4.1c) elucidates the sp^2 hybridized carbons evident in the G-mode (~ 1590 cm^{-1})[158-159] and the out-of-plane sp^3 hybridized carbon atoms induced by defects in the D-mode (~ 1320 cm^{-1})[160-163] for carbon composite materials in this work. The intensity ratios of D peak to G peak (I_D/I_G) confirm the highest defect content in SWCNHs,

lowest/negligible defect content in SWCNTs, and an average in the 1:1 SWCNT/SWCNH composite. Following grinding to impregnate these different carbon materials with red P, the composite materials were characterized by SEM (Figs. 1d-1e). In these images, carbon materials form three-dimensional networks that prevent agglomeration of red P, and red P appears well-mixed with the carbons in each case, with slightly modified film geometry in the composites containing SWCNHs due to their spherical shape, instead of rope-like geometry of SWCNTs, which is pointed out in images using white circles.

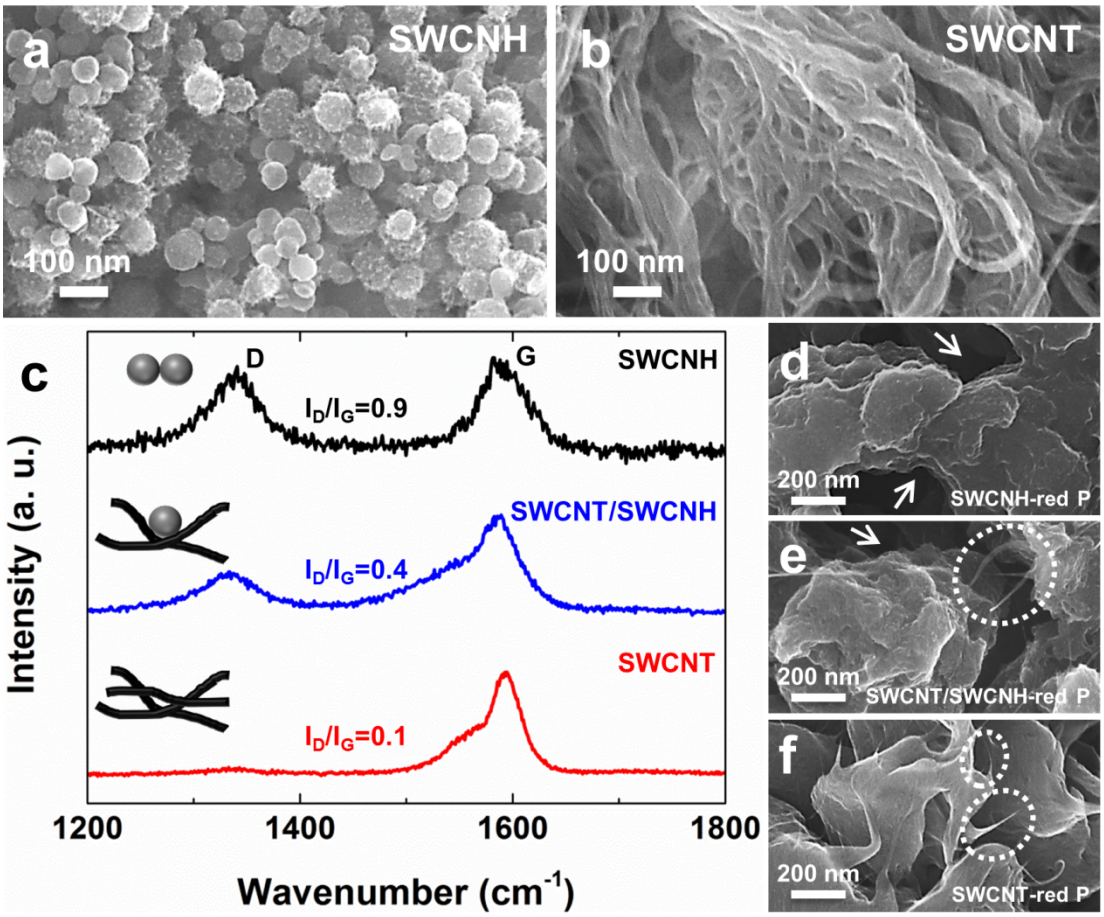

Figure 4.1 SEM images of pristine (a) SWCNHs and (b) SWCNTs. (c) Raman spectra of SWCNH, SWCNT/SWCNH, and SWCNT using 532 nm excitations. SEM zoom-in view

of (a) SWCNH-red P, (b) SWCNT/SWCNH-red P, and (c) SWCNT-red P with white arrows indicating geometrical modifications upon adding SWCNHs, and dotted circles indicating interconnected structure.

To assess the electrochemical performances of pure red P and carbon-red P composites, galvanostatic charge/discharge tests were performed. Pure red P has inherently low electrical conductivity. After mixing with polymer binder and conductive carbon, the red P anode alone showed an initial discharge capacity of 900 mAh/g_{comp} and then degraded to less than 50 mAh/g_{comp} in the following charge cycle. This is due to the large volume expansion (~300 %) during alloying with sodium, which further leads to severe electrode pulverization. The SWCNH-red P, SWCNT/SWCNH-red P, and SWCNT-red P composites with similar loadings exhibit capacities of 1167, 1477, 1521 mAh/g_{comp} from the 1st discharge, respectively, and 490, 640, 867 mAh/g_{comp} from the successive charge. The improved electrochemical performances demonstrate the successful role of carbon materials as conductive matrix and mechanical buffer for red P, even though distinctions exist in this comparison regarding the effectiveness of the different composite electrodes and their relative performance. This directed us to pursue a more comprehensive understanding of the mechanistic roles the carbon materials play in the chemical alloying reaction associated with sodium storage in red P.

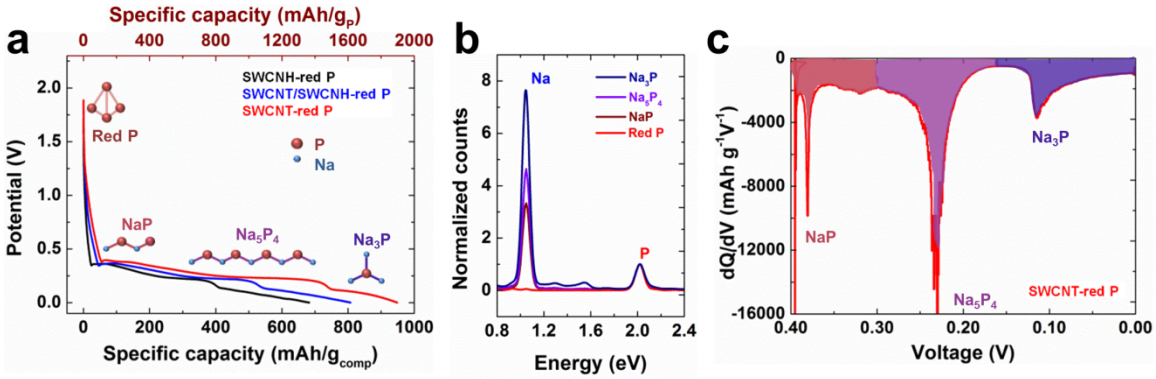

Figure 4.2 (a) 2nd-cycle galvanostatic discharge curve of different red P-carbon composites at a current density of 200 mA/g_{comp} with insets indicating different alloying products. (b) Ex-situ STEM elemental spectra of Na and P for different alloying products for SWCNT-red P anode. (c) differential charge (dQ/dV) curve derived from 2nd discharge.

To carefully examine the alloying states during charge/discharge, the three composites are compared based on their 2nd cycle discharge to eliminate effects from solid electrolyte interphase formation observed in the first discharge. As shown in Figure 4.2a, the carbon-red P composites undergo an alloying reaction with sodium ions and first form shallow, then medium, and finally deep alloying products during discharging from 2 V to 0.001 V. We note that although there is no available evidence to experimentally prove each distinctive phase, theoretical studies using density functional theory (DFT) calculations indicate three thermodynamically stable sodium-phosphate stoichiometric phases below 0.6 V, denoted as NaP, Na_5P_4, and Na_3P.[164] Here the formation of different phases is indicated with representative features of the discharge curve, along with the ball and stick models in Figure 4.2a indicating different Na to P ratios characteristic of the alloying states. Ex-situ STEM EDS elemental spectra were performed on different

alloying products to further confirm the transition of Na to P ratio upon discharging as seen in Figure 4.2b. To further characterize the electrochemical properties of each phase, differential capacity (dQ/dV) curves derived from discharge curves after the 1st cycle were analyzed. For illustration of the alloying process, the dQ/dV plot of only the SWCNT-red P composite at 2nd discharge cycle was shown in Figure 4.2b. Indicated with different shading, three distinctive peaks were observed which corresponded directly to the three alloying states and their products: NaP (red, shallow), Na_5P_4 (purple, medium), and Na_3P (blue, deep), respectively. The position of each peak implies the voltage at which each alloying state is formed. The area of each peak suggests the specific capacities delivered by the formation of each phase.

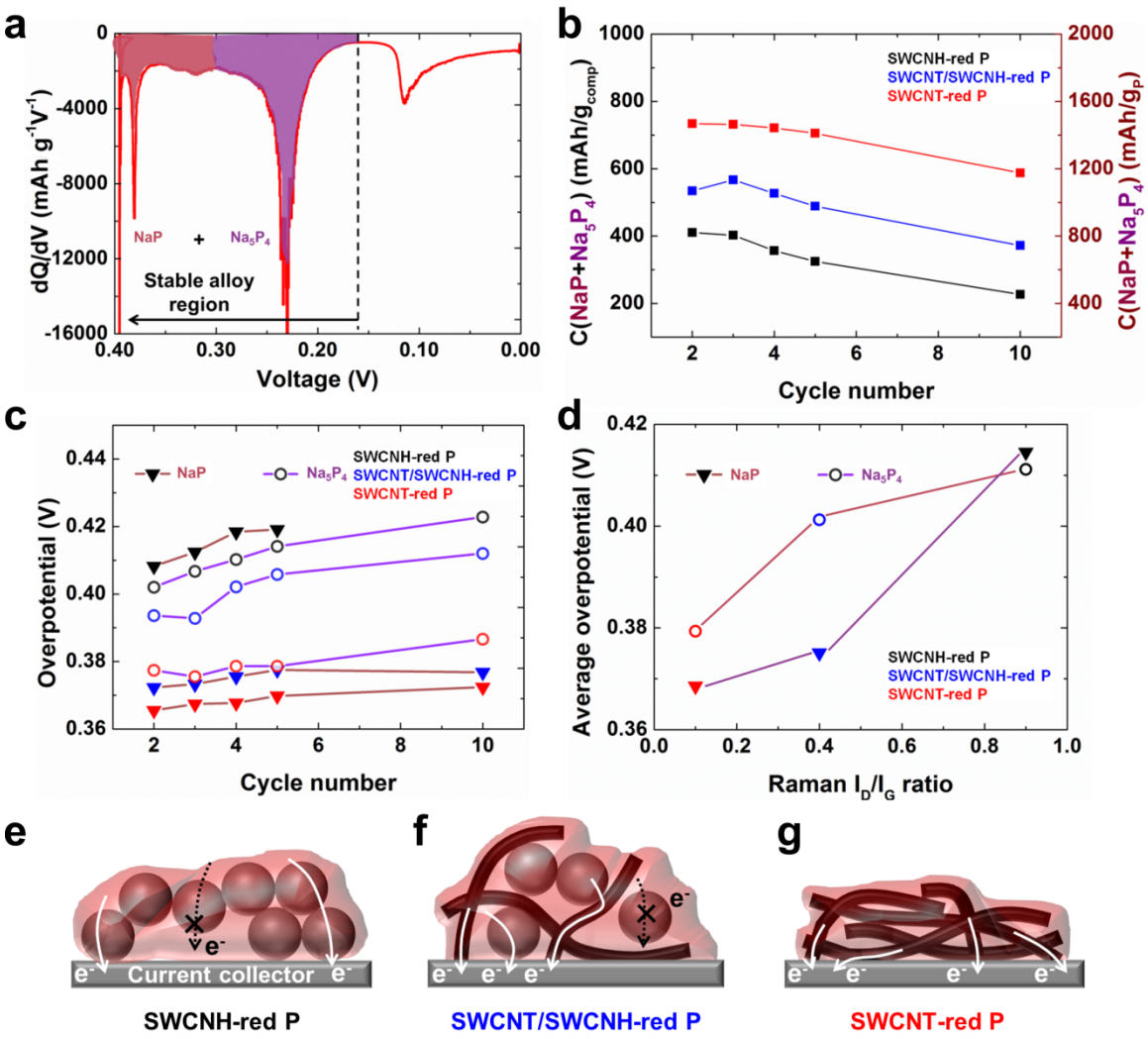

Figure 4.3 (a) differential charge (dQ/dV) curve derived from 2nd discharge with stable alloying products (NaP+Na_5P_4) formation highlighted. (b) Specific capacities delivered by stable alloying products. (c) Changes in overpotential upon cycling for two stable alloying products. (d) Overpotential for two stable alloys vs. Raman I_D/I_G ratio. (e) to (g) Schematic illustration of resistance differences between different carbon-red P composites due to the carbon geometry.

To better understand the evolution of the alloying phases for the different composites, the specific capacity delivered by only these alloy regions and corresponding

overpotential for each phase is plotted for the first 10 cycles. Assessment of these results leads to a straightforward delineation of the stable alloy phases as mostly independent of the carbon materials (Figure 4.3) and the unstable Na_3P alloy phase whose performance is strongly correlated to the carbon surface properties (Figure 4.4). In this spirit, we identify the stable alloy region (Figure 4.3a) to include NaP and Na_5P_4 formation. Specific capacities delivered by these two phases are 410, 534, 734 mAh/g_{comp} in the 2nd cycle for SWCNH-red P, SWCNT/SWCNH-red P, and SWCNT-red P and degradations of 20%, 8%, and 4% were observed from the 2nd to 5th cycle (Figure 4.3b), respectively. By the 10th cycle, the capacities delivered by stable alloy region for all three composites maintain more than 50% compared to the 2nd cycle. Notably, for all three carbon composite materials, the degradation that occurs during cycling of the stable phase alloying capacity seems to follow the same trend, only offset by the differences in initial capacity, which is due to solid electrolyte interphase (SEI) formation on different electrode architectures. To better understand this, overpotential measurements on the two stable alloying phases of all three composites were calculated using the difference in peak positions between charge and discharge from dQ/dV curves and indicate minimal change for NaP and Na_5P_4 for the three different composites with less than 10 mV for NaP phase, and 20 mV for Na_5P_4 phase (Figure 4.3c). For SWCNH-red P composite, the overpotential of NaP phase can only be monitored up to 5 cycles, which is because the NaP peak in dQ/dV plot becomes nearly unobservable. The differences in defect densities for different composites contribute to minimal changes (within 50 mV) in average overpotential as shown in Figure 4.3d. An additional key difference between the carbon composites is highlighted in this case in the overpotential for the alloying reactions to be

higher for SWCNH-red P composites in comparison to SWCNT-red P composites, and we attribute this to the poor electrical conductivity of SWCNHs. Schematic representation of the SWCNH composite (Figure 4.3e) reveals the spherical geometry providing the contact only at point locations where spheres come in contact limiting the number of continuous pathways between SWCNH-red P composite and current collector reflected as resistance in the cell. Void spaces in between spherical aggregates that are filled by red P (confirmed through SEM Figure 4.1d) do not provide electron pathways. After SWs are introduced (Figure 4.3f) more electron pathways are available because of the high aspect ratio and length that provides more electrical interconnections and pathways for electrons to the current collector. During hand grinding of SWs with red P, red P does not fill the empty spaces but instead forms a conformal coating on the outside of tube bundles, and exhibits more preferable contact between the composite and current collector with more electron pathways available and in turn lower resistance compared to the other composites (see Figure 4.3g). Whereas this is not a chemical mechanism for steering the alloying reaction in the same manner as defect density, the native electrical connectivity of SWCNTs in the composite leads to improved electron transfer to the insulating red P, resulting in lower overpotentials for alloying reactions as demonstrated in Figure 4.3e-g. However, in this stable alloying regime involving the formation of NaP and Na_5P_4 phases, our results overall indicate good stability and consistency of all three composite electrodes without significant chemical influence from the carbon materials.

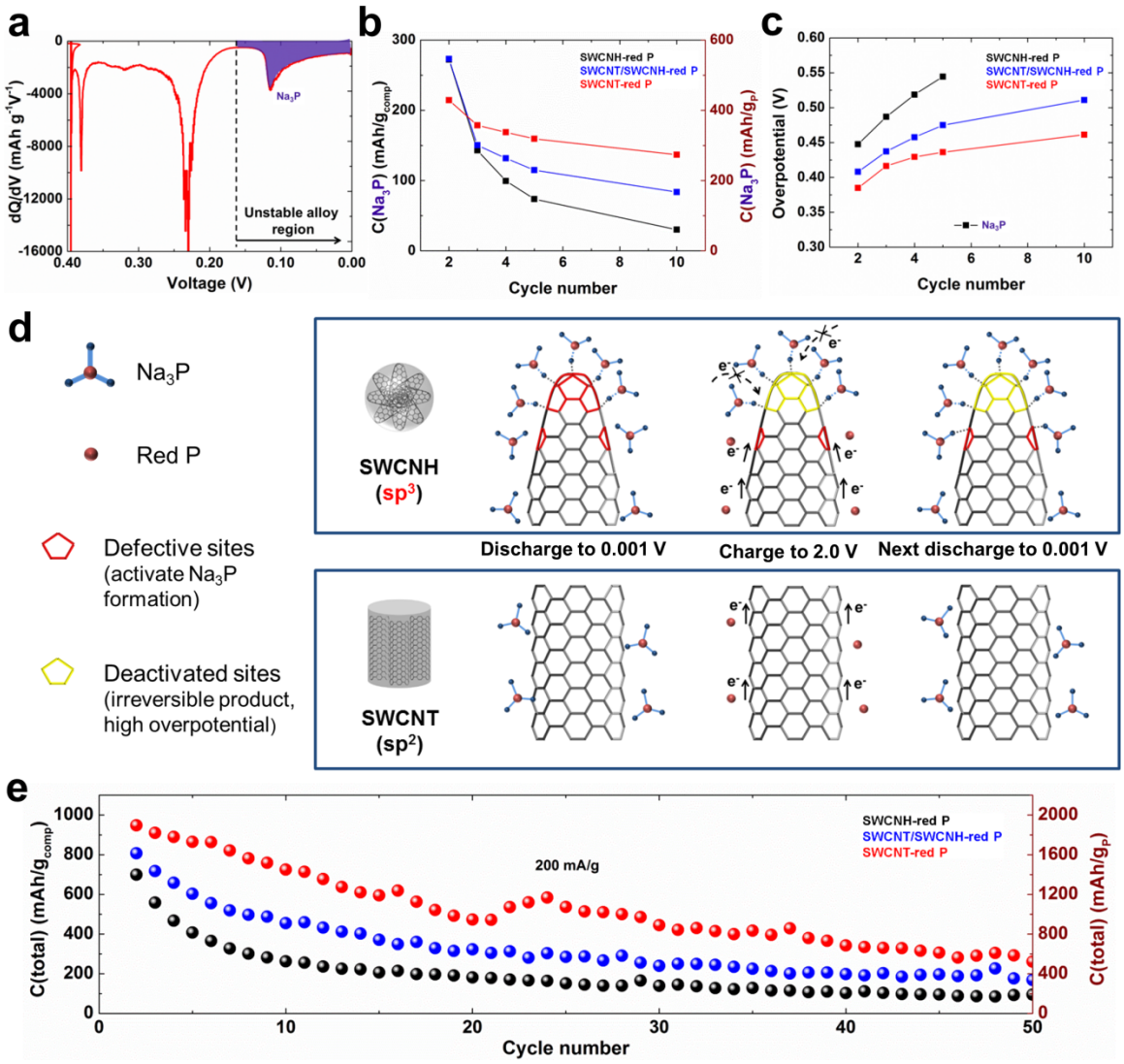

Figure 4.4 (a) dQ/dV curve derived from 2nd discharge with unstable alloying product (Na_3P) formation being highlighted. (b) Specific capacities delivered by unstable alloying product formation. (c) Changes in overpotential upon cycling for the unstable alloying product for different red P-carbon composites. (d) Schematic illustration underlying the carbon defect-dominated unstable alloy formation and increased resistance that leads to irreversible alloying/dealloying process. (e) Cycling performance of different carbon-red P composites at a current density of 200 mA/g_{comp}.

In contrast to this, in the unstable alloy region (Figure 4.4a) where the final alloying Na_3P phase is formed, the specific capacities delivered by Na_3P formation during discharge show values of 273 mAh/g_{comp} for SWCNH-red P, and 272 mAh/g_{comp} for SWCNT/SWCNH-red P in the 2nd cycle compared to 214 mAh/g_{comp} for the SWCNT composite. However the composites containing SWCNHs exhibit drastic degradation (Figure 4.4b) whereas the SWCNT-red P composite showed only minimal degradation. Furthermore, the differences between the composites containing SWCNHs (defects) and those without SWCNHs are evident by comparing overpotentials (Figure 4.4c). Similar trends of degradation based on different carbon-phosphorus composite anodes with different defect densities have also been observed in lithium ion batteries (LIBs) system.[165] Whereas the initial overpotential differences can be attributed to different electronic properties of each composite material (Figure 4.3c), the overpotential for Na_3P phase shows dramatic increases of 51 mV for SWCNT-red P, 67 mV for SWCNT/SWCNH-red P, and 97 mV for SWCNH-red P from 2nd to 5th cycle (Figure 4.4c) compared to less than 20 mV changes with cycling in the stable region. This qualifies the designation of the Na_3P phase as an unstable alloy region, and these results indicate the strong dependence of the stability of the alloying products in this region to the defect properties of the carbons. The mechanism behind this observation is presented and discussed in Figure 4.4d. Previous reports have shown that defects of graphitic materials are highly reactive sites for binding sodium ions due to the delocalized nature of electrons.[166-168] Recently, theoretical calculations showed that a single Na vacancy can lead to fast electron transfer in Na_3P phase, which has a semiconducting behavior.[164, 169] The abundant defect sites on the horns of SWCNHs initiate Na_3P formation during the

2nd discharge, leading to higher capacity contribution in the unstable alloy region. However, upon charging for SWCNH-containing composites, the Na_3P that effectively formed on discharge cannot be dealloyed and is then stored in the composite as an irreversible product. The existence of this product acts as a resistive barrier for electron transfer, which is observed as increased overpotential with subsequent cycles. Defective sites now coated with irreversible products are deactivated, meaning less Na_3P formation and rapid degradation of this alloy region. However, for SWCNT-red P, the non-defective nature of carbon does not provide specific activated sites for Na_3P formation, which corresponds to a more moderate 2nd discharge capacity in this region compared to the other two composites. This leads to cycling without production of irreversible products, and provides a surface that favors the reversible alloying/dealloying process.

In this manner, our results specifically elucidates that an ideal composite anode for red P will involve a surface site in the composite material that enables robust charge transfer between the conductive host material and Na_3P alloy phase. Our results indicate that this is accomplished with SWCNTs, which can be related to the capability of sp2 carbon defects to enable reversible charge transfer to Na_3P products without excessive Na_3P formation that limits the reversible charge transfer reaction. This provides the mechanistic foundation for the improved capacity measured for SWCNT-red P composites versus those containing SWCNHs (Figure 4.4e).. Overall, our studies not only shed light on fundamental considerations for Na-P alloying dealloying evolution, but also provide insights into future engineering of carbon/red P composites for SIB anodes. For example, surface engineering routes[157] employing ultrathin coatings to stabilize Na_3P surface products and provide fast charge transfer to enable the reversibility of these

products can enable anodes for Na-ion batteries that can leverage the extraordinarily high theoretical capacity of P in a durable cell configuration.

4.4 Conclusion

In summary, we utilize red P – carbon composites with controlled defect density to investigate the underlying mechanistic role that carbon defects play in the reversible alloying reaction of red P with Na. Our results elucidate stable alloying phases that include both NaP and Na_5P_4 that form in the range 0.4 – 0.15 V vs. Na/Na^+ which exhibit reversibility that does not appear correlated with the defect content of the carbon matrix. However, below 0.15 V we emphasize the formation of the final alloying product of Na_3P to occur in an unstable alloying regime, where the presence of defects in the carbon composite matrix lead to charge transfer barriers toward reversible alloying reactions with Na. Our work presents critical insight that effective composites for red P anodes that are able to maintain simultaneous durability and capacity approaching the theoretical limit of 2596 mAh/g will effectively leverage approaches to enable reversible charge transfer specifically tailored to the alloying reaction to form Na_3P. Our results suggest this as the mechanism for why sp^2 hybridized carbon is better suited as a reversible host material for red P anodes, but we envision future efforts that can leverage surface engineering routes to further improve performance in this unstable alloying regime.

CHAPTER 5

GRAPHENE-BLACK PHOSPHORUS HETEROSTRUCTURED BUILDING BLOCKS ASSEMBLED FOR SODIUM-ION BATTERIES

5.1 Introduction

Phosphorus has been reported as a promising candidate for sodium-ion battery (SIB) anodes due to the highest theoretical capacity of 2596 mAh/g among all the SIB anodes.[170-173] There are three common allotropes of phosphorus including white, red, and black phosphorus. White phosphorus is toxic and unstable in the ambient environment. Red phosphorus (red P) is cheap and abundant, but the amorphous structure, insulating property, and flammable nature make it less desirable for battery application. Unlike these two allotropes, black phosphorus (BP) is the most thermodynamically stable form, which is synthesized using cheap red P as raw material. Early syntheses of BP end up with high cost and low yield due to the required high pressure and high temperature environment and addition of expensive catalysts.[174-176] However, increasing research efforts have been developed recently on facile synthesis of BP that results into large-scale and environmental friendly production, and estimated low cost of less than 1 US dollar per gram, which makes BP promising for sustainable access and further applications.[177-180] Previous reports have shown electronic properties of BP highly attractive for next-generation electronic devices.[181-184] Recent studies have also demonstrated that 2D few-layer BP can enable both the highest capacity and fast ion-diffusion channels during the alloying process with sodium.[185-190]

To obtain 2D thin-layer BP, two common methods employed are mechanical exfoliation[191-193] and solution-based sonication/exfoliation[194-196]. For the specific application of battery materials, both methods produce a material that still requires binder

and conductive carbon additives in addition to the processed BP. Hence, multi-step processing must be performed to collect enough exfoliated materials from solution for electrode fabrication.[188, 197] Additionally, the volume expansion that is involved in the sodiation of black phosphorus has been reported to be above 300%, which can lead to electrode fracturing and capacity degradation upon cycling.[198-199] Thus, it is crucial to have mechanical buffering materials in the system that can accommodate the large volume expansion without undergoing local cracking or mechanical failure – emphasizing the need for complex electrode design strategies.

In this regard, architectures of 2D materials involving stacking have been reported recently for their capability to enable high rate performance, improve cycle life, and control the electrochemistry of battery electrodes.[200-201] The stacking of 2D materials is a novel nanomanufacturing strategy where the overall properties of stacked 2D heterostructures can compensate for the bottlenecks or limitations associated with either one of the 2D materials in the stack.[202-203] The stacking of 2D materials can also enable novel electronic,[113, 204] phononic,[205] or optical properties[206-207] that are differentiated from the individual 2D materials themselves. Graphene is often an excellent candidate as a co-stacking material due to its high electronic conductivity,[208] mechanical strength,[209] and fast reaction kinetics.[200] High-yield and low-cost production of graphene from graphite can be achieved by solution-based exfoliation process for further applications.[210-212] In the specific case of 2D BP, pioneering efforts that demonstrate stable anode cycling performance attributed this performance to van der Waals stacking between graphene and BP that occurs during vacuum filtration to fabricate electrodes.[188] Building from these efforts, methods to controllably engineer this beneficial BP/G architecture in bulk, such

as by exploiting interactions between different 2D nanomaterials during solvent processing, can enable highly tailored approaches to produce functional 2D structures in a scalable manner, which can then be coated onto desired surfaces and used for diverse applications.

In this spirit, here we demonstrate co-exfoliation of 2D graphene and BP materials to produce 2D heterostructured material in N-methyl-pyrrolidone (NMP) solvents. We demonstrate the resulting heterostructure formation to be due to the favorable electrostatic surface interaction between 2D BP and graphene materials dispersed in NMP solvents. These co-exfoliated heterostructured materials are then assembled onto conductive surfaces using electrophoretic deposition (EPD), which can be used as an effective way to produce thick coatings of 2D materials from dilute solutions. We then assess these heterostructured BP/G coatings as anodes in sodium ion batteries with no additional additives or binders, and observe a discharge capacity of 2365 mAh/g_P at a current density of 100 mA/g_P, which maintains a reversible capacity of 1297 mAh/g_P after 100 cycles. Our work gives insight into pathways for bulk processing of complex heterostructured 2D materials with application toward highly energy dense batteries.

5.2 Methods

5.2.1 Co-exfoliation of graphene and black phosphorous

12 mg of black phosphorous (crystal pieces from Smart Elements) and 12 mg of graphene (Graphene X from cheaptubes) were added into 40 mL N-methyl-pyrrolidinone (NMP). The solution was sonicated in ice bath by inserting the sonicator (Sonics, VCX750, 30% amplitude) probe into the centrifuge tube sealed with PDMS and Parafilm for minimizing

air exposure. The sonication process is set to be 3s pulse on and 3s pulse off to avoid excessive heating for 5 hrs. After sonication, the solution was left overnight for further use. For comparison, BP and G were individually probe sonicated in NMP solution with the same initial concentration of 0.6 mg/mL.

5.2.2 Electrode assembly by electrophoretic deposition

Electrophoretic deposition (EPD) was performed by using two identical stainless steel pieces (316 stainless steel coil from Trinity Brand Industries, 0.006 inch thick) with a size of 0.8 cm×3 cm as working and counter electrodes. Electrodes were immersed into 12 mL co-exfoliated solution in a plastic tube with an immersion depth of 2.5 cm. 200 V constant voltage was applied to the electrodes, and the corresponding current was recorded by a sourcemeter (Keithley 2400) integrated with a LabView data acquisition software.

5.2.3 Electrochemical test

Coin-cell type batteries were fabricated in an Ar-filled glovebox with O_2 level <0.5 ppm for electrochemical tests. Co-exfoliated BP/G on stainless steel by electrophoretic deposition was cut into ~0.8 cm×0.7 cm and applied as anode materials by directly cutting the stainless steel. Whatman grade GF/F glass microfiber was used as separator. 1 M $NaPF_6$ (Sigma Aldrich, 98%) in ethylene carbonate/diethyl carbonate (EC/DEC, 1/1 v/v, Sigma-Aldrich, 99%/>99%) with 10 vol% 4-Fluoro-1,3-dioxolan-2-one (FEC) (Alfa Aesar, 98%) was used as electrolyte. Sodium metal (Strem Chemicals, 99.95%) was used as counter electrode. Electrochemical charge/discharge was performed on a MTI battery testing system with current densities of 100 mA/g_P, 200 mA/g_P, 500 mA/g_P.

5.2.4 Material characterization

The morphology of electrodes with co-exfoliated BP/G deposited on stainless steel was characterized by using a Zeiss scanning electron microscope (SEM), The zeta potential and hydrostatic sizes of different exfoliated solution was measured on a Malvern Zetasizer Nano ZS instrument. The morphology of co-exfoliated BP/G in NMP solution and after EPD on steel were further characterized by a FEI Osiris transmission electron microscope (TEM). Crystallographic analysis of bulk BP, exfoliated BP, co-exfoliated BP/G, bulk G, exfoliated G was performed by using a Scintag XGEN 4000 to obtain X-ray diffraction pattern using Cu Kα 1.542 Å.

5.3 Results & Discussion

To investigate the solution assembly of 2D BP and graphene materials, BP and G were co-exfoliated in NMP solution by probe sonication. A schematic representing the observed co-exfoliation process *via* probe sonication is shown in Figure 1a. After 5-hr probe sonication in an ice bath, the initial clear solution with BP and G at the bottom became a uniform dark solution. To understand the solution properties of the resulting co-exfoliated solutions, zeta potential measurements were performed on exfoliated BP, BP/G and G in NMP solution respectively. Zeta potential measurements indicate the resulting surface charge on the exfoliated nanosheets in solution, with the BP in NMP showing the lowest average value of -31 mV, G in NMP of 1 mV, and BP/G in NMP of -8 mV (Figure 5.1b). This result emphasizes a key outcome of co-exfoliation in that the BP/G solution exhibits uniform and widely different surface charge properties than either the BP in NMP or G in NMP solutions individually. The measured zeta potential of BP/G in NMP solution indicates neutralized surface charge on the solvent shell-wrapped

nanosheets (Figs. 1c and 1d). This results from the interaction of heterostructures formed by the interaction between negatively charged exfoliated BP and positively charged exfoliated G surfaces,[213-214] leading to electrostatic-driven aggregation and heterostructure formation that act to neutralize surface charge in solution (Figs. 1 and 2).[215-217] This observation is further supported by measurement of the hydrostatic size distribution of co-exfoliated BP/G in NMP compared to exfoliated BP in NMP and exfoliated G in NMP. Following co-exfoliation, BP/G dispersed in NMP solution was characterized by transmission electron microscopy (TEM) (Figure 5.1e), with the inset plot showing the diffraction pattern indicating three lattice spacings of 2.1 Å, 2.6 Å, and 9.3 Å, which corresponds to graphene $(1\bar{1}00)$,[218-219] black phosphorus (111),[220] and increased graphene *d*-spacing due to the presence of some initial oxygen-containing functional groups on the surface.[221-222] Scanning TEM energy dispersive X-ray spectroscopy (STEM EDS) elemental mapping confirms the stacking of 2D thin sheets of BP and G, which confirmed the self-assembly between exfoliated BP and exfoliated G in solution (Figure 5.1f-1h). Notably, this technique for forming 2D heterostructured BP/G materials is distinguished from prior work[188] in that our approach leverages fundamental particle-particle electrostatic interactions in solution to drive heterostructure formation rather than drying effects at an interface that cause separate 2D materials to stack into thick sheets. By forming suspensions of heterostructures based on equilibrium electrostatic-driven processes in solution, we overcome scaling limitations of drying-induced heterostructure formation across interfaces that can be highly sensitive to factors such as drying rate, and enable a new versatile platform for large-scale processing of heterostructured 2D materials that can be broadly implemented into manufacturing-scale

processes.

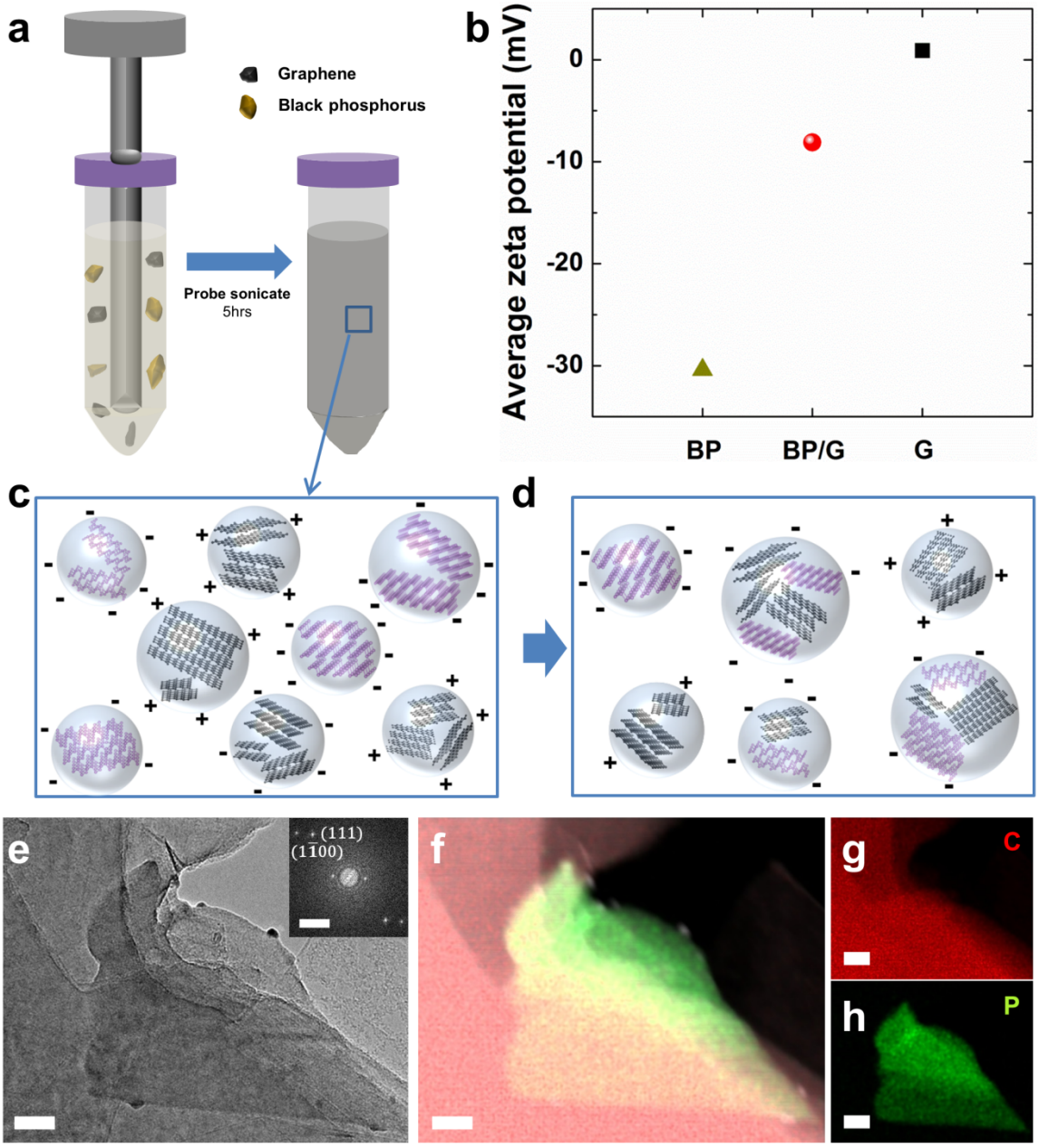

Figure 5.1 (a) Schematic illustration of the co-exfoliation of BP/G in NMP solution assisted by probe sonication. (b) Average zeta-potential measured on exfoliated BP in NMP, co-exfoliated BP/G in NMP, and exfoliated G in NMP. (c)-(d) Schemes of solution assembly process between exfoliated BP and G driven by electrostatic force. (e) High-resolution TEM image of BP/G in solution with the inset showing the diffraction pattern

of the characterized area, inset scale bar equals 2 nm^{-1}, and (f)-(h) TEM EDS elemental mapping of the characterized area (all scale bars equal 5 μm).

To assemble the BP/G heterostructured 2D materials into functional coatings, we utilized electrophoretic deposition (EPD). The set-up was shown schematically in Figure 5.2a, and involved two identical stainless steel electrodes immersed into the solution with a voltage of 200 V applied between the electrodes. Unlike other methods for assembly of 2D material films,[223-224] EPD is known to enable *complete* removal of solution-dispersed materials into uniform films that can be used in applications.[225] Figure 5.2b shows the I-t curve for the deposition, transformation from a dark to clear solution after 1400 seconds with a corresponding uniform film formation during the deposition of BP and BP/G was observed. However, for graphene, the low absolute value of Zeta potential resulted into no color change in solution before and after deposition, and minimal patchy graphene coating during EPD process. The initial higher slope of the I-t curve and shorter time needed to deposit an identical concentration, and hence mass, of 2D materials between the three curves can be explained by the difference in the electrophoretic mobility (μ) of exfoliated sheets. This is calculated using the Smoluchowski equation:

$$\mu = \frac{\varepsilon \varepsilon_0 \zeta}{\eta}$$

which can be applied to rigid particles with high aspect ratio.[226-227] Here, ε is the dielectric constant of the solution, ε_0 is the permittivity of free space, ζ is the zeta-potential of the dispersion, and η is the viscosity of the dispersion. Using the measured average zeta-potential value, the calculated electrophoretic mobility for exfoliated BP in NMP, BP/G in NMP and G in NMP is 5.2×10^{-9}, 1.4×10^{-9}, and 1.5×10^{-10} $m^2V^{-1}s^{-1}$, with

deposition mechanism illustrated in Figure 5.2c-e. For exfoliated BP in NMP, 2D BP nanosheets were rapidly assembled on the stainless steel electrode during EPD. For co-exfoliated BP/G in NMP, the pre-assembled nanosheets in solution maintained their structure through deposition where drying led to a thick layer of heterostructured BP/G material. Notably, control studies aimed to analyze sedimentation indicates no apparent sedimentation after 48 hours for the BP and BP/G solution, which is much longer than the timescale over which deposition takes place. Massive sedimentation was observed for the graphene solution after 12 hours. After EPD of co-exfoliated BP/G in NMP, the deposited materials on stainless steel electrode was characterized by scanning electron microscopy (SEM). The structure and morphology of the materials from top-down view were shown in Figure 5.2f, with multiple micron-sized sheets stacked together. SEM EDS elemental mapping results shown in Figure 5.2g-i indicate uniform distribution of exfoliated BP and G on stainless steel. TEM dark field image and corresponding EDS elemental mapping of the co-exfoliated materials after EPD are shown in Figure 5.2j and 2k-m, respectively. Exfoliated BP nanosheets were uniformly distributed in between exfoliated G, and formed sandwich-like heterostructures as a result of solution-driven assembly during co-exfoliation of BP and G and electric field-driven assembly during EPD.

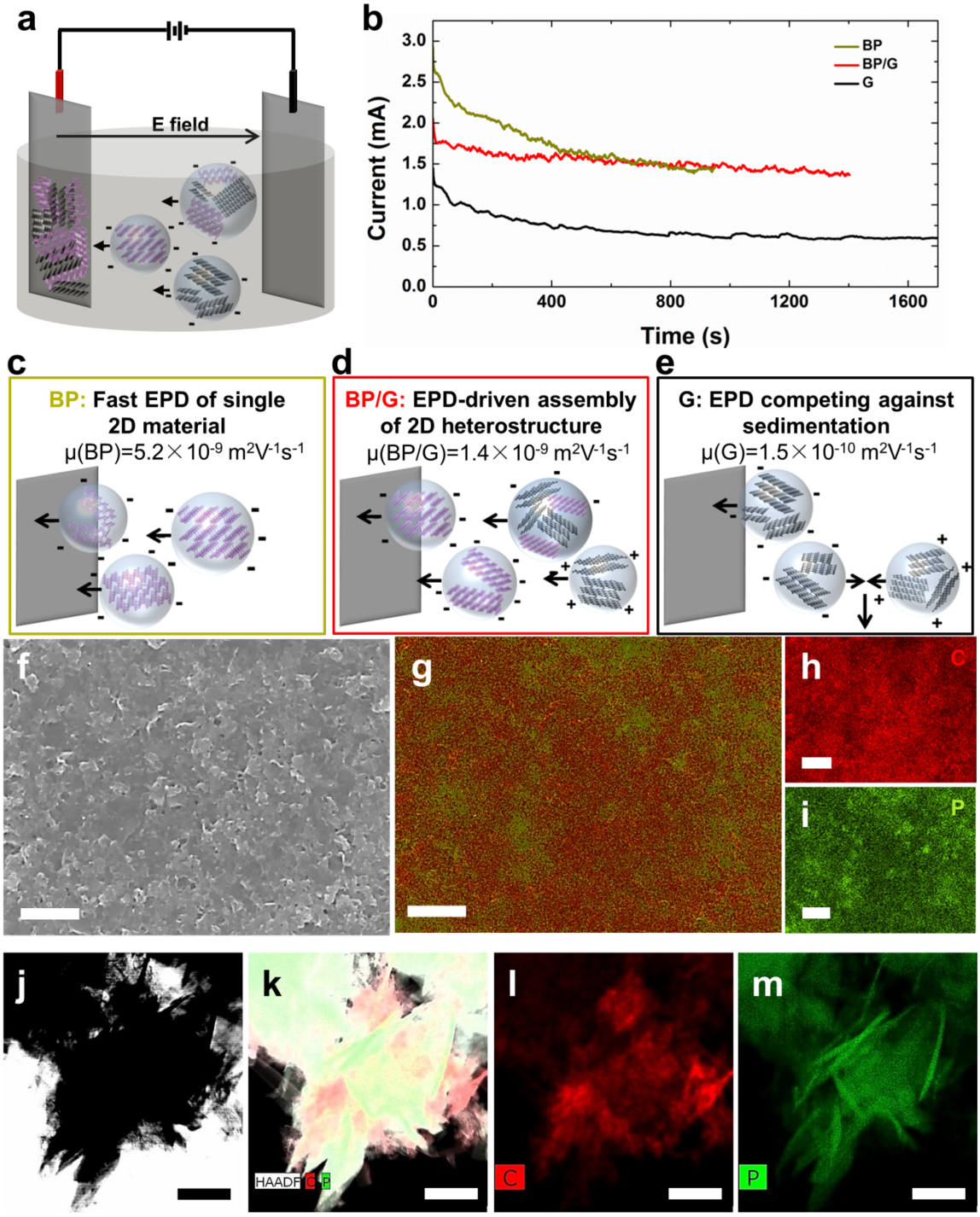

Figure 5.2 (a) Schematic illustration of the EPD process to assemble 2D heterostructures. (b) Deposition I-t curve for exfoliated BP, co-exfoliated BP/G, and exfoliated G in NMP solution. (c)-(e) Proposed deposition mechanism for the three different 2D materials studied. (f) SEM top-down view of the deposited materials on stainless steel electrode,

and (g)-(i) SEM EDS elemental mapping results of the area in (f), all scale bars represent 2 μm. (j) Dark-field TEM image of the material after deposition, and (k)-(m) TEM EDS elemental mapping of the BP/G heterostructure, all scale bars represent 500 nm.

To further characterize the properties of the exfoliated materials deposited by EPD, X-ray diffraction (XRD) was performed on bulk BP, bulk G, exfoliated BP, exfoliated G, and co-exfoliated BP/G (Figure 5.3a). Bulk BP exhibited three characteristic peaks around 17˚, 34˚, and 52.5˚ that correspond to (020), (040) and (060), which confirmed its orthorhombic structure.[220] Bulk graphite displayed a broad peak around 26.7˚ and 43˚, which corresponds to the interlayer spacing of (002) and (100), respectively.[228-229] After exfoliation, BP showed another characteristic peak around 26˚ that corresponds to the (021) lattice.[230-231] Exfoliated G maintained similar features in XRD patterns to that of graphite. For the co-exfoliated BP/G, several peaks around 17˚, 26.7˚, 34.6˚, and 35.4˚ demonstrated the existence of highly crystalline exfoliated G and exfoliated BP. The disappearance of peaks within the range of 40˚ to 45˚ and 50˚ to 55˚ could possibly due to the assembly and formation of 2D heterostructure. The Raman spectroscopy of co-exfoliated BP/G shown in Figure 5.3b indicated the distinctive A_g^1, B_{2g}, and A_g^2 peaks of BP centered at 363 cm^{-1}, 440 cm^{-1} and 467 cm^{-1}.[232-234] The D and G peaks centered at 1347 cm^{-1} and 1582 cm^{-1} are characteristic peaks for graphitic carbon. The presence of a D peak is attributed to edge effects of small flakes during solvent exfoliation process in NMP.[159, 235]

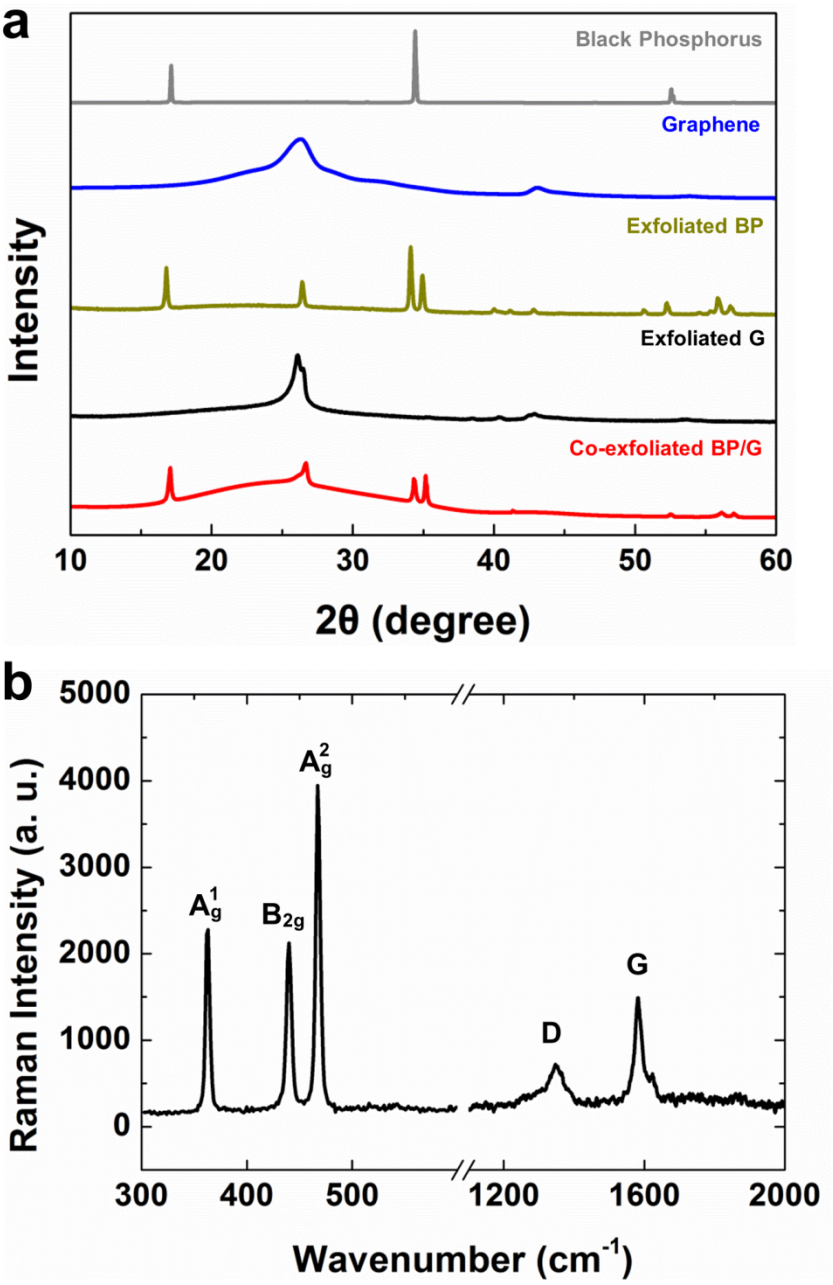

Figure 5.3 (a) XRD patterns of bulk BP, bulk G, exfoliated BP, exfoliated G, and co-exfoliated BP/G, and (b) Raman spectra of BP/G heterostructured materials assembled through EPD.

To evaluate the benefit of heterostructured BP/G materials, coin-cell battery

electrodes were prepared by directly cutting the stainless steel electrode after EPD without adding binder or conductive carbon additive. Whereas BP has been recently demonstrated to have the highest known sodium storage capacity compared to all host insertion anodes, the large volumetric expansion associated with sodium alloying with BP leads to rapid capacity degradation. Here, the use of EPD combined with bulk solution processing enables thick electrodes composed of microscopically heterostructured building blocks. Electrode thickness was characterized under SEM cross-sectional imaging, and measured as ~140 μm. To test these materials, Na-BP/G metal half cells were fabricated and tested using galvanostatic charge/discharge measurements between 0.02 to 1.5 V. Figure 5.4a shows charge/discharge profiles collected at a current density of 100 mAh/g_P. The 1st-cycle discharge capacity was measured to be 2622 mAh/g_P . This is slightly higher than the known theoretical capacity of BP (2596 mAh/g) due to the high surface area of BP/G structures and the formation of the solid-electrolyte interphase (SEI) layer at the electrode-electrolyte interface in the carbonate electrolyte. Using a fluoroethylene carbonate (FEC) additive, the 1st-cycle Coulombic efficiency was measured as 75.6%, which is higher than reports without FEC electrolyte additive.[236] From the results in Figure 5.4, it is evident that the BP/G heterostructures lead to improved electrochemical performance compared to BP materials prepared in the same way. We attribute this to the ability of the BP/G network to better accommodate the volume expansion associated with the sodium alloying reaction with BP. Comparing the capacity measured in our heterostructured BP/G material to other reports on BP at currents of 100, 200, and 500 mA/g_P (Figure 5.4b),[40, 188, 197, 237] our work showed the highest specific capacity of 2365 mAh/g_P at 100 mA/g_P current density. Further,

compared to other reports of layered and heterostructured materials tested for Na-ion battery anodes (Table 5.1) at comparable cycling rates, including graphene,[200] graphene oxide,[238] MoS_2/graphene,[239] and other layered materials[240-242], our results demonstrate promising capacities for high performance sodium batteries. Galvanostatic tests at different current densities were also carried out for 100 cycles (Figure 5.4c). The stable cycling with maintained capacities of 1297, 1009, and 623 mAh/g_P at 100, 200 and 500 mA/g_P after 100 cycles demonstrated the effective role of G in the 2D BP/G heterostructured anode as a buffering matrix to accommodate BP volume expansion. This elucidates the role of the heterostructure toward improved cycling, which has been observed in other 2D material/graphene hybrid structures used in Na-ion batteries.[239, 241] Xie et al. observed that heterostructured MoS_2/graphene materials enabled improved cycling performance up to 300 cycles for Na-ion batteries.[201] Our results demonstrate that hybrid architectures for BP/G materials can therefore enable stable high capacity performance with more suitable electrochemical potentials for coupling into a Na-ion cell compared to 2D TMDs.[243]

Table 5.1. Electrochemical performances comparison with other layered materials and heterostructures as sodium-ion battery anodes.

SIB Anode	1st cycle	Cycling
Graphene [Ref 79]	270 mAh/g at 200 mA/g	~118 mAh/g at 1200 mA/g for 8000 cycles
RGO paper [Ref 238]	500 mAh/g_{anode} at 100 mA/g	~100 mAh/g at 100 mA/g for 1000 cycles
MoS_2/Graphene paper [Ref 239]	943 mAh/g_{total} at 25 mA/g	214 mAh/g at 100 mA/g for 5 cycles
2D MXene/SnS_2 [Ref 240]	882 mAh/g at 100 mA/g	407 mAh/g at 100 mA/g for 200 cycles

Few layer SnS_2 on few layer RGO [Ref 241]	~850 mAh/g at 100 mA/g	649 mAh/g at 100 mA/g for 6 cycles 469 mAh/g at 800 mA/g for 1000 cycles
Porous 2D MXene [Ref 242]	641 mAh/g at 100 mA/g	180 mAh/g at 100 mA/g for 200 cycles
This work*	1183 mAh/g_{total} at 100 mA/g	648 mAh/g_{total} at 100 mA/g for 100 cycles

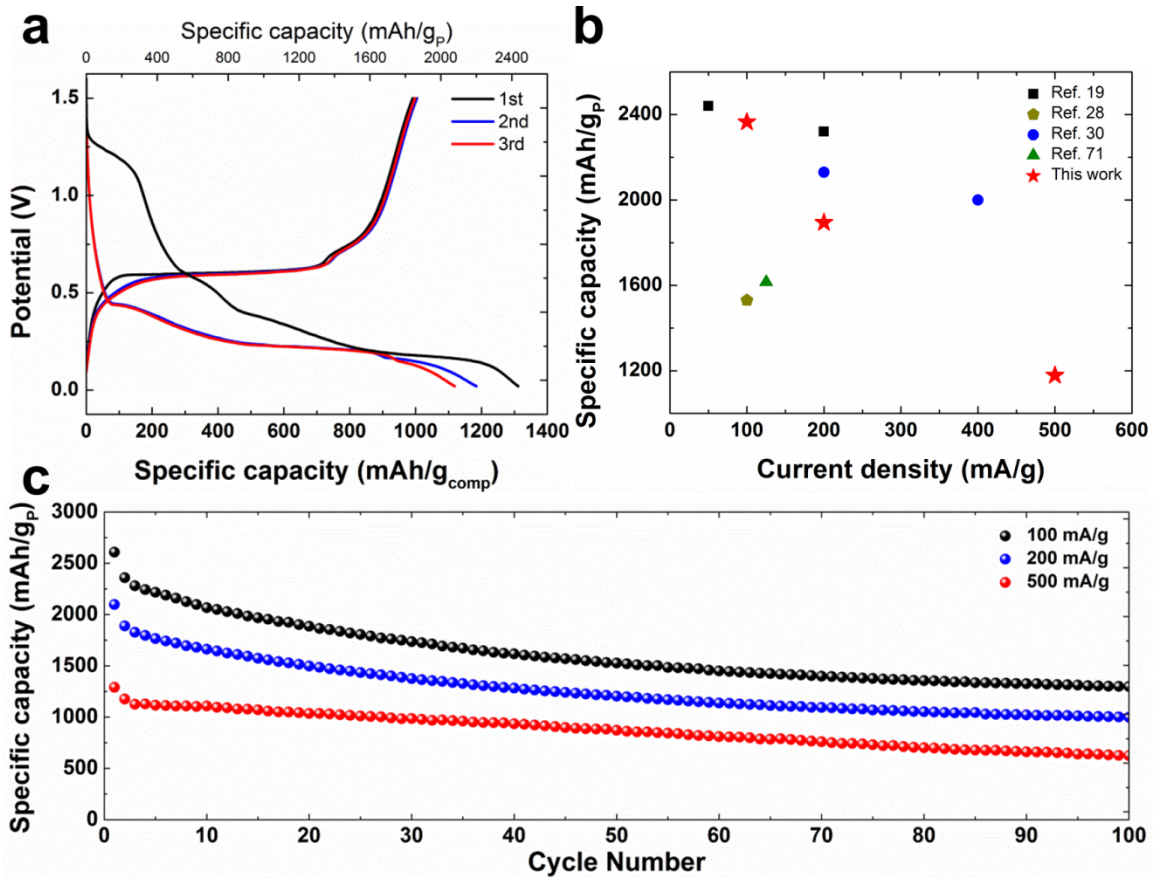

Figure 5.4 (a) Galvanostatic charge/discharge profiles for 2D BP/G heterostructure anode at current density of 100 mA/g_P between 0.02-1.5 V. (b) Specific capacities obtained by BP electrode at different current densities in this work compared to those in other literatures. (c) Cycling performance at different current densities up to 100 cycles.

Overall, our results pave the way toward the ability to prepare highly functional materials composed of 2D heterostructured building blocks by exploiting the native electrostatic interactions of 2D materials during exfoliation or liquid processing. Whereas here we show the effectiveness of this technique for batteries, leveraging the exceptional sodium alloying capacity of 2D BP nanosheets, we expect this approach to be useful for other applications such as multifunctional composites, flexible electronics, filtration and water purification, and optoelectronic devices, among others. The ability to simultaneously control organization of nanostructures from the microscale where 2D materials can stack into heterostructured building blocks, to the macroscale where the building blocks can be controllably formed into 3D functional materials represents an exciting frontier in nanomanufacturing that builds the foundation of future technologies for 2D or other nanostructured materials.

5.4 Conclusion

In summary, our work demonstrated how combining co-exfoliation of BP/G 2D materials can lead to heterostructured building blocks that can be controllably assembled into thick and functional films using EPD. Due to the high specific sodium alloying capacity of BP materials, we demonstrate this material to enable high specific capacities of 2365 mAh/g_P, 1894 mAh/g_P, and 1456 mAh/g_P at 100, 200, and 500 mA/g_P rates, respectively. These heterostructured electrodes were shown to exhibit stable cycling performance of the BP due to the ability to accommodate the volume expansion associated with sodium alloying into the BP/G heterostructured material network. Collectively, our work gives promise to manufacturing heterostructured 2D materials at two length scales

simultaneously: first the control over stacking based on the electrostatic interaction of 2D materials in solution to produce heterostructured building blocks, and second the ability to deposit such heterostructured materials in thick functional coatings through electrophoretic deposition. In combination, this route gives promise to overcome materials and scaling challenges for next-generation applications, and we demonstrate this idea here in the context of efficient sodium battery anodes.

CHAPTER 6

SULFUR VAPOR-INFILTRATED 3D CARBON NANOTUBE FOAM AS HIGH AREAL CAPACITY LITHIUM-SULFUR BATTERY CATHODES

6.1 Introduction

Lithium-sulfur (Li-S) battery cathodes are a promising replacement for lithium-ion cathodes due to earth abundance and low cost of sulfur, non-toxic nature of cathode materials, and extraordinary theoretical capacity (~1675 mAh/g) many times that of traditional cathodes.[138-139, 142, 145, 244-247] The high theoretical energy density (~2600 Wh/kg) of Li-S batteries is about 3~5 times higher than conventional Li-ion batteries.[246, 248-250] However, to achieve mass performance approaching this theoretical value, the insulating nature of sulfur, large volume expansion, and polysulfide dissolution remain challenges.[142, 156, 245, 251-252] Specifically, the electrochemical reaction between lithium and sulfur first results in high-order polysulfides (HOPSs; Li_2S_8, Li_2S_6, and Li_2S_4) that are soluble in widely used ether-based electrolytes and lead to sulfur mass loss from the cathode. The irreversible loss of HOPSs in the electrolyte leads to poor conversion of low-order polysulfides (LOPSs, Li_2S_2 and Li_2S), and result into poor capacity and cyclability.[248, 253-256] Previous research has focused on using several strategies to solve these problems, with conductive composite material fabrication,[151, 253, 257-261] structural confinement design,[146, 155, 262-265] polar binding additives,[261, 266-269] and additional interlayer configuration.[270-272]

Whereas these advances continue to emerge, an engaging area of research has focused on developing routes to maintain the high gravimetric capacity associated with stable sulfur cathodes in electrode architectures where high areal loading and high areal capacity are achieved. This requires scaling-up of fundamental nanoscale design rules to

thick electrode architectures that are at minimum competitive with the areal capacity of commercial lithium-ion battery cathodes, which is generally between 2-4 mAh/cm^2.[142, 247, 273-277] Achieving cathodes that maintain gravimetric capacity at substantially higher loading results in less external packaging weight, lower cost associated with expensive current collector materials, and better energy density at the cell level resulting from less inactive material. However, design challenges emerge for high areal capacity electrodes that are not relevant in thinner electrode architectures and three separate approaches have been primarily used in state-of-the-art efforts. The most widely utilized technique for fabricating sulfur cathode composites is melt infiltration, where bulk carbon and sulfur powder are heated (typically overnight) in a furnace to produce a composite.[278-282] These are then mixed with binders and cast in thick slurry coatings to achieve high areal loading. The critical limitation of this technique is the lack of control over the location of insulating sulfur deposits, which inhibit conductive carbon-carbon material interfaces that are critical to achieve full electrical connectivity of the thick electrode and full sulfur conversion. Another prominent route has involved the use of interlayers,[269, 283-284] where a thick interlayer or membrane is cast over typically elemental sulfur electrodes to overcome polysulfide shuttling, but only utilizing sulfur as active material. The limitation of this approach is that researchers often achieve high areal capacities at the expense of including excess electrochemically inactive mass that lowers the total electrode gravimetric performance and compromises improvements in cell-level energy density over lithium-ion. Currently the most commonly accepted technique for high areal capacity electrodes is the use of a catholyte electrolyte where the carbon electrode is preformed, species known to be soluble are loaded into the electrolyte, and solid sulfur

deposits form at the host during operation.[285-287] Whereas this technique yields the highest recorded areal capacity,[285] the requirement of sulfur-containing electrolytes ushers in new challenges for packaging and manufacturing since cathode development is dependent upon electrolyte properties.

In this work, we demonstrate a new technique, whereby we combine the benefit of a pre-formed carbon-based electrode that is a strength of the catholyte approach, with spatial control of sulfur infiltration at high mass loadings (~ 79 wt.%) directed by capillary thermodynamics, to produce a sulfur-carbon composite cathode. As a host material we utilize carbon nanotube (CNT) foams, as these are low-density interconnected sponge-like materials that can be produced in thick structures using solution processing methodologies.[288-292] The capillary loading of sulfur directs the infiltration on the interior of CNTs, leaving conductive CNT-CNT electrical pathways unimpeded by insulating sulfur deposits to enable accessible thick electrode geometries. Further, after vapor infiltration we mechanically compress these low-density materials into electrodes that maintain density above 0.2 g/cm^3 and overcomes limitations of highly porous and low volumetric density electrode designs. Based on this approach, we observe electrodes that exhibit high areal capacities of 19.3 mAh/cm^2 at mass loading of 19.1 mg/cm^2 with gravimetric capacity of 1039 mAh/g_S. Whereas this is among the highest composite cathode performance reported to date, second only to one report on catholyte-infiltrated cotton,[285] our calculations emphasize this areal capacity to be at a level where significantly improved areal capacity is less important to the packaged cell energy density compared to the degree of sulfur utilization which is proportional to energy density.

6.2 Methods

6.2.1 Fabrication of 3D CNT foam

Multi-wall carbon nanotubes (MWCNTs) (diameter~8-15 nm, length~10-50 μm, ash<1.5 wt%) were added into ethanol to form a ~2.4 mol/L solution. The solution was sonicated for 3-5 minutes by a probe sonicator (Sonics, VCX750, 30% amplitude) to form a flocculent. The process of solvent exchange was then performed by adding ultrapure Milli-Q water (18.2 Mohm) into the MWCNTs solution, and followed by pipetting the solvent out several times until the flocculent was uniformly distributed in water-based solution. Then the solution was chilled to -80 ℃ for an hour, and then transferred immediately into a vacuum chamber. Vacuum-drying was carried out to ensure all of the ice directly sublimates. After drying overnight, a fluffy and light-weight CNT foam with porous structure was achieved.

6.2.2 Sulfur vapor-phase infiltration into 3D CNT foam as cathode materials

Sulfur powder and 3D CNT foam were placed separately inside a sealed stainless-steel reaction chamber, with the 3D CNT foam suspended ~1 mm above the sulfur reservoir. The chamber was then heated up to 175 ℃ for 3 hours. After the chamber cooled down, sulfur infiltrated 3D CNT foam was taken out and pressed and cut into electrodes by razor blade with a size ~4 mm x 4 mm.

6.2.3 Characterization

The morphology and structure of pristine foam, sulfur infiltrated foam, and pressed sulfur infiltrated foam were characterized by Zeiss Merlin Scanning Electron Microscope (SEM) and FEI Transmission Electron Microscope (TEM). Elemental mapping was

performed by SEM and STEM energy dispersive X-ray spectroscopy (EDS). The mass loading of sulfur was measured by massing the carbon foam before and after sulfur infiltration, and confirmed through themogravimetric analysis (TGA).

6.2.4 Electrochemical tests

The pressed sulfur infiltrated foam with a size of ~4 mm x 4 mm was directly applied as cathode material, and then assembled into CR 2032 type coin cell inside Ar filled glovebox with lithium foil as counter electrode, 2500 Celgard separator, and 1M LiTFSi (Sigma Aldrich, 99.95%), 0.25 M LiNO3 (Sigma Aldrich, 99.99%) in a dimethoxyethane (DME, Sigma Aldrich, anhydrous 99.5%) and 1,3-dioxolane (DOL, Sigma Aldrich, anhydrous 99.8%) with a volume ratio of 1:1 as electrolyte. Galvanostatic charge/discharge tests were performed at 0.1 C (1 C = 1675 mA/g) between 1.8 to 2.6 V.

6.3 Results & Discussion

Three dimensional (3D) CNT foams were fabricated by vacuum freeze-drying of water-dispersed CNTs to result in a freestanding and lightweight foam as shown in the photograph in Figure 6.1a with a scheme shown in Figure 6.1b. A typical low-density foam shown in Figure 6.1e has a dimension of ~1.8 cm x 0.9 cm x 0.8 cm and a weight of 7.0 mg. The backbone of the CNT foam involves flake-like CNT sheets (Figure 6.1c, 6.1f) composed of interconnected CNTs (Figure 6.1d, 6.1g) and is a result of material agglomeration in solution prior to freeze-drying. The hierarchical porous structure of the 3D CNT foam ranges from macropores in-between the carbon flakes where ice was removed during the vacuum freeze-drying process, to meso- and micropores that results from interconnected CNTs to provide high surface area.

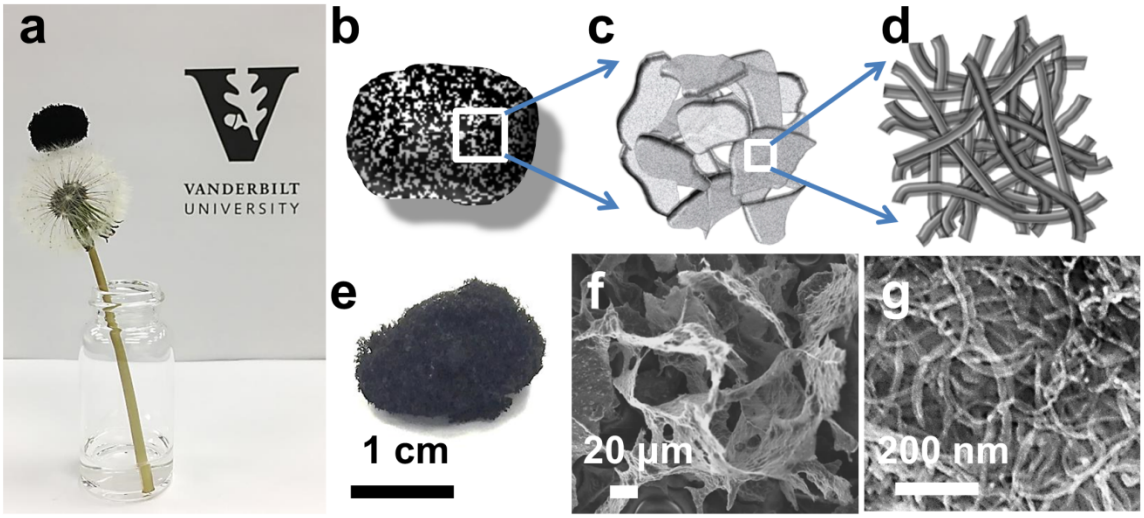

Figure 6.1. (a) Ultra-light CNT sponge with a size of ~1.5 cm x 0.8 cm x 0.2 cm standing on a dandelion. Schematic illustration (b) bulk 3D CNT foam, (c) carbon microscale morphology formed during solution processing, and (d) interconnected CNTs that make up structure corresponding to SEM imaging. (e) Photograph of a typical 3D CNT foam. SEM images of (f) the 3D CNT foam with carbon flakes at the microscale, and (g) interconnected CNTs with meso- and microporous features at the nanoscale.

To infiltrate sulfur into the 3D CNT foam, the foam was placed on a steel mesh and suspended ~ 1 mm above a sulfur reservoir inside a small sealed steel vessel. Infiltration was carried out by heating the vessel to 175 ℃ for 3 hours, and utilizing the sulfur vapor generated from molten sulfur within the free space inside the reaction chamber. The high vapor pressure within the small chamber drives sulfur to be condensed onto the CNTs *via* capillary effect. Unlike melt infiltration, where a liquid is placed in contact with the cathode material for duration that most commonly extends overnight, this technique involves a shorter duration of exposure, no physical contact between sulfur and CNT foam, and no excess or wasted sulfur material. SEM energy dispersive x-ray

spectroscopy (EDS) mapping of the sulfur-3D CNT foam (Figure 6.2a) confirms uniform loading of sulfur into the CNT foam (Figure 6.2b and 6.2c). The visible macroporous features function to enable uniform and rapid penetration of the sulfur vapor into the CNT material and to achieve uniform high mass loading. Transmission electron microscopy (TEM) and scanning TEM EDS (STEM EDS) elemental mapping confirms the uniform loading of sulfur on nanoscale features (Figure 6.2d-2e). The scheme in Figure 6.2f specifically demonstrates sulfur filling the interior of CNTs during the isothermal vapor-phase infiltration process, which occurs due to thermodynamic capillary condensation. Here the surface tension of the sulfur on the interior of CNT maintains a negative radius of curvature that leads to pressure difference ($\Delta P = 2\sigma/r, r < 0$) compared to the vapor environment, and then leads to rapid continuous filling until the interior pressure saturates.[151, 293] Besides rapid interior filling, sulfur also forms condensation on the exterior of CNTs due to capillary.[294] STEM EDS elemental mapping of an individual CNT (Figure 6.2g-2i) demonstrates this observed mode of filling. In the line scan, the narrowed sulfur peak relative to carbon peak confirms the existence of sulfur on the interior of the tube.

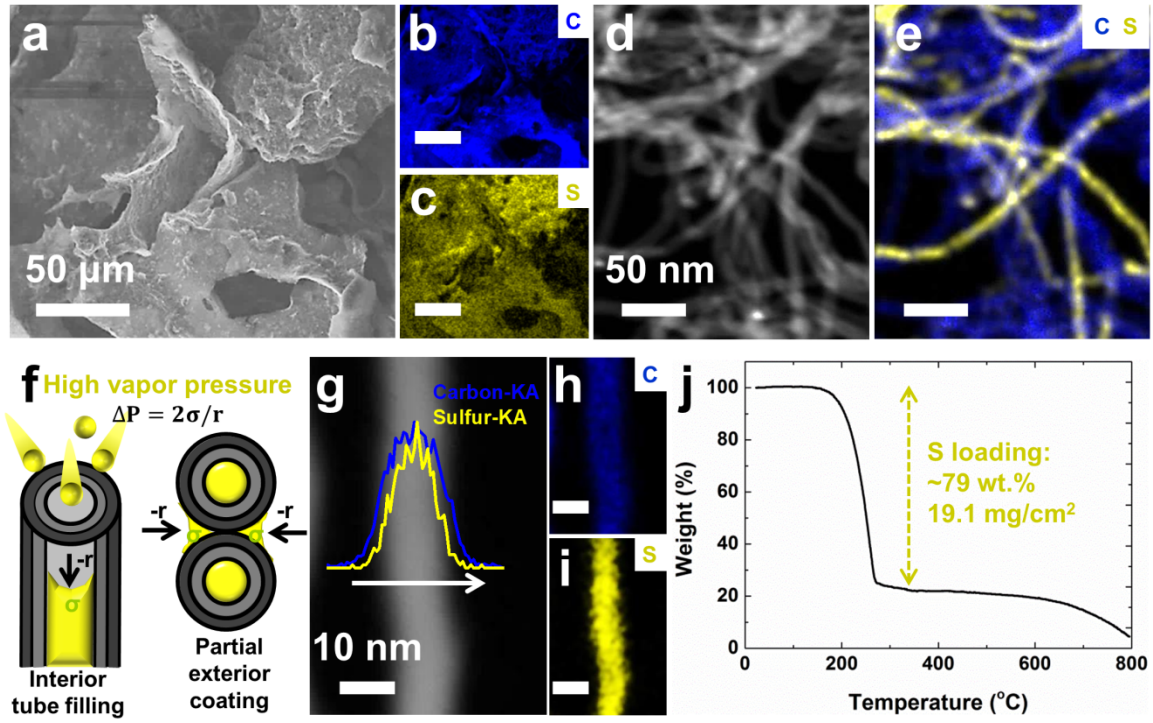

Figure 6.2. a) SEM image of zoomed-in view of sulfur-3D CNT foam. SEM EDS elemental mapping of (b) carbon and (c) sulfur (with scale bars = 50 μm). d) TEM image of sulfur-filled CNTs with EDS elemental mapping of e) carbon and sulfur (with scale bar indicating 50 nm). (f) Schematic illustration of capillary-driven sulfur filling the interior of tube and partially coating the exterior of CNT during vapor-phase infiltration. (g) TEM line scan of a single CNT filled with sulfur, and corresponding STEM EDS elemental mapping of (h) carbon and (i) sulfur (with scale bars = 10 nm). (j) TGA data for sulfur loading onto the 3D CNT foam.

Further analysis of the sulfur-3D CNT foam demonstrates a mass loading of 79 wt.% as confirmed through thermogravimetric analysis (TGA) along with areal loading reaching 19.1 mg/cm^2 (Figure 6.2j). Whereas the interior of the CNT is favorable for capillary filling, this high gravimetric loading combines coating on exterior surfaces and

interior surfaces, the former of which have a lower radius of curvature, causing slower capillary condensation.[294] While achieving high mass loading, the interior filling promise a much thinner exterior coating that will not result into insulating CNT-CNT junctions compared to traditional melt-infiltration method. Notably, this is extremely high areal loading compared to current state-of-the-art in composite cathodes formed in the solid state.

After sulfur infiltration, the cathode material is mechanically compressed into a densely packed carbon-sulfur composite. This eliminates macroporous networks that are advantageous for sulfur infiltration, but consume large amounts of unutilized electrolyte in a packaged device configuration (Figure 6.3a). The compressed cathode material was further cut into pieces for coin-cell battery fabrication (Figure 6.3b-3c). The mechanical integrity of the 3D CNT foam enabled ease of use for conventional processing, such as blade cutting, to prepare electrode samples. SEM imaging of compressed cathodes reveal suppression of the CNT flake-like sheet structures, but the interconnected CNT structure at the nanoscale is maintained (Figure 6.3d, 6.3e). The uniform infiltration of sulfur in the CNTs was also maintained without any delamination after compression due to the uniform sulfur coating mechanism that preserves conductive CNT junctions (Figure 6.3f-3g). The actual thickness of the compressed electrode inside the coin cell is about ~150-200 μm.

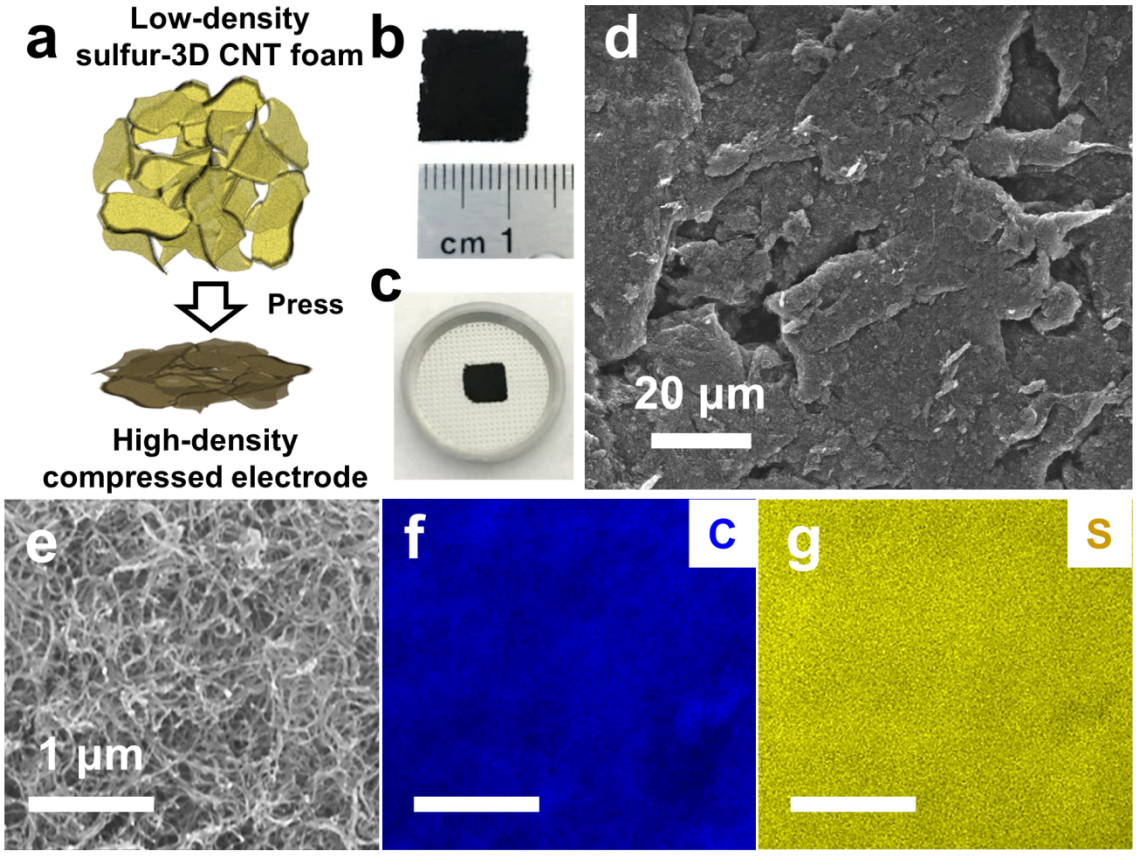

Figure 6.3. (a) Scheme depicting the method to form compact CNT foam electrodes. Optical images of (b) compressed sulfur-infiltrated CNT foam and (c) compressed electrode that was directly cut from the compressed foam by razor blade to fit in a coin-cell. (d) SEM image of mechanically compressed sulfur-3D CNT foam. (e) SEM image of interconnected CNTs in sulfur-3D CNT foam and corresponding EDS mapping of (f) carbon and (g) sulfur (with both scale bars indicating 1 µm).

To assess the electrochemical performance of the sulfur-3D CNT foam with high areal loading, galvanostatic charge/discharge studies were performed on the compressed sulfur-3D CNT foam composite cathode at 0.1 C (1C=1675 mA/g; 3.2 mA/cm^2). With an initial activation process, the sulfur-3D CNT foam delivered a discharge capacity 1039

mAh/g_S in the 2nd cycle, which corresponds to an areal capacity of 19.8 mAh/cm^2. To the best of our knowledge, this is the highest value compared to the state-of-the-art literature reporting performance for sulfur-3D carbon composite cathodes to date. The remarkable sulfur utilization of our cathode results from uniform interior and exterior coatings of sulfur on CNTs, which provides enough surface area to sustain high gravimetric loading with the sulfur remaining in close enough proximity to conductive CNTs to produce thick and electrically accessible electrodes. The upper and lower voltage plateau on the discharge curves in Figure 6.4a represents the high order polysulfide (HOPS) and low-order polysulfide (LOPS) conversion processes, respectively. The LOPS/HOPS ratio is a comparison that reflects the cathode reversibility, and exhibits values from 2.2 on the 2^{nd} cycle to above 2.4 on the 5^{th} cycle, which demonstrates cycling stability and approaches the theoretical maximum value of 3. This performance implies a cathode architecture that is effective in both enabling high sulfur utilization with fast conversion kinetics to trap soluble polysulfides before significant outward diffusion of the electrode occurs.

To compare the results from our cathodes to the trend of cathode development that has engaged a significant research crowd in the battery community, we plotted areal loading and capacity delivered by sulfur-3D carbon cathodes to several previous works selected for their notably high areal performance (Figure 6.4b). Whereas our foams exhibit lower areal performance than cotton-derived carbon cathodes through the catholyte approach recently pioneered by the Manthiram group,[285] our results exhibit higher areal loading and performance relative to all other previous reports and specifically the highest value compared to relevant solid sulfur-carbon composite routes

that remain most synergistic with conventional battery manufacturing methodology. Specific numbers and details for points on these curves are further shown in Table 6.1. To better understand the stability of this high areal performance, 100 consecutive charge-discharge cycles were carried out (Figure 6.4c). Notably, even after 100 cycles of testing, the CNT foam cathode delivered areal capacity of 9 mAh/cm^2, which is over 2 times higher than the best commercialized Li-ion batteries and remains higher than the maximum performance of the majority of previous reports on sulfur cathodes. Moreover, the mechanical integrity of the composite foam electrode and porous interconnected network of CNTs were maintained after cycling. Further optimization on surface modification of CNTs could potentially allow stronger binding of polysulfides to better mitigate dissolution.

Table 6.1. Areal loading and areal capacities in high-loading Li-S battery cathodes in previously reported works.

Cathode Material	Areal Sulfur Loading (mg/cm^2)	Areal Capacity (mAh/cm^2)	Cycling rate
Mesoporous carbon-CNT-sulfur microspheres	5	4	C/5
Thick sulfur cathode	3.5	4.5	C/10
3D sulfur-coated carbon fiber foam	16.5	16.3	C/10
Sulfur infultrated-MWCNT porous microspheres	2.5	2.66	C/10
3D carbon cotton infiltrated with catholyte	61.4	56.05	C/10
Layer-by-layer sulfur-porous carbon nanofiber	11.4	11.3	C/5
Li_2S_6 impregnated N,O-codoped porous hollow carbon fibers	6.2	6.2	C/3
Sulfur cathodes with CNF interlayer	1.4	2.1	C/5
Sulfur-Nitrogen-doped carbon composites	5	6	C/10
Nanopowder carbon-sulfur composite with graphene oxide interlayer	1.2	1.4	C/2

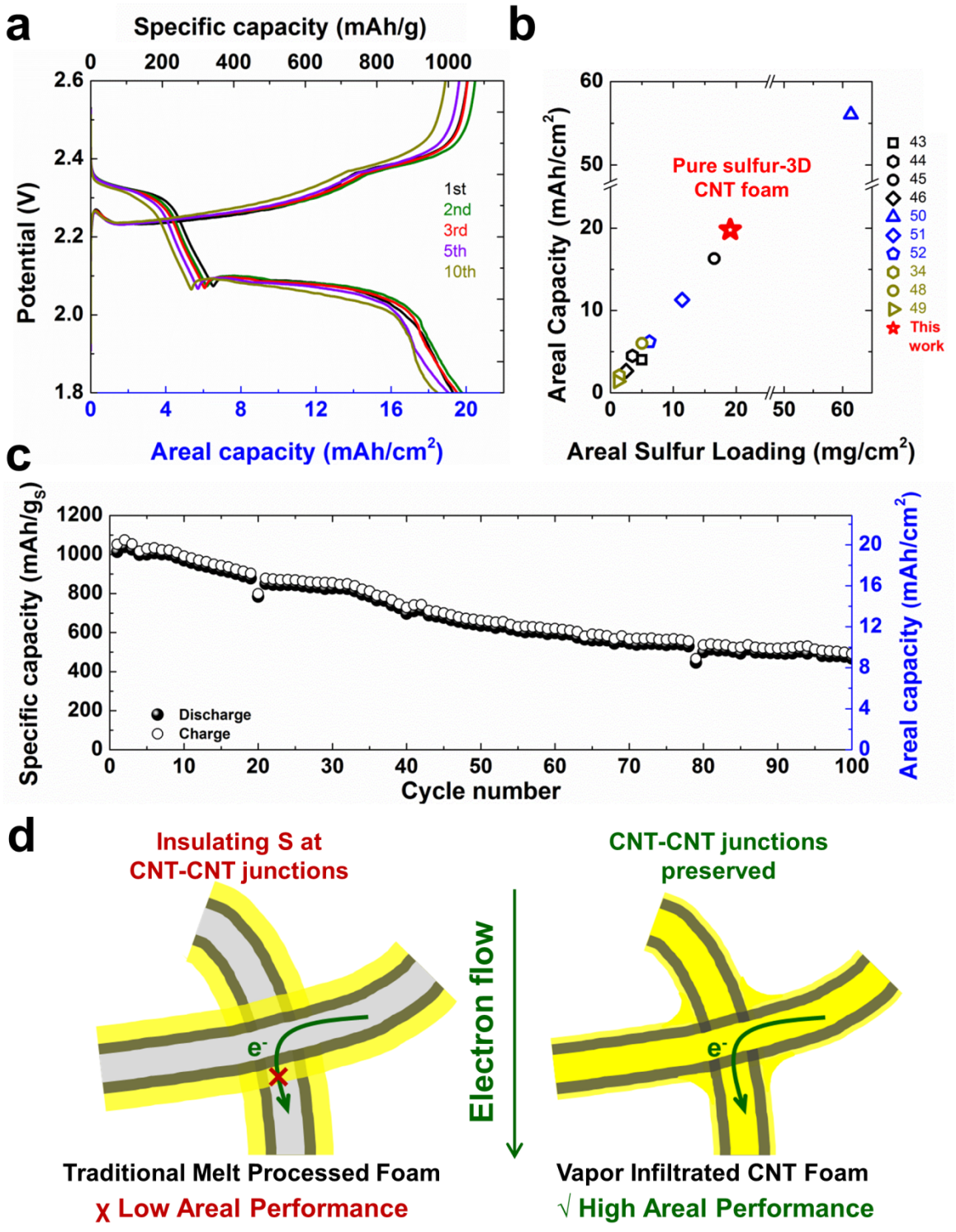

Figure 6.4. (a) Galvanostatic charge/discharge curves of the sulfur-3D CNT foam at 0.1 C. (b) Areal loading and areal capacities in high-loading Li-S battery strategies described in previously reported works (black: melt-infiltration method, blue: catholyte infiltration

method, yellow: interlayer method, and red: our work). (c) Cycling performance of sulfur sulfur-3D CNT foam at 0.1 C. (d) Scheme to demonstrate difference between traditional (melt-infiltrated) composite cathode sulfur-3D CNT foam composite cathode.

To illustrate the design rationale of this electrode architecture that enables high areal performance, we compare our approach to the conventional solid-state composite approach in the literature that requires melt diffusion (Figure 6.4d). In previous studies, the use of melt diffusion leads to sulfur deposits that are uncontrollable by the long thermal treatment of bulk sulfur which results into thick coating onto host materials. These nanostructures are then processed into slurry electrodes without design control over charge transport pathways, which poses a challenge when achieving high gravimetric loading of insulating sulfur. In contrast to this, the use of vapor infiltration into CNT foams alleviates the critical issues associated with this approach. First, the formation of a low-density conductive solid from solution processing prior to sulfur infiltration embeds interconnected CNTs that provide a conductive skeleton for the electrode. Next, the use of capillary thermodynamics to infiltrate sulfur into the CNT foams ensures a conformal sulfur coating on the interior and/or exterior of the CNT that by its mechanistic nature prevents the formation of thick, insulating deposits. This is because the self-limiting coating process deactivates as the chemical potential of the coated sulfur approaches that of bulk liquid sulfur. When compressed into a compact electrode, the sulfur remains electrically addressable and the thick CNT material remains interconnected and conductive to produce a high areal capacity electrode.

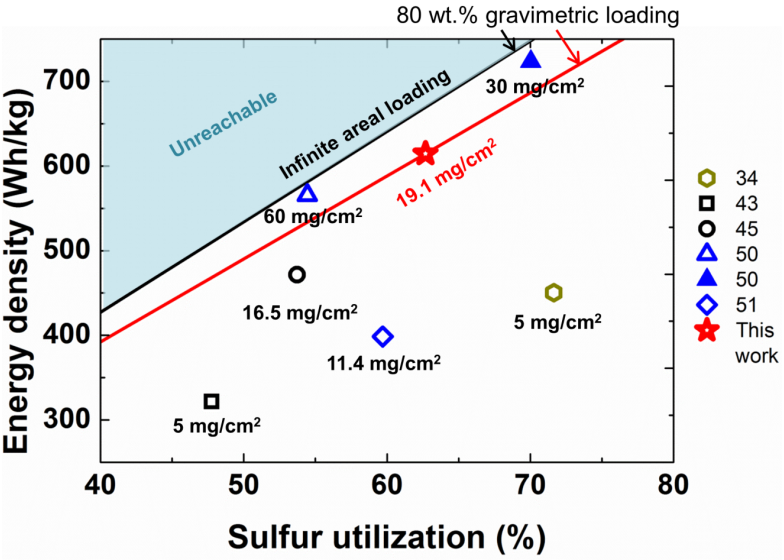

Figure 6.5. Energy density calculated assuming an ideal lithium metal anode, conservative packaging, and based on Li-S battery cathodes from our work compared to the work of other teams reporting high areal performance. Packaging weight considerations include 32% for electrolyte (fixed), 10% for external/diagnostic packaging (fixed), 2% for separator (fixed), and 15% for current collectors that varies based on areal loading. Here, "infinite" areal loading is the asymptotic limit where mass of current collectors is negligible relative to electrode active materials. Lines running from left to right indicate constant areal loading with varying sulfur utilization. (Assuming 80 wt.% mass loading for all lines as ideal-case comparison) This calculations emphasizes small gains in energy density can be widely offset by low sulfur utilization, making this a critical parameter for high areal loading strategies.

Whereas areal capacity remains an important metric in efforts to develop stable cathode architectures for batteries with a target energy density > 500 Wh/kg, we note that at high areal capacities, it is critically important to consider sulfur utilization as a design

parameter for a Li-S battery. To illustrate this, we show a plot of ideal energy density for a fully packaged Li-S battery, where the sulfur mass loading is assumed 80 wt.%, and sulfur cathode performance is coupled with an ideal Li metal anode (see Figure 6.5). The energy density is calculated as a function of sulfur utilization as well as areal performance.

Energy density calculation

Energy density was calculated based on full cell architectures involving pure Li metal anodes with ideal performance, external and internal packaging, and based on the measured cathode performance in our work and other works. The general basis for energy density is given by the following equation:

E = Capacity x Voltage x Sulfur mass loading x Sulfur ratio in Li_2S x packaging

-Voltage: assuming 2.1 V for all for ideal-case comparison

-Sulfur mass loading: assuming 80 wt% for all for ideal-case comparison, or the reported sulfur mass loading of other studies.

-Sulfur ratio in Li_2S: 0.69 ($= \frac{\text{Number of sulfur atoms in } Li_2S \times \text{Sulfur molar mass}}{\text{Molar mass of } Li_2S}$, sulfur mass percentage in the final product Li_2S)

-Packaging: in a full battery system, we assume electrolyte+separator+packaging in total to account for 45 % of the weight (see ref. [56]). Except for the above elements, other packaging includes weight of current collector and active material yielding total 55% of the weight. For the "infinity loading" case where the mass of the collector is negligible to the mass of the active materials, the 55% weight should all be active cathode materials, so packaging should be 55%. In a practical future 18650 Li-S cell with 6 mg/cm^2 areal loading, the weight percentage of cathode electrode materials is 15%.[295] Based on this

assumption, a cell with x mg/cm^2 areal loading, the cathode material ratio in other packaging will be: $55\% - \frac{6\,(\frac{mg}{cm^2})\times 15\%}{x(\frac{mg}{cm^2})}$, for example, the packaging factor for a 20 mg/cm^2 areal loading cell should be: 55%-4.5%=50.5%.

Built into this calculation are the following packaging considerations: (1) an electrolyte composition of ~33 wt.% that is about double that of conventional Li-ion cells due to the increased electrolyte requirement from the polysulfide shuttling effect, (2) current collector composition of 15 wt.% that varies with areal loading, where at "infinite" areal loading the mass of the collector material is negligible compared to the electrode active material mass, (3) separator of ~2 wt.%, and (4) external packaging and battery diagnostics of ~ 10 wt.%.[296] In all cases, it is assumed the ideal Li metal anode has areal capacity matching that of the cathode and exhibits ideal behavior – a concept currently the focus of broad and extensive research efforts. On this plot, we present our results in comparison to other key work in noted references. Importantly, this demonstrates the important principle that the highest measured areal loading does not directly correlate to the highest cell energy density. In fact, our results with areal loading of 19.1 mg/cm^2 demonstrate a simulated energy density that is superior to the result of 60 mg/cm^2 loading – the highest result in the literature. This is due to the linear trend of increasing energy that correlates with sulfur utilization and the non-linear trend of increasing energy density with increasing areal loading. In other words, at extremely high areal loading (> 20 mg/cm^2), large increases in areal loading provide only minimal further increases to energy density due to the finite mass of the current collector material, whereas achieving higher sulfur utilization still linearly increases the total energy density. In this regard, the results reported by Manthiram's team with areal loading ~ 30 mg/cm^2

exhibits a higher sulfur utilization and significantly higher energy density than those of the cathodes with ~ 60 mg/cm^2 areal loading,[285] which are higher than our results and breaks common intuition in the research arena that high areal loading at the expense of sulfur utilization is acceptable. Based on this idealized calculation, we deduce a simulated energy density of ~ 600 Wh/kg from our CNT foams and can be targeted to exceeding 700 Wh/kg theoretically by further improving the sulfur utilization, which provides a significant opportunity to engineer artificial interfaces on the anode side and maintain > 500 Wh/kg in a full cell configuration, which is a primary target of battery technology in coming years.

6.4 Conclusion

Here we demonstrate a strategy to use solution processing to generate low-density CNT foams, utilize capillary thermodynamics to infiltrate sulfur into these foams with high mass loading (79 wt.%), and condense the foams into compact electrodes that enable high areal loading and capacity (19.3 mAh/g at 19.1 mg/cm^2). Compared to melt-infiltration approaches where high areal capacity is bottlenecked by thick sulfur deposits formed at electrically conducting interfaces, our work builds upon the formation of a thick conductive CNT foam prior to vapor phase sulfur infiltration to preserve critical charge conduction pathways and enable electrical accessibility through thick electrodes. Whereas our findings are among the highest reported values of areal performance documented in the literature, our calculations that emphasize that further improvements to energy density are best achieved by improvement of sulfur utilization as opposed to current developmental trends of further widely increasing areal loading and capacity. Overall, this paves a route toward a practical battery architecture with > 500 Wh/kg

energy density that remains a key target for the battery community. Finally, we emphasize how the approaches used in this work can be broadened to include a variety of different nanostructured building blocks to broaden this technique a battery oriented nanomanufacturing scheme where capillary forming thermodynamics and nanomaterial building blocks in low-density 3-D architectures can be combined to form composite structures for a wide range of applications.

CHAPTER 7

CARBON NANOTUBE FOAM FOR EFFICIENT ELECTROCHEMICAL REMOVAL OF CHROMIUM (VI) FROM AQUEOUS SOLUTION

7.1 Introduction

Carbon can be arranged into nanomaterials that possess unique electrical,[1, 3] mechanical,[6-7] and chemical properties[8-9] desired for small-scale applications while maintaining low-density. The nanoscale properties of carbon nanomaterials can be further engineered by incorporating other functional nanomaterials, which can result into synergistic effects that are beneficial for certain applications.[297-301] However, macroscale assembly of these nanostructures often compromises the desired properties due to their low-density nature and poor interconnection.[302-305] Thus, proper approaches and scalable techniques are crucial to assemble appropriate carbon nanomaterials and fabricate carbon nanocomposites into 3D architectures for large-scale applications such as solving environmental problems.

Among many kinds of environmental problems, water pollution has been one of the biggest problems. Chromium is a primary heavy metal pollutant in contaminated water, which commonly exists in waste effluent of tanning, plating, and welding industries.[306] Between the two common oxidation states of Cr, trivalent chromium-Cr (III) is an essential dietary element in human body, and is insoluble in water.[307] While Cr (VI), is extremely toxic and carcinogenic, and can be diffused into groundwater and soil unrestrictedly.[308] Exposure or uptake of Cr (VI) contaminated water can cause health-threatening problems such as inflammatory skin,[309] respiratory tract irritation,[310] DNA damage,[311] and lung cancer[312]. Considering the above disadvantageous effects of

chromium on the surroundings, it is thus essential to efficiently remove Cr (VI) from industrial waste.

Previous research has reported several Cr (VI) removal approaches by using carbon nanomaterials.[313-317] Because of the high surface area and desired surface chemistry, carbon nanomaterials have been demonstrated to achieve high Cr (VI) removal efficiencies by adsorption and reduction.[317-319] Due to the absolute physical process, adsorption can be slow and may take up to several hours or even a day to reach maximum Cr (VI) removal efficiency.[320-321] The powder-type carbon nanomaterials adsorbents have been reported effective in removing low-concentration Cr (VI) in aqueous solution (<10 mg/L)[322-324] and often require further membrane filtration to be separated from the solution. However, when the waste effluent has a high concentration of Cr (VI), primary removal methods must be performed before trace metal adsorption. Reduction of Cr (VI) to Cr (III) has also been demonstrated as an effective process in Cr (VI) removal.[325] Since Cr (III) is less toxic and insoluble in water, the final product which is usually $Cr(OH)_3$ can be easily separated from the filtrated solution.[326-327] Carbon nanomaterials that possess specific surface chemistry can be directly added to the solution or combined with other functional nanomaterials as reducing agents.[317, 328-329] Without external energy input, reduction of Cr (VI) only occurred on the surface of reducing agents, which led to comparatively lower removal efficiency.[330-331] Electrochemical reduction process, where an external current or voltage is applied to the system, usually combines electrosorption and reduction of Cr (VI), and has been demonstrated to achieve high Cr (VI) removal efficiencies close to 100% with high energy input[332-333] and adjusted pH (to ~2).[334-335] However, it is more practical to remove

Cr (VI) at neutral pH with low energy input ang high removal efficiency for further scalable water treatment.

In this work, we demonstrate a low-energy input Cr (VI) removal process, combining CNT-based foam electrodes with electrosorption and electrochemical reduction to efficiently remove high concentration Cr (VI) in aqueous solution at neutral pH. We investigate the Cr (VI) removal efficiencies by varying the initial Cr (VI) concentration, reduction time, applied voltage, and composition of electrodes for the electrochemical reduction. The removal efficiencies for pristine CNT foam improve with increasing applied voltage and reduction time, while by increasing the Cr (VI) concentration from 20 to 40 to 60 mg/L, the removal efficiency exhibit an increase from 91% to 95% and a slight decrease from 95% to 88%. The removal efficiencies of Cr (VI) by CNT foam increase with increasing applied voltage and reduction time. Besides pristine CNT foam electrodes, we also fabricated CNT-MoS_2 composite foam by incorporating exfoliated MoS_2 nanosheets into the foam architecture. For 60 mg/L Cr (VI) solution, the removal efficiency for CNT-MoS_2 composite foam electrode increases to 90%. By further investigating the energy input for Cr (VI) removal process, we observed a decrease from 0.20 Wh to 0.16 Wh by using CNT-MoS_2 composite foam electrodes due to the catalytic MoS_2 nanosheets for oxygen evolution reaction, which promotes the reduction of Cr (VI) to Cr (III). Besides, we also calculated charge efficiencies, which dictate how many charges that were put into the electrochemical system have been effectively utilized for Cr (VI) reduction, and observed an efficiency of 16% for CNT-MoS_2 foam comparing to 12% for pristine CNT foam. As a conductive material with high surface area, the CNT foam promotes the electrosorption and

reduction of Cr (VI), and thus improves the removal efficiency without need of tuning solution pH comparing to other planar electrodes in Cr (VI) electrochemical reduction process.[333] The simple set-up of our electrochemical reduction process prevented further multi-step processing such as filtrating out adsorbents or tuning the pH, which can be promising in further expanding to pilot scale for managing high concentration Cr (VI) waste effluents.

7.2 Methods

7.2.1 Carbon nanotube foam synthesis

Multi-walled carbon nanotubes (MWCNTs) (outer diameter: 8-15 nm; length: 10-50 μm; specific surface area: 233 m^2/g) are purchased from Cheap Tubes Inc. 200 mg MWCNTs were added to 40 mL ethanol solution in a 50 mL centrifuge tube. Sonication process was assisted by a probe sonicator (Sonics, VCX750, 30% amplitude) for 3 min to form the suspension, with a 3s on 3s off pulse to avoid excessive heating. Then solvent exchange process was performed by adding ultrapure Milli-Q water (18.2 Mohm) to the suspension and pipette the solvent out until a stable flocculated suspension was formed in a water-based solution. The solution was further transferred to a freeze-dryer (BIOBASE BK-FD10S), to first froze at -60 ℃ for 4 hours, and then dried under vacuum overnight until the ice sublimated. After drying, a free-standing three-dimensional CNT foam was achieved.

7.2.2 Preparation of Cr (VI) solution and electrochemical reduction set-up

Potassium dichromate ($K_2Cr_2O_7$) (ACS, 99.0% min, Alfa Aesar™) was dissolved in ultrapure Milli-Q water (18.2 Mohm) to make artificial Cr (VI) aqueous solution with

concentration of 20, 40, and 60 mg/L. 20 mL of Cr (VI) solution in a 50 mL beaker was used for each electrochemical reduction process. The electrodes were fabricated by compressing the CNT foam onto a Cu tape (3 cm × 1.1 cm) with the bottom part (0.6 cm × 1.1 cm) being covered. Mass of compressed CNT foam on each Cu tape was controlled to ~5 mg. Two identical electrodes holding by alligator clips were dipped into the Cr (VI) solution with a distance of 0.5 cm in parallel. Voltage was applied to the two electrodes, and corresponding current profile was recorded by a sourcemeter (Keithley 2400).

7.2.3 Characterization

The morphology and structure of CNT foam and CNT-MoS_2 composite foam were characterized by Zeiss Merlin Scanning Electron Microscope (SEM). Elemental mapping of composite foam was performed by SEM energy dispersive X-ray spectroscopy (EDS). UV-vis Spectroscopy of Cr (VI) solutions before and after electrochemical reduction was performed on a Varian Cary 5000 UV-vis NIR spectrophotometer (Agilent Technologies). Solution after electrochemical reduction was left overnight, and then top part was collected for UV-vis characterization.

7.3 Results and discussion

To synthesize three-dimensional CNT foam, probe sonication of CNT powders was first performed in ethanol solution to achieve a stable dispersion. DI water was then added to the solution for exchanging ethanol to water, and maintains a stable dispersion of CNTs in water. The water-based dispersion was transferred to the vacuum freeze-drying for freezing at -60 °C, after ice fully crystalizes, the frozen dispersion was dried under vacuum to let ice directly sublimates, thus to avoid structural interference on the

free-standing CNT foam. After adequate sublimation, the foam was compressed for further fabrication of electrodes for electrochemical reduction of Cr (VI). The above process was shown schematically in Figure 7.1a. Figure 7.1b showed photographs of freeze-dries CNT foam before and after compressing. SEM image of uncompressed CNT foam (see Figure 7.1c) indicated an interconnected carbon flake structure at the microscale. After compressed to foam electrodes, the macro-pores are eliminated and a compact film-like structure was formed (see Figure 7.1d). As can be seen in Figure 7.1e, the nanoscale feature of meso- and micro-pores and interconnected nanotubes are maintained after compressing.

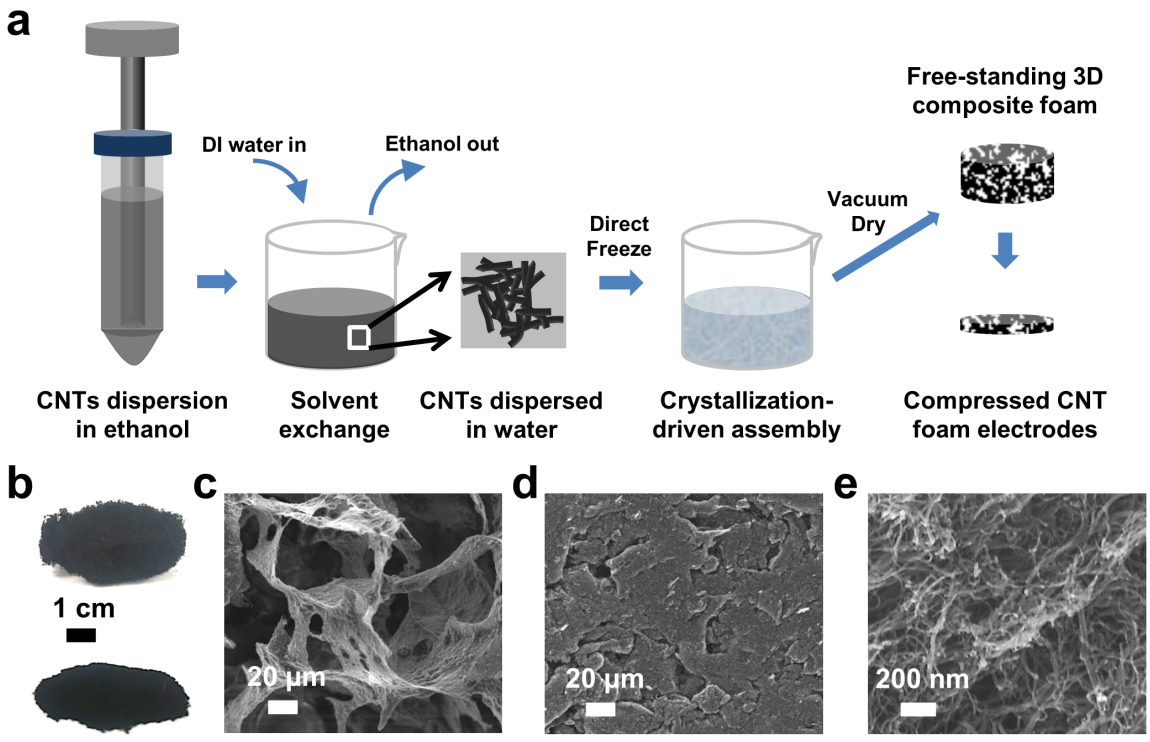

Figure 7.1. (a) Three-dimensional free-standing CNT foam synthesis scheme. (b) Photograph of a free-standing CNT foam and after compressed for electrode fabrication. SEM of (c) SEM of free-standing CNT foam with interconnected carbon network at

microscale, (d) compressed CNT foam at microscale, and (e) compressed CNT foam at nanoscale.

The compressed CNT foam electrodes were placed on top of Cu tape partially for fabrication of electrodes for Cr (VI) reduction. Two identical electrodes were in parallel facing each other, and immersed into the solution with CNT foam electrode fully exposed to Cr (VI) solution (in Figure 7.2a). The other side of the electrodes is held by alligator clips that connected to a Keithley sourcemeter for monitoring the current profile upon time and set different applied voltages. It was observed that the solution with 60 mg/L Cr (VI) turned color from bright yellow to almost clear after electrochemical reduction (see Figure 7.2b). During the process, massive bubbles are observed on the cathode side. After 15 V, 1 hr electrochemical reduction, yellow-colored flocculent was precipitated at the bottom of the container, which corresponds to the insoluble Cr (III) compounds as reduction products. Previous research have demonstrated that acidic conditions favors Cr(VI) reduction to Cr(III) where as neutral conditions is effective for Cr (III) precipitation in a combined electrocoagulation–electroflotation reactor using other electrodes such as iron.[336-337] The UV-vis spectra shown in Figure 7.2c indicated specific peak around 350 nm exhibited a sharp decrease in intensity and slight shift to higher wavenumber. The decrease of peak intensity corresponded to a successful removal of Cr (VI) and reduction to Cr (III), as have shown in several previous studies.[338-340] The low-intensity UV-vis absorption spectra (blue curve in Figure 7.2c) indicated minimal residue Cr (VI) in the solution after electrochemical reduction. A peak shift of ~20nm could be due to the pH change during electrolysis process, which may affect the electronic charge

transfer and an energetically favorable state of Cr (VI) between multiple states such as dichromate ($Cr_2O_7^{2-}$) or chromate (CrO_4^{2-}) ions.[341] Based on concentration calibration, the Cr (VI) removal efficiency for 60 mg/L Cr (VI) solution was calculated to be 88%. To confirm that the high removal efficiency results from CNT foam instead of Cu tape, control experiment was done by using two identical Cu tapes for electrochemical Cr (VI) reduction. Only few bubbles were observed at the surface of Cu tapes staying steadily, and a Cr (VI) removal efficiency of only 44% for a 60 mg/L solution at 15 V for 1 hr reduction. Even when scaling up by doubling the amount of 60 mg/L Cr (VI) solution to 40 mL, the CNT foam electrodes exhibited only a slight decrease in Cr (VI) removal efficiency from 88% to 74% comparing to Cu tape that resulted into a drastic decrease from 44% to 17%.

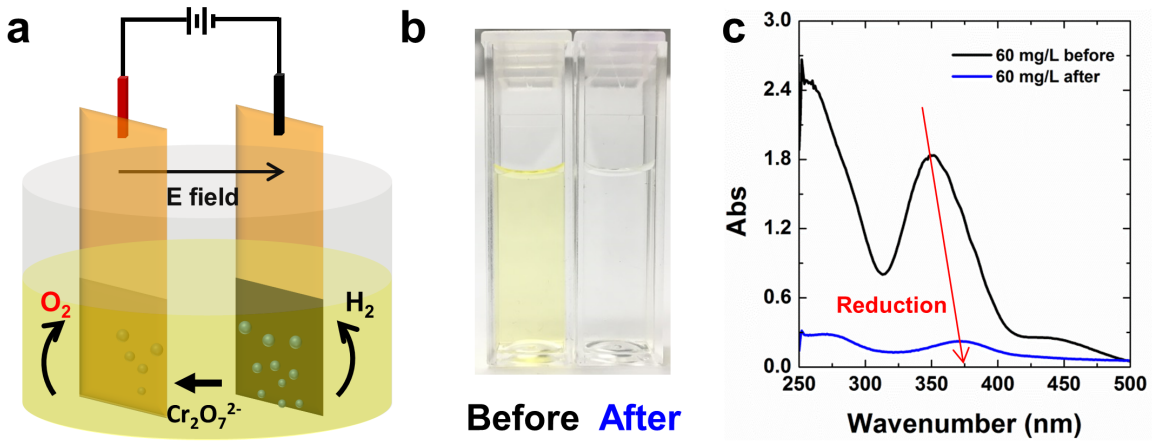

Figure 7.2. (a) Schematic illustration of the electrochemical Cr (VI) reduction set-up. (b) Photograph and (c) UV-vis spectra of 60 mg/L Cr (VI) solution before and after 15 V, 1 hr reduction.

To study the effects of concentration, applied voltage, and reduction time on the removal efficiency of Cr (VI), multiple control experiments were performed using the

same electrochemical reduction set-up and same compressed CNT foam electrodes. In Figure 7.3a and 7.3d, The high removal efficiency at lower Cr (VI) concentrations (20 and 40 mg/L) can be correlated to more efficient electrosorption initially and the following effective reduction electrochemically. As can be seen in Figure 7.3b and 7.3e, increasing applied voltage from 5 V to 10 V resulted into significant improvement (183% times higher) of Cr (VI) removal efficiency. When increased to 15 V, a slight improvement (4.3%) in removal efficiency was observed, which could possibly due to saturation in electrochemical reduction process. At same initial Cr (VI) concentration (60 mg/L) and applied voltage (15 V), Cr (VI) removal efficiency was observed to increase slightly with the increase amount of reduction time, and reached 95% after 2 hrs (see Figure 7.3c and 7.3f). There were two main competing reactions during the electrochemical reduction process, electrolysis and Cr (VI) reduction:

$$\text{Anode: } 2H_2O \rightarrow O_2 + 4\,H^+$$

$$\text{Cathode: } 4\,H^+ + 4\,e^- \rightarrow 2H_2$$

$$\text{Cr (VI)reduction: } Cr_2O_7^{2-} + 14\,H^+ + 6e^- \rightarrow 2Cr^{3+} + 7H_2O$$

It is obvious that Cr (VI) reduction is favorable at the anode side due to continuous generation of protons. While the high surface area nature of CNT foam electrodes promoted reactions at both anode and cathode sides.

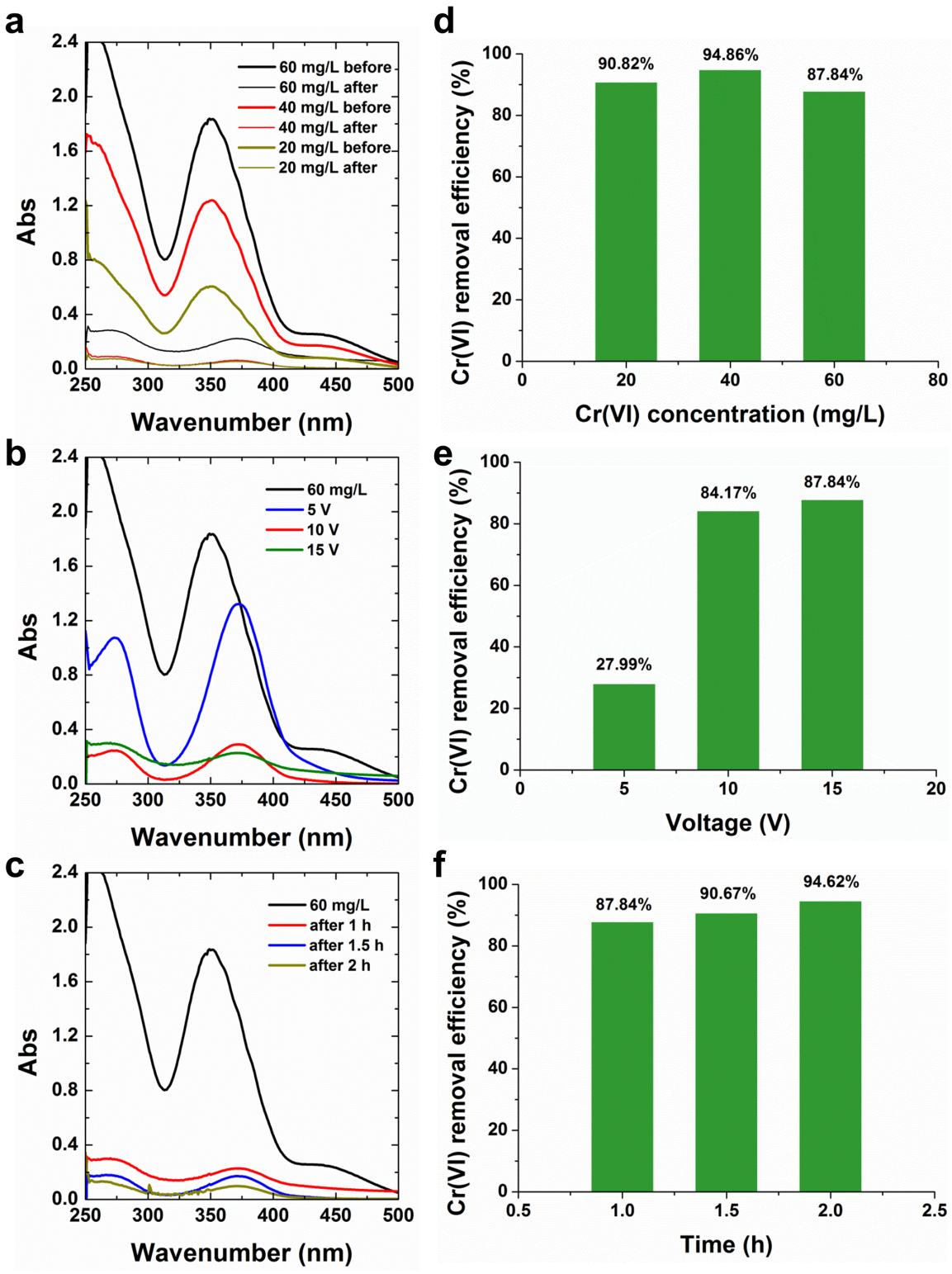

Figure 7.3. UV-vis spectra and bar plot comparison of Cr (VI) removal efficiency of (a) (d) 15 V, 1 hr reduction for 20, 40 and 60 mg/L Cr (VI) solutions before and after, (b) (e)

60 mg/L Cr (VI) solution reduced at 5, 10, 15 V for 1 hr before and after, and (c) (f) 60 mg/L Cr (VI) solution reduced at 15 V for 1, 1.5, 2 hrs before and after.

Besides pristine CNT foam, we also fabricated CNT-MoS2 composite foam to investigate the Cr (VI) removal capabilities. With an initial exfoliation of bulk MoS_2 in aqueous solution, the composite foam can be produced by similar vacuum freeze-drying method described in Figure 7.1 by simply mixing the MoS_2 exfoliation with CNT dispersion before freezing. SEM images and corresponding EDS elemental mapping results indicated uniform distribution of MoS_2 nanosheets within the CNT foam architecture, which ended up with ~5 wt% loading. For Cr (VI) removal experiment, CNT-MoS_2 composite foam was used for 60 mg/L Cr (VI) solution at different applied voltages (see Figure 7.4a). At 15 V, an increased removal efficiency of 90% comparing to 88% for pristine CNT foam was observed. Cyclic voltammetry was performed on these two different foam electrodes in 60 mg/L Cr (VI) solution between 0 to 16 V at a scan rate of 100 mV/s. As can be seen in Figure 7.4b, a peak around 10 V was observed for both foam electrodes, which could be correlated to Cr (VI) reduction to Cr (III).[342] A peak shift from ~11 V for CNT foam to ~9 V for CNT-MoS_2 composite foam dictated the role of MoS_2 nanosheets as efficient catalyst for oxygen evolution reaction that facilitates the reduction process and also lowers down the reduction energy.

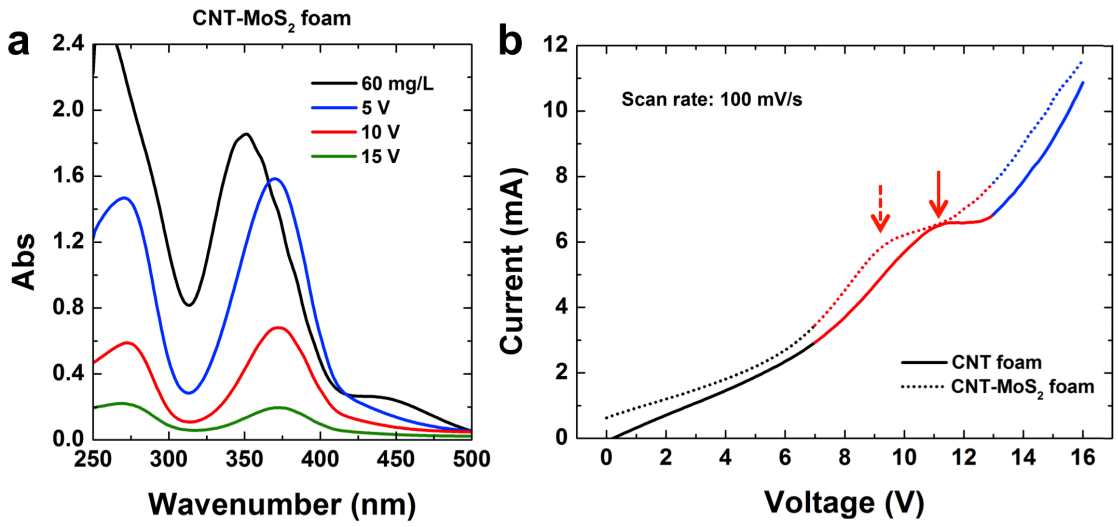

Figure 7.4. (a) UV-vis spectra of Cr (VI) removal by CNT-MoS_2 foam with initial Cr (VI) concentration of 60 mg/L for 1 hr electrochemical reduction at 5, 10, and 15 V. (b) Cyclic voltammogram of the electrochemical reduction of Cr (VI) by pristine CNT foam and CNT-MoS_2 foam between 0 to 16 V at 100 mV/s scan rate.

The total amount of energy input of the electrochemical reduction system in this work was calculated by using the applied voltage to multiply the integration of current profile. As plotted in Figure 7.5, this work required low energy-input and can still achieve high Cr (VI) removal efficiency around 90%, especially at high Cr (VI) concentration. The interconnected conductive CNT network that has high surface area stands out in comparison to other planar metal electrodes, which promotes the initial electrosorption of dichromate ions. MoS_2 nanosheets act as catalytic materials for the reduction of Cr (VI).

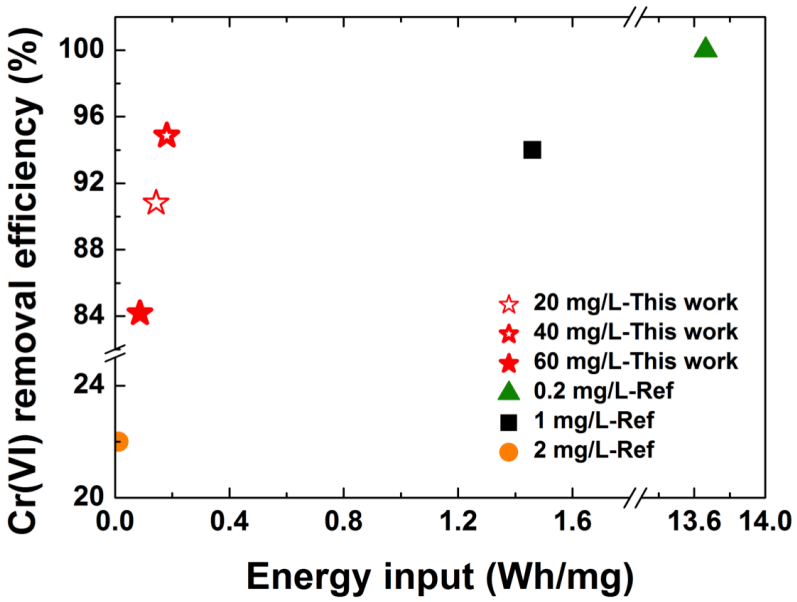

Figure 7.5. Cr (VI) removal efficiency and energy input in previously reported electrochemical Cr (VI) reduction work and this work.

7.4 Conclusion

In summary, we demonstrate an electrosorption and a following electrochemical reduction process for hexavalent chromium (Cr (VI)) removal by using compressed CNT-based foam as electrodes. With the conductive nature and high surface area, the CNT foam exhibit a high Cr (VI) removal efficiency of 88% at 15 V for 1 hr reduction time for 60 mg/L Cr (VI) aqueous solution. When incorporating MoS_2 nanosheets to fabricate composite CNT-MoS_2 foam, we observed an increase in Cr (VI) removal efficiency to 90% and corresponding low energy input of 0.16 Wh and high charge efficiency of 16%. The synergistic effect of CNT foam and MoS_2 nanosheets promotes the electrosorption of Cr (VI) and lowers down the Cr (VI) reduction energy, thus result into high Cr (VI) removal efficiency and charge efficiency at low energy input. The

manufacturing method of the macroscale foam architecture is promising for future pilot-scale applications in solving environmental problems.

CHAPTER 8

CONCLUSION AND LOOKING FORWARD

8.1 Conclusion

Here I demonstrated manufacturing of carbon nanocomposites based on different carbon nanomaterials for multiple energy storage systems including solid-state supercapacitors, sodium-ion battery anodes, red P-carbon composite for sodium-ion anodes, 2D black P-graphene heterostructured anodes for high capacity sodium-ion batteries, sulfur vapor-infiltrated CNT foam cathode for high areal performance Li-S batteries, and pristine and composite CNT foam electrodes for toxic Cr (VI) removal from water.

In each chapter, a different electrochemical system or environmental system was well-studied including the current status, previous achievement, possible improvements, and future directions. The role of carbon nanomaterials in all the above systems are well investigated with respect to different reaction mechanisms, motivations, and goals. In Chapter 2, I investigated the interaction between graphene and polymer electrolytes at the electrode-electrolyte interfaces for solid-state supercapacitors. I observed the tunable electrochemical window by varying the ratio of ionic liquid and polymer in the solid-state electrolyte. With further characterizations, my observation turned into deep understanding of pi-pi stacking at the interface, and further guided me on device fabrication to achieve both high energy and power performances.

Supercapacitors are advantageous in several applications, however, to pursue a high energy route, I moved to batteries. Starting my first battery making experience here

at Vanderbilt, it was exciting to see the giant foam in the quartz tube after using CVD processing with oxidized Ni, with further applications as sodium-ion battery anodes which exhibit stable cycling and high capacity compared to other carbon nanomaterials, as demonstrated in Chapter 3. To continue on this high energy-route, I introduced phosphorus (both red and black) to the lab due to their high theoretical capacity. However, even though there have been several publications on red P composite anodes, there is still a lacking of understanding of the role of carbon in the sodium-red P alloying process. Using the different kinds of carbon nanomaterials in the lab, I made different red P-carbon composite anodes, as described in Chapter 4. By analyzing electrochemical data carefully, I investigated the mechanism of reaction between carbon nanomaterials and different kinds of Na-P alloying products. Understanding of the new electrochemical system assisted by data analysis, I was able to guide the manufacturing of red P – carbon composite anodes to approach high theoretical sodium ion capacity (2596 mAh/g) while simultaneously addressing chemical interactions that compromise performance stability. Based on my understanding of the sodium-phosphorus system from the previous experience, I examined black phosphorus. (see Chapter 5) Inspired by EPD processes developed by a previous labmate, I decided to use the same technique for manufacturing 2D heterostructured electrodes for sodium-ion batteries to tackle the challenges in previous research in material handling and processing. I successfully fabricated ultrathin electrodes with good electrochemical properties, and the fabrication technique was further expanded to another co-contributed work on fabricating an ultrathin black P mechanical strain energy harvester. (see publication list). Besides the sodium system, lithium-sulfur batteries are also attractive to me due to the similar nature of high energy

materials just like phosphorus. As part of the team developing high sulfur loading techniques, I was thrilled to witness a vapor-phase capillary-driven process that can result in high amounts of sulfur loading in very short period of time. Combining this idea with my previous patent before I came to Vanderbilt, "Carbon nanotube sponge and method for making the same, US Patent US 9,102,537 B2", I came up with the idea of making 3D free-standing CNT foam to load sulfur to achieve high areal performance, as described in Chapter 6. The final result was gladly as expected, and thanks to this work I got the chance to participate in two professional research conferences. Finally, at the last stage of graduate school, I developed new applications of CNT foam to be used for heavy metal-hexavalent chromium (Cr (VI)) removal. Energy and the environment are topics that are always bonded to each other. For a sustainable future, not only preserving energy, but also protecting the environment are indispensable. With the UV-vis facility in Dr. Rizia Bardhan's lab (special thanks!), I was able to characterize the removal efficiency of Cr (VI) by electrochemical reduction. And as my last project, the excitement and enjoyable moments helped me become a more passionate and independent researcher. I was able to achieve a high removal efficiency of ~90% by using the CNT-MoS_2 composite foam as electrodes with a low energy input of 0.16 Wh and high charge efficiency of 16% comparing to pristine CNT foam.

8.2 Future of carbon nanocomposites for energy storage and environmental applications

With the continuous efforts in lowering the production costs of carbon nanomaterials, their applications for energy storage can be promising especially in flexible devices where high energy density is not usually required. Instead, outstanding mechanical properties and stable storage capabilities will be desirable.

Besides, building upon the research findings in this dissertation, with more systematic understandings of different electrochemical systems such as high energy or high power systems, where small quantities of carbon nanomaterials can play a vital role in improving device performance, more and more practical and larger-scale applications of composite electrode materials based on carbon nanomaterials will open a new era of carbon.

Again, with the development of the cost-effective production of carbon materials, they will offer exciting opportunities as adsorbent, membrane, or electrodes for efficient pollutant management such as wastewater treatment for heavy metal removal in which biodegradable nanocomposite design can be absolutely environmentally benign.

8.3 Outlook of future projects

With the expertise in carbon nanomaterials and skills in nanomanufacturing of carbon nanocomposites, a variety of promising future projects can be designed by combining current lab expertise in anode-free batteries, electrochemical carbon nanotube growth, desalination, and energy harvesting devices.

Based on the fabrication method of three-dimensional carbon nanotube foam structures, different 3D architectures with highly porous features and high surface area can be achieved. Some examples include: 1) Pre-treat the carbon nanomaterial precursor for desired wettability; 2) incorporate multiple nanomaterials to make nanocomposite foams for multifunctional applications; 3) post-treatment of three-dimensional carbon foam by annealing or polymer infiltration for strengthening the mechanical robustness for desired systems.

From the material cost point of view, with the currently developed electrochemical growth of carbon nanotubes from ambient carbon dioxide,[29-30, 32, 343-344] further fabrication of three-dimensional carbon nanotube foam structures can potentially be low-cost and more scalable.

From the application point of view, in the anode-free type of battery, high energy density is an ultimate goal.[345-347] To push the current status further, where two-dimensional carbon films are used as seed layers for metal plating,[347] a properly designed three-dimensional carbon foam architecture with good wettability and highly porous features can be introduced to achieve more uniform plating with projected higher energy density when compressing it into 2D film. Inspired from sulfur-vapor infiltration into carbon nanotube foams,[33-34, 151, 294, 348] further experiments can be developed to even expand the idea to metal infiltration such as lithium or sodium for fabricating high-performance metal anode battery with high energy density, high coulombic efficiency and improved safety.[347] Based on the electrochemically-driven mechanical strain energy harvesting systems,[299, 349-353] a flexible and compressible all-foam-based harvester can be implemented into shoes to harvest stepping energy. For environmental applications, composite foam architectures can be developed to improve heavy metal removal efficiency and improve the charge efficiency by incorporating catalytic nanomaterials or hydrophilic nanomaterials.

From the manufacturing point of view, except for electrophoretic deposition[71, 225-226, 300, 354-355] and vacuum freeze-drying of foam fabrication,[348] new approaches can be developed to improve the scalability and lower the cost of fabricating functional composite materials. For example, solution assembly that utilizes the differences in

surface charges of different materials for nanocomposite fabrication, roll-to-roll manufacturing of composite foam for structural applications, or flexible textile fabrication.

REFERENCES

1. Sengupta, R.; Bhattacharya, M.; Bandyopadhyay, S.; Bhowmick, A. K., A review on the mechanical and electrical properties of graphite and modified graphite reinforced polymer composites. *Prog. Polym. Sci.* **2011,** *36*, 638-670.
2. Allaoui, A.; Bai, S.; Cheng, H.-M.; Bai, J., Mechanical and electrical properties of a MWNT/epoxy composite. *Compos. Sci. Technol.* **2002,** *62*, 1993-1998.
3. Wang, M.; Wang, J.; Chen, Q.; Peng, L. M., Fabrication and electrical and mechanical properties of carbon nanotube interconnections. *Adv. Funct. Mater.* **2005,** *15*, 1825-1831.
4. Dai, H.; Wong, E. W.; Lieber, C. M., Probing electrical transport in nanomaterials: conductivity of individual carbon nanotubes. *Science* **1996,** *272*, 523-526.
5. Baimova, J. A.; Liu, B.; Dmitriev, S. V.; Zhou, K., Mechanical properties and structures of bulk nanomaterials based on carbon nanopolymorphs. *Phys. Status Solidi Rapid Res. Lett.* **2014,** *8*, 336-340.
6. Parveen, S.; Rana, S.; Fangueiro, R.; Paiva, M. C., Microstructure and mechanical properties of carbon nanotube reinforced cementitious composites developed using a novel dispersion technique. *Cem. Concr. Res.* **2015,** *73*, 215-227.
7. Hayashi, T.; Kim, Y. A.; Natsuki, T.; Endo, M., Mechanical properties of carbon nanomaterials. *Chemphyschem* **2007,** *8*, 999-1004.
8. Sun, H.; Ren, J.; Qu, X., Carbon nanomaterials and DNA: From molecular recognition to applications. *Accounts Chem. Res.* **2016,** *49*, 461-470.
9. Cha, C.; Shin, S. R.; Annabi, N.; Dokmeci, M. R.; Khademhosseini, A., Carbon-based nanomaterials: multifunctional materials for biomedical engineering. *ACS Nano* **2013,** *7*, 2891-2897.
10. Baptista, F. R.; Belhout, S.; Giordani, S.; Quinn, S., Recent developments in carbon nanomaterial sensors. *Chem. Soc. Rev.* **2015,** *44*, 4433-4453.
11. Knoch, J.; Appenzeller, J., Tunneling phenomena in carbon nanotube field-effect transistors. *Phys. Status Solidi A* **2008,** *205*, 679-694.
12. Franklin, A. D., Nanomaterials in transistors: From high-performance to thin-film applications. *Science* **2015,** *349*, aab2750.
13. Liu, S.; Guo, X., Carbon nanomaterials field-effect-transistor-based biosensors. *NPG Asia Mater.* **2012,** *4*, e23.
14. Guo, C. X.; Yang, H. B.; Sheng, Z. M.; Lu, Z. S.; Song, Q. L.; Li, C. M., Layered graphene/quantum dots for photovoltaic devices. *Angew. Chem. Int. Edit.* **2010,** *49*, 3014-3017.
15. Brennan, L. J.; Byrne, M. T.; Bari, M.; Gun'ko, Y. K., Carbon Nanomaterials for Dye-Sensitized Solar Cell Applications: A Bright Future. *Adv. Energy Mater.* **2011,** *1*, 472-485.

16. Ago, H.; Petritsch, K.; Shaffer, M. S.; Windle, A. H.; Friend, R. H., Composites of carbon nanotubes and conjugated polymers for photovoltaic devices. *Adv. Mater.* **1999,** *11*, 1281-1285.
17. Zhu, Z.; Garcia-Gancedo, L.; Flewitt, A. J.; Xie, H.; Moussy, F.; Milne, W. I., A critical review of glucose biosensors based on carbon nanomaterials: carbon nanotubes and graphene. *Sensors* **2012,** *12*, 5996-6022.
18. Llobet, E., Gas sensors using carbon nanomaterials: A review. *Sens. Actuators B Chem.* **2013,** *179*, 32-45.
19. Yang, W.; Ratinac, K. R.; Ringer, S. P.; Thordarson, P.; Gooding, J. J.; Braet, F., Carbon nanomaterials in biosensors: should you use nanotubes or graphene? *Angew. Chem. Int. Edit.* **2010,** *49*, 2114-2138.
20. Zhang, Q.; Huang, J. Q.; Zhao, M. Q.; Qian, W. Z.; Wei, F., Carbon nanotube mass production: principles and processes. *ChemSusChem* **2011,** *4*, 864-889.
21. Ajayan, P. M.; Tour, J. M., Materials science: nanotube composites. *Nature* **2007,** *447*, 1066.
22. Kim, M.; Park, Y.-B.; Okoli, O. I.; Zhang, C., Processing, characterization, and modeling of carbon nanotube-reinforced multiscale composites. *Compos. Sci. Technol.* **2009,** *69*, 335-342.
23. U.S. Energy Information Administration. International Energy Outlook. **2016**.
24. Frackowiak, E.; Beguin, F., Carbon materials for the electrochemical storage of energy in capacitors. *Carbon* **2001,** *39*, 937-950.
25. Wang, D. W.; Li, F.; Liu, M.; Lu, G. Q.; Cheng, H. M., 3D aperiodic hierarchical porous graphitic carbon material for high-rate electrochemical capacitive energy storage. *Angew. Chem. Int. Edit.* **2008,** *120*, 379-382.
26. Che, G.; Lakshmi, B. B.; Fisher, E. R.; Martin, C. R., Carbon nanotubule membranes for electrochemical energy storage and production. *Nature* **1998,** *393*, 346.
27. Frackowiak, E.; Beguin, F., Electrochemical storage of energy in carbon nanotubes and nanostructured carbons. *Carbon* **2002,** *40*, 1775-1787.
28. Raccichini, R.; Varzi, A.; Passerini, S.; Scrosati, B., The role of graphene for electrochemical energy storage. *Nat. Mater.* **2015,** *14*, 271.
29. Douglas, A.; Carter, R.; Muralidharan, N.; Oakes, L.; Pint, C. L., Iron catalyzed growth of crystalline multi-walled carbon nanotubes from ambient carbon dioxide mediated by molten carbonates. *Carbon* **2017,** *116*, 572-578.
30. Douglas, A.; Muralidharan, N.; Carter, R.; Pint, C. L., Sustainable Capture and Conversion of Carbon Dioxide into Valuable Multiwalled Carbon Nanotubes Using Metal Scrap Materials. *ACS Sus. Chem. Eng.* **2017,** *5*, 7104-7110.
31. Douglas, A.; Carter, R. E.; Li, M.; Pint, C. L., Toward Small Diameter Carbon Nanotubes Synthesized from Captured Carbon Dioxide: Critical Role of Catalyst Coarsening. *ACS Appl. Mater. Interfaces* **2018,** *10*, 19010-19018.

32. Licht, S.; Douglas, A.; Ren, J.; Carter, R.; Lefler, M.; Pint, C. L., Carbon nanotubes produced from ambient carbon dioxide for environmentally sustainable lithium-ion and sodium-ion battery anodes. *ACS Cent. Sci.* **2016,** *2*, 162-168.
33. Carter, R.; Oakes, L.; Muralidharan, N.; Cohn, A. P.; Douglas, A.; Pint, C. L., Polysulfide Anchoring Mechanism Revealed by Atomic Layer Deposition of V2O5 and Sulfur-Filled Carbon Nanotubes for Lithium-Sulfur Batteries. *ACS Appl. Mater. Interfaces* **2017,** *9*, 7185-7192.
34. Carter, R.; Davis, B.; Oakes, L.; Maschmann, M. R.; Pint, C. L., A high areal capacity lithium-sulfur battery cathode prepared by site-selective vapor infiltration of hierarchical carbon nanotube arrays. *Nanoscale* **2017,** *9*, 15018-15026.
35. Kumar, T. P.; Ramesh, R.; Lin, Y.; Fey, G. T.-K., Tin-filled carbon nanotubes as insertion anode materials for lithium-ion batteries. *Electrochem. Commun.* **2004,** *6*, 520-525.
36. Xu, Y.; Liu, Q.; Zhu, Y.; Liu, Y.; Langrock, A.; Zachariah, M. R.; Wang, C., Uniform nano-Sn/C composite anodes for lithium ion batteries. *Nano Lett.* **2013,** *13*, 470-474.
37. Xu, Y.; Zhu, Y.; Liu, Y.; Wang, C., Electrochemical performance of porous carbon/tin composite anodes for sodium-ion and lithium-ion batteries. *Adv. Energy Mater.* **2013,** *3*, 128-133.
38. Zhu, Y.; Wen, Y.; Fan, X.; Gao, T.; Han, F.; Luo, C.; Liou, S.-C.; Wang, C., Red phosphorus–single-walled carbon nanotube composite as a superior anode for sodium ion batteries. *ACS Nano* **2015,** *9*, 3254-3264.
39. Li, W.; Hu, S.; Luo, X.; Li, Z.; Sun, X.; Li, M.; Liu, F.; Yu, Y., Confined Amorphous Red Phosphorus in MOF-Derived N-Doped Microporous Carbon as a Superior Anode for Sodium-Ion Battery. *Adv. Mater.* **2017,** *29*, 1605820.
40. Sun, J.; Zheng, G.; Lee, H.-W.; Liu, N.; Wang, H.; Yao, H.; Yang, W.; Cui, Y., Formation of stable phosphorus–carbon bond for enhanced performance in black phosphorus nanoparticle–graphite composite battery anodes. *Nano Lett.* **2014,** *14*, 4573-4580.
41. Scrosati, B.; Garche, J., Lithium batteries: Status, prospects and future. *J. Power Sources* **2010,** *195*, 2419-2430.
42. Elliott, H.; Liberati, M.; Huang, C., Competitive Adsorption of Heavy Metals by Soils1. *J. Environ. Qual.* **1986,** *15*, 214-219.
43. Febrianto, J.; Kosasih, A. N.; Sunarso, J.; Ju, Y.-H.; Indraswati, N.; Ismadji, S., Equilibrium and kinetic studies in adsorption of heavy metals using biosorbent: a summary of recent studies. *J. Hazard. Mater.* **2009,** *162*, 616-645.
44. Saffaj, N.; Loukili, H.; Younssi, S. A.; Albizane, A.; Bouhria, M.; Persin, M.; Larbot, A., Filtration of solution containing heavy metals and dyes by means of ultrafiltration membranes deposited on support made of Moroccan clay. *Desalination* **2004,** *168*, 301-306.

45. Vigneswaran, S.; Ngo, H. H.; Chaudhary, D. S.; Hung, Y.-T., Physicochemical treatment processes for water reuse. In *Physicochemical treatment processes*, Springer: **2005**, pp 635-676.
46. Lytle, C. M.; Lytle, F. W.; Yang, N.; Qian, J.-H.; Hansen, D.; Zayed, A.; Terry, N., Reduction of Cr (VI) to Cr (III) by wetland plants: potential for in situ heavy metal detoxification. *Environ. Sci. Technol.* **1998,** *32*, 3087-3093.
47. Basta, N.; McGowen, S., Evaluation of chemical immobilization treatments for reducing heavy metal transport in a smelter-contaminated soil. *Environ. Pollut.* **2004,** *127*, 73-82.
48. Kobya, M.; Demirbas, E.; Senturk, E.; Ince, M., Adsorption of heavy metal ions from aqueous solutions by activated carbon prepared from apricot stone. *Bioresour. Technol.* **2005,** *96*, 1518-1521.
49. Congeevaram, S.; Dhanarani, S.; Park, J.; Dexilin, M.; Thamaraiselvi, K., Biosorption of chromium and nickel by heavy metal resistant fungal and bacterial isolates. *J. Hazard. Mater.* **2007,** *146*, 270-277.
50. Yan, G.; Viraraghavan, T., Heavy metal removal in a biosorption column by immobilized M. rouxii biomass. *Bioresour. Technol.* **2001,** *78*, 243-249.
51. Mier, M. V.; Callejas, R. L.; Gehr, R.; Cisneros, B. E. J.; Alvarez, P. J., Heavy metal removal with mexican clinoptilolite:: multi-component ionic exchange. *Water Res.* **2001,** *35*, 373-378.
52. Chevrier, V.; Ceder, G., Challenges for Na-ion negative electrodes. *J. Electrochem. Soc.* **2011,** *158*, A1011-A1014.
53. Wu, H.; Cui, Y., Designing nanostructured Si anodes for high energy lithium ion batteries. *Nano Today* **2012,** *7*, 414-429.
54. Guo, Y. G.; Hu, J. S.; Wan, L. J., Nanostructured materials for electrochemical energy conversion and storage devices. *Adv. Mater.* **2008,** *20*, 2878-2887.
55. Simon, P.; Gogotsi, Y., Materials for Electrochemical Capacitors. *Nat. Mater.* **2008,** *7*, 845-854.
56. Raccichini, R.; Varzi, A.; Passerini, S.; Scrosati, B., The Role of Graphene for Electrochemical Energy Storage. *Nat. Mater.* **2015,** *14*, 271-279.
57. Cheng, Y.; Lu, S.; Zhang, H.; Varanasi, C. V.; Liu, J., Synergistic Effects from Graphene and Carbon Nanotubes Enable Flexible and Robust Electrodes for High-performance Supercapacitors. *Nano Lett.* **2012,** *12*, 4206-4211.
58. Zhang, L. L.; Zhao, X., Carbon-Based Materials as Supercapacitor Electrodes. *Chem. Soc. Rev.* **2009,** *38*, 2520-2531.
59. Pan, H.; Li, J.; Feng, Y. P., Carbon Nanotubes for Supercapacitor. *Nanoscale Res. Lett.* **2010,** *5*, 654-668.
60. Liu, C. G.; Yu, Z. N.; Neff, D.; Zhamu, A.; Jang, B. Z., Graphene-Based Supercapacitor with an Ultrahigh Energy Density. *Nano Lett.* **2010,** *10*, 4863-4868.

61. Cheng, Q.; Tang, J.; Ma, J.; Zhang, H.; Shinya, N.; Qin, L. C., Graphene and Carbon Nanotube Composite Electrodes for Supercapacitors with Ultra-High Energy Density. *Phys. Chem. Chem. Phys.* **2011,** *13*, 17615-17624.
62. Zhu, Y. W.; Murali, S.; Stoller, M. D.; Ganesh, K. J.; Cai, W. W.; Ferreira, P. J.; Pirkle, A.; Wallace, R. M.; Cychosz, K. A.; Thommes, M.; Su, D.; Stach, E. A.; Ruoff, R. S., Carbon-Based Supercapacitors Produced by Activation of Graphene. *Science* **2011,** *332*, 1537-1541.
63. Lei, Z.; Liu, Z.; Wang, H.; Sun, X.; Lu, L.; Zhao, X., A High-Energy-Density Supercapacitor with Graphene–CMK-5 as the Electrode and Ionic Liquid as the Electrolyte. *J. Mater. Chem. A* **2013,** *1*, 2313-2321.
64. Kong, C.; Qian, W.; Zheng, C.; Yu, Y.; Cui, C.; Wei, F., Raising the Performance of a 4 V Supercapacitor Based on an EMIBF4–Single Walled Carbon Nanotube Nanofluid Electrolyte. *Chem. Commun.* **2013,** *49*, 10727-10729.
65. Yu, C.; Masarapu, C.; Rong, J.; Wei, B.; Jiang, H., Stretchable Supercapacitors Based on Buckled Single-Walled Carbon-Nanotube Macrofilms. *Adv. Mater.* **2009,** *11*, 4793.
66. Yamada, Y.; Kimizuka, O.; Tanaike, O.; Machida, K.; Suematsu, S.; Tamamitsu, K.; Saeki, S.; Yamada, Y.; Hatori, H., Capacitor Properties and Pore Structure of Single- and Double-Walled Carbon Nanotubes. *Electrochem. Solid-State Lett.* **2009,** *12*, K14-K16.
67. Jang, I. Y.; Muramatsu, H.; Park, K. C.; Kim, Y. J.; Endo, M., Capacitance Response of Double-Walled Carbon Nanotubes Depending on Surface Modification. *Electrochem. Commun.* **2009,** *11*, 719-723.
68. Zheng, C.; Qian, W.; Yu, Y.; Wei, F., Ionic Liquid Coated Single-Walled Carbon Nanotube Buckypaper as Supercapacitor Electrode. *Particuology* **2013,** *11*, 409-414.
69. Barisci, J. N.; Wallace, G. G.; Baughman, R. H., Electrochemical Characterization of Single-Walled Carbon Nanotube Electrodes. *J. Electrochem. Soc.* **2000,** *147*, 4580-4583.
70. Niu, Z.; Zhou, W.; Chen, J.; Feng, G.; Li, H.; Ma, W.; Li, J.; Dong, H.; Ren, Y.; Zhao, D., Compact-Designed Supercapacitors Using Free-Standing Single-Walled Carbon Nanotube Films. *Energy Environ. Sci.* **2011,** *4*, 1440-1446.
71. Carter, R.; Oakes, L.; Cohn, A. P.; Holzgrafe, J.; Zarick, H. F.; Chatterjee, S.; Bardhan, R.; Pint, C. L., Solution Assembled Single-Walled Carbon Nanotube Foams: Superior Performance in Supercapacitors, Lithium-Ion, and Lithium-Air Batteries. *J. Phys. Chem. C* **2014,** *118*, 20137-20151.
72. Kim, B.; Chung, H.; Kim, W., High-Performance Supercapacitors Based on Vertically Aligned Carbon Nanotubes and Nonaqueous Electrolytes. *Nanotechnology* **2012,** *23*, 155401.

73. Chen, Y.; Zhang, X.; Zhang, H.; Sun, X.; Zhang, D.; Ma, Y., High-Performance Supercapacitors Based on a Graphene–Activated Carbon Composite Prepared by Chemical Activation. *RSC Adv.* **2012,** *2*, 7747-7753.
74. Verma, P.; Maire, P.; Novak, P., A Review of the Features and Analyses of the Solid Electrolyte Interphase in Li-Ion Batteries. *Electrochim. Acta* **2010,** *55*, 6332-6341.
75. Agubra, V. A.; Fergus, J. W., The Formation and Stability of the Solid Electrolyte Interface on the Graphite Anode. *J. Power Sources* **2014,** *268*, 153-162.
76. Perez, E. M.; Martin, N., Pi-Pi Interactions in Carbon Nanostructures. *Chem. Soc. Rev.* **2015,** *44*, 6425-6433.
77. Carter, R.; Chatterjee, S.; Gordon, E.; Share, K.; Erwin, W. R.; Cohn, A. P.; Bardhan, R.; Pint, C. L., Corrosion Resistant Three-Dimensional Nanotextured Silicon for Water Photo-Oxidation. *Nanoscale* **2015,** *7*, 16755-16762.
78. Chatterjee, S.; Carter, R.; Oakes, L.; Erwin, W. R.; Bardhan, R.; Pint, C. L., Electrochemical and Corrosion Stability of Nanostructured Silicon by Graphene Coatings: Toward High Power Porous Silicon Supercapacitors. *J. Phys. Chem. C* **2014,** *118*, 10893-10902.
79. Cohn, A. P.; Erwin, W. R.; Share, K.; Oakes, L.; Westover, A. S.; Carter, R. E.; Bardhan, R.; Pint, C. L., All Silicon Electrode Photocapacitor for Integrated Energy Storage and Conversion. *Nano Lett.* **2015,** *15*, 2727-2731.
80. Oakes, L.; Westover, A.; Mares, J. W.; Chatterjee, S.; Erwin, W. R.; Bardhan, R.; Weiss, S. M.; Pint, C. L., Surface Engineered Porous Silicon for Stable, High Performance Electrochemical Supercapacitors. *Sci. Rep.* **2013,** *3*, 3020.
81. Westover, A. S.; Tian, J. W.; Bernath, S.; Oakes, L.; Edwards, R.; Shabab, F. N.; Chatterjee, S.; Anilkumar, A. V.; Pint, C. L., A Multifunctional Load-Bearing Solid-State Supercapacitor. *Nano Lett.* **2014,** *14*, 3197-3202.
82. Lin, Y. C.; Lu, C. C.; Yeh, C. H.; Jin, C. H.; Suenaga, K.; Chiu, P. W., Graphene Annealing: How Clean Can It Be? *Nano Lett.* **2012,** *12*, 414-419.
83. Westover, A. S.; Freudiger, D.; Gani, Z. S.; Share, K.; Oakes, L.; Carter, R. E.; Pint, C. L., On-Chip High Power Porous Silicon Lithium Ion Batteries with Stable Capacity Over 10,000 Cycles. *Nanoscale* **2015,** *7*, 98-103.
84. Gurunathan, K.; Murugan, A. V.; Marimuthu, R.; Mulik, U. P.; Amalnerkar, D. P., Electrochemically Synthesised Conducting Polymeric Materials for Applications Towards Technology in Electronics, Optoelectronics and Energy Storage Devices. *Mater. Chem. Phys.* **1999,** *61*, 173-191.
85. Sivaraman, P.; Rath, S. K.; Hande, V. R.; Thakur, A. P.; Patri, M.; Samui, A. B., All-Solid-Supercapacitor Based on Polyaniline and Sulfonated Polymers. *Synth. Met.* **2006,** *156*, 1057-1064.
86. Ferrari, A. C.; Robertson, J., Interpretation of Raman Spectra of Disordered and Amorphous Carbon. *Phys. Rev. B* **2000,** *61*, 14095-14107.

87. Li, S. W.; Guo, S. J.; Yang, H. L.; Gou, G. L.; Ren, R.; Li, J.; Dong, Z. P.; Jin, J.; Ma, J. T., Enhancing Catalytic Performance of Au Catalysts by Noncovalent Functionalized Graphene Using Functional Ionic Liquids. *J. Hazard. Mater.* **2014,** *270*, 11-17.
88. Zhang, Z. X.; Huang, H. L.; Yang, X. M.; Zang, L., Tailoring Electronic Properties of Graphene by Pi-Pi Stacking with Aromatic Molecules. *J. Phys. Chem. Lett.* **2011,** *2*, 2897-2905.
89. Sim, D.; Liu, D. Y.; Dong, X. C.; Xiao, N.; Li, S. A.; Zhao, Y.; Li, L. J.; Yan, Q. Y.; Hng, H. H., Power Factor Enhancement for Few-Layered Graphene Films by Molecular Attachments. *J. Phys. Chem. C* **2011,** *115*, 1780-1785.
90. Garcia, G.; Atilhan, M.; Aparicio, S., Adsorption of Choline Benzoate Ionic Liquid on Graphene, Silicene, Germanene and Boron-nitride Nanosheets: a DFT Perspective. *Phys. Chem. Chem. Phys.* **2015,** *17*, 16315-16326.
91. Kundu, D.; Talaie, E.; Duffort, V.; Nazar, L. F., The Emerging Chemistry of Sodium Ion Batteries for Electrochemical Energy Storage. *Angew. Chem. Int. Edit.* **2015,** *54*, 3431-3448.
92. Slater, M. D.; Kim, D.; Lee, E.; Johnson, C. S., Sodium-Ion Batteries. *Adv. Funct. Mater.* **2013,** *23*, 947-958.
93. Yabuuchi, N.; Kubota, K.; Dahbi, M.; Komaba, S., Research development on sodium-ion batteries. *Chem. Rev.* **2014,** *114*, 11636-11682.
94. Stevens, D.; Dahn, J., An In Situ Small-Angle X-Ray Scattering Study of Sodium Insertion into a Nanoporous Carbon Anode Material within an Operating Electrochemical Cell. *J. Electrochem. Soc.* **2000,** *147*, 4428-4431.
95. Stevens, D.; Dahn, J., The mechanisms of lithium and sodium insertion in carbon materials. *J. Electrochem. Soc.* **2001,** *148*, A803-A811.
96. Thomas, P.; Billaud, D., Sodium electrochemical insertion mechanisms in various carbon fibres. *Electrochim. Acta* **2001,** *46*, 3359-3366.
97. Thomas, P.; Billaud, D., Electrochemical insertion of sodium into hard carbons. *Electrochim. Acta* **2002,** *47*, 3303-3307.
98. Lotfabad, E. M.; Ding, J.; Cui, K.; Kohandehghan, A.; Kalisvaart, W. P.; Hazelton, M.; Mitlin, D., High-Density Sodium and Lithium Ion Battery Anodes from Banana Peels. *ACS Nano* **2014,** *8*, 7115-7129.
99. Ding, J.; Wang, H. L.; Li, Z.; Kohandehghan, A.; Cui, K.; Xu, Z. W.; Zahiri, B.; Tan, X. H.; Lotfabad, E. M.; Olsen, B. C.; Mitlin, D., Carbon Nanosheet Frameworks Derived from Peat Moss as High Performance Sodium Ion Battery Anodes. *ACS Nano* **2013,** *7*, 11004-11015.
100. Lotfabad, E. M.; Kalisvaart, P.; Kohandehghan, A.; Karpuzov, D.; Mitlin, D., Origin of non-SEI related coulombic efficiency loss in carbons tested against Na and Li. *J. Mater. Chem. A* **2014,** *2*, 19685-19695.

101. Bommier, C.; Surta, T. W.; Dolgos, M.; Ji, X., New Mechanistic Insights on Na-Ion Storage in Nongraphitizable Carbon. *Nano Lett.* **2015,** *15*, 5888-5892.
102. Jache, B.; Adelhelm, P., Use of Graphite as a Highly Reversible Electrode with Superior Cycle Life for Sodium-Ion Batteries by Making Use of Co-Intercalation Phenomena. *Angew. Chem. Int. Edit.* **2014,** *53*, 10169-10173.
103. Kim, H.; Hong, J.; Park, Y. U.; Kim, J.; Hwang, I.; Kang, K., Sodium Storage Behavior in Natural Graphite using Ether-based Electrolyte Systems. *Adv. Funct. Mater.* **2015,** *25*, 534-541.
104. Cohn, A. P.; Share, K.; Carter, R.; Oakes, L.; Pint, C. L., Ultrafast Solvent-Assisted Sodium Ion Intercalation into Highly Crystalline Few-Layered Graphene. *Nano Lett.* **2016,** *16*, 543-548.
105. Cao, Y.; Xiao, L.; Sushko, M. L.; Wang, W.; Schwenzer, B.; Xiao, J.; Nie, Z.; Saraf, L. V.; Yang, Z.; Liu, J., Sodium ion insertion in hollow carbon nanowires for battery applications. *Nano Lett.* **2012,** *12*, 3783-3787.
106. Alcántara, R.; Jiménez-Mateos, J. M.; Lavela, P.; Tirado, J. L., Carbon black: a promising electrode material for sodium-ion batteries. *Electrochem. Commun.* **2001,** *3*, 639-642.
107. Wen, Y.; He, K.; Zhu, Y.; Han, F.; Xu, Y.; Matsuda, I.; Ishii, Y.; Cumings, J.; Wang, C., Expanded graphite as superior anode for sodium-ion batteries. *Nat. Commun.* **2014,** *5*, 4033.
108. Wenzel, S.; Hara, T.; Janek, J.; Adelhelm, P., Room-temperature sodium-ion batteries: Improving the rate capability of carbon anode materials by templating strategies. *Energy Environ. Sci.* **2011,** *4*, 3342-3345.
109. Zhang, B.; Ghimbeu, C. M.; Laberty, C.; Vix-Guterl, C.; Tarascon, J. M., Correlation Between Microstructure and Na Storage Behavior in Hard Carbon. *Adv. Energy Mater.* **2016,** *6*, 1501588.
110. Wang, Z.; Qie, L.; Yuan, L.; Zhang, W.; Hu, X.; Huang, Y., Functionalized N-doped interconnected carbon nanofibers as an anode material for sodium-ion storage with excellent performance. *Carbon* **2013,** *55*, 328-334.
111. Wang, H. g.; Wu, Z.; Meng, F. l.; Ma, D. l.; Huang, X. l.; Wang, L. m.; Zhang, X. b., Nitrogen-Doped Porous Carbon Nanosheets as Low-Cost, High-Performance Anode Material for Sodium-Ion Batteries. *ChemSusChem* **2013,** *6*, 56-60.
112. Tang, K.; Fu, L.; White, R. J.; Yu, L.; Titirici, M. M.; Antonietti, M.; Maier, J., Hollow Carbon Nanospheres with Superior Rate Capability for Sodium-Based Batteries. *Adv. Energy Mater.* **2012,** *2*, 873-877.
113. Yun, Y. S.; Park, K. Y.; Lee, B.; Cho, S. Y.; Park, Y. U.; Hong, S. J.; Kim, B. H.; Gwon, H.; Kim, H.; Lee, S.; Park, Y. W.; Jin, H. J.; Kang, K., Sodium-Ion Storage in Pyroprotein-Based Carbon Nanoplates. *Adv. Mater.* **2015,** *27*, 6914.
114. Nessim, G. D., Properties, synthesis, and growth mechanisms of carbon nanotubes with special focus on thermal chemical vapor deposition. *Nanoscale* **2010,** *2*, 1306-1323.

115. Pint, C. L.; Nicholas, N. W.; Xu, S.; Sun, Z. Z.; Tour, J. M.; Schmidt, H. K.; Gordon, R. G.; Hauge, R. H., Three dimensional solid-state supercapacitors from aligned single-walled carbon nanotube array templates. *Carbon* **2011,** *49*, 4890-4897.
116. Ozden, S.; Tiwary, C. S.; Hart, A. H. C.; Chipara, A. C.; Romero-Aburto, R.; Rodrigues, M. T. F.; Taha-Tijerina, J.; Vajtai, R.; Ajayan, P. M., Density Variant Carbon Nanotube Interconnected Solids. *Adv. Mater.* **2015,** *27*, 1842.
117. Shawat, E.; Perelshtein, I.; Westover, A.; Pint, C. L.; Nessim, G. D., Ultra high-yield one-step synthesis of conductive and superhydrophobic three-dimensional mats of carbon nanofibers via full catalysis of unconstrained thin films. *J. Mater. Chem. A* **2014,** *2*, 15118-15123.
118. Hashim, D. P.; Narayanan, N. T.; Romo-Herrera, J. M.; Cullen, D. A.; Hahm, M. G.; Lezzi, P.; Suttle, J. R.; Kelkhoff, D.; Munoz-Sandoval, E.; Ganguli, S.; Roy, A. K.; Smith, D. J.; Vajtai, R.; Sumpter, B. G.; Meunier, V.; Terrones, H.; Terrones, M.; Ajayan, P. M., Covalently bonded three-dimensional carbon nanotube solids via boron induced nanojunctions. *Sci. Rep.* **2012,** *2*, 363.
119. Seghiouer, A.; Chevalet, J.; Barhoun, A.; Lantelme, F., Electrochemical oxidation of nickel in alkaline solutions: a voltammetric study and modelling. *J. Electroanal. Chem.* **1998,** *442*, 113-123.
120. Yang, L.; Qian, L.; Tian, X.; Li, J.; Dai, J.; Guo, Y.; Xiao, D., Hierarchically Porous Nickel Oxide Nanosheets Grown on Nickel Foam Prepared by One-Step In Situ Anodization for High-Performance Supercapacitors. *Chem. Asian. J.* **2014,** *9*, 1579-1585.
121. Pattinson, S. W.; Viswanath, B.; Zakharov, D. N.; Li, J. J.; Stach, E. A.; Hart, A. J., Mechanism and Enhanced Yield of Carbon Nanotube Growth on Stainless Steel by Oxygen-Induced Surface Reconstruction. *Chem. Mater.* **2015,** *27*, 932-937.
122. Hardwick, L. J.; Ruch, P. W.; Hahn, M.; Scheifele, W.; Kötz, R.; Novák, P., In situ Raman spectroscopy of insertion electrodes for lithium-ion batteries and supercapacitors: First cycle effects. *J. Phys. Chem. Solids* **2008,** *69*, 1232-1237.
123. Dimiev, A. M.; Ceriotti, G.; Behabtu, N.; Zakhidov, D.; Pasquali, M.; Saito, R.; Tour, J. M., Direct real-time monitoring of stage transitions in graphite intercalation compounds. *ACS Nano* **2013,** *7*, 2773-2780.
124. Ohzuku, T.; Iwakoshi, Y.; Sawai, K., Formation of Lithium-Graphite Intercalation Compounds in Nonaqueous Electrolytes and Their Application as a Negative Electrode for a Lithium Ion (Shuttlecock) Cell. *J. Electrochem. Soc.* **1993,** *140*, 2490-2498.
125. Liu, Y.; Merinov, B. V.; Goddard, W. A., Origin of low sodium capacity in graphite and generally weak substrate binding of Na and Mg among alkali and alkaline earth metals. *Proc. Natl. Acad. Sci. U S A* **2016,** *113*, 3735-3739.
126. Frank, O.; Tsoukleri, G.; Riaz, I.; Papagelis, K.; Parthenios, J.; Ferrari, A. C.; Geim, A. K.; Novoselov, K. S.; Galiotis, C., Development of a universal stress sensor for graphene and carbon fibres. *Nat. Commun.* **2011,** *2*, 255.

127. Ni, Z. H.; Yu, T.; Lu, Y. H.; Wang, Y. Y.; Feng, Y. P.; Shen, Z. X., Uniaxial strain on graphene: Raman spectroscopy study and band-gap opening. *ACS Nano* **2008,** *2*, 2301-2305.
128. Mukherjee, R.; Thomas, A. V.; Datta, D.; Singh, E.; Li, J.; Eksik, O.; Shenoy, V. B.; Koratkar, N., Defect-induced plating of lithium metal within porous graphene networks. *Nat. Commun.* **2014,** *5*, 1-10.
129. Ellis, B. L.; Nazar, L. F., Sodium and sodium-ion energy storage batteries. *Curr. Opin. Solid St. M.* **2012,** *16*, 168-177.
130. Palomares, V.; Serras, P.; Villaluenga, I.; Hueso, K. B.; Carretero-Gonzalez, J.; Rojo, T., Na-ion batteries, recent advances and present challenges to become low cost energy storage systems. *Energy Environ. Sci.* **2012,** *5*, 5884-5901.
131. Yabuuchi, N.; Matsuura, Y.; Ishikawa, T.; Kuze, S.; Son, J. Y.; Cui, Y. T.; Oji, H.; Komaba, S., Phosphorus Electrodes in Sodium Cells: Small Volume Expansion by Sodiation and the Surface-Stabilization Mechanism in Aprotic Solvent. *Chemelectrochem* **2014,** *1*, 580-589.
132. Li, W. J.; Chou, S. L.; Wang, J. Z.; Liu, H. K.; Dou, S. X., Simply Mixed Commercial Red Phosphorus and Carbon Nanotube Composite with Exceptionally Reversible Sodium-Ion Storage. *Nano Lett.* **2013,** *13*, 5480-5484.
133. Song, J.; Yu, Z.; Gordin, M. L.; Hu, S.; Yi, R.; Tang, D.; Walter, T.; Regula, M.; Choi, D.; Li, X., Chemically bonded phosphorus/graphene hybrid as a high performance anode for sodium-ion batteries. *Nano Lett.* **2014,** *14*, 6329-6335.
134. Li, W.; Yang, Z.; Li, M.; Jiang, Y.; Wei, X.; Zhong, X.; Gu, L.; Yu, Y., Amorphous Red Phosphorus Embedded in Highly Ordered Mesoporous Carbon with Superior Lithium and Sodium Storage Capacity. *Nano Lett.* **2016,** *16*, 1546-1553.
135. Xin, S.; Guo, Y. G.; Wan, L. J., Nanocarbon Networks for Advanced Rechargeable Lithium Batteries. *Accounts Chem. Res.* **2012,** *45*, 1759-1769.
136. Song, J. X.; Yu, Z. X.; Gordin, M. L.; Li, X. L.; Peng, H. S.; Wang, D. H., Advanced Sodium Ion Battery Anode Constructed via Chemical Bonding between Phosphorus, Carbon Nanotube, and Cross-Linked Polymer Binder. *ACS Nano* **2015,** *9*, 11933-11941.
137. Wu, N.; Yao, H. R.; Yin, Y. X.; Guo, Y. G., Improving the electrochemical properties of the red P anode in Na-ion batteries via the space confinement of carbon nanopores. *J. Mater. Chem. A* **2015,** *3*, 24221-24225.
138. Manthiram, A.; Chung, S. H.; Zu, C. X., Lithium-Sulfur Batteries: Progress and Prospects. *Adv. Mater.* **2015,** *27*, 1980-2006.
139. Seh, Z. W.; Sun, Y.; Zhang, Q.; Cui, Y., Designing high-energy lithium-sulfur batteries. *Chem. Soc. Rev.* **2016,** *45*, 5605-5634.
140. Bruce, P. G.; Freunberger, S. A.; Hardwick, L. J.; Tarascon, J. M., Li-O-2 and Li-S batteries with high energy storage. *Nat. Mater.* **2012,** *11*, 19-29.

141. Yin, Y. X.; Xin, S.; Guo, Y. G.; Wan, L. J., Lithium-Sulfur Batteries: Electrochemistry, Materials, and Prospects. *Angew. Chem. Int. Edit.* **2013,** *52*, 13186-13200.
142. Evers, S.; Nazar, L. F., New approaches for high energy density lithium-sulfur battery cathodes. *Acc. Chem. Res.* **2013,** *46*, 1135-43.
143. Manthiram, A.; Fu, Y.; Chung, S. H.; Zu, C.; Su, Y. S., Rechargeable lithium-sulfur batteries. *Chem. Rev.* **2014,** *114*, 11751-87.
144. Ma, L.; Hendrickson, K. E.; Wei, S. Y.; Archer, L. A., Nanomaterials: Science and applications in the lithium-sulfur battery. *Nano Today* **2015,** *10*, 315-338.
145. Yang, Y.; Zheng, G. Y.; Cui, Y., Nanostructured sulfur cathodes. *Chem. Soc. Rev.* **2013,** *42*, 3018-3032.
146. Carter, R.; Ejorh, D.; Share, K.; Cohn, A. P.; Douglas, A.; Muralidharan, N.; Tovar, T. M.; Pint, C. L., Surface Oxidized Mesoporous Carbons Derived from Porous Silicon as Dual Polysulfide Confinement and Anchoring Cathodes in Lithium Sulfur Batteries. *J. Power Sources* **2016,** *330*, 70-77.
147. Ding, Y. L.; Kopold, P.; Hahn, K.; van Aken, P. A.; Maier, J.; Yu, Y., Facile Solid-State Growth of 3D Well-Interconnected Nitrogen-Rich Carbon Nanotube-Graphene Hybrid Architectures for Lithium-Sulfur Batteries. *Adv. Funct. Mater.* **2016,** *26*, 1112-1119.
148. Gu, X. X.; Tong, C. J.; Lai, C.; Qiu, J. X.; Huang, X. X.; Yang, W. L.; Wen, B.; Liu, L. M.; Hou, Y. L.; Zhang, S. Q., A porous nitrogen and phosphorous dual doped graphene blocking layer for high performance Li-S batteries. *J. Mater. Chem. A* **2015,** *3*, 16670-16678.
149. Han, K.; Shen, J. M.; Hao, S. Q.; Ye, H. Q.; Wolverton, C.; Kung, M. C.; Kung, H. H., Free-Standing Nitrogen-doped Graphene Paper as Electrodes for High-Performance Lithium/Dissolved Polysulfide Batteries. *Chemsuschem* **2014,** *7*, 2545-2553.
150. Jand, S. P.; Chen, Y. X.; Kaghazchi, P., Comparative theoretical study of adsorption of lithium polysulfides (Li2Sx) on pristine and defective graphene. *J. Power Sources* **2016,** *308*, 166-171.
151. Oakes, L.; Carter, R.; Pint, C. L., Nanoscale defect engineering of lithium-sulfur battery composite cathodes for improved performance. *Nanoscale* **2016,** *8*, 19368-19375.
152. Brun, N.; Sakaushi, K.; Yu, L. H.; Giebeler, L.; Eckert, J.; Titirici, M. M., Hydrothermal carbon-based nanostructured hollow spheres as electrode materials for high-power lithium-sulfur batteries. *Phys. Chem. Chem. Phys.* **2013,** *15*, 6080-6087.
153. Li, Q.; Zhang, Z. A.; Zhang, K.; Fang, J.; Lai, Y. Q.; Li, J., A simple synthesis of hollow carbon nanofiber-sulfur composite via mixed-solvent process for lithium-sulfur batteries. *J. Power Sources* **2014,** *256*, 137-144.

154. Shin, E. S.; Kim, M. S.; Cho, W. I.; Oh, S. H., Sulfur/graphitic hollow carbon sphere nano-composite as a cathode material for high-power lithium-sulfur battery. *Nanoscale Res. Lett.* **2013,** *8*, 1-8.
155. Zhang, C. F.; Wu, H. B.; Yuan, C. Z.; Guo, Z. P.; Lou, X. W., Confining Sulfur in Double-Shelled Hollow Carbon Spheres for Lithium-Sulfur Batteries. *Angew. Chem. Int. Edit.* **2012,** *51*, 9592-9595.
156. Zheng, G. Y.; Yang, Y.; Cha, J. J.; Hong, S. S.; Cui, Y., Hollow Carbon Nanofiber-Encapsulated Sulfur Cathodes for High Specific Capacity Rechargeable Lithium Batteries. *Nano Lett.* **2011,** *11*, 4462-4467.
157. Share, K.; Westover, A.; Li, M.; Pint, C. L., Surface engineering of nanomaterials for improved energy storage–A review. *Chem. Eng. Sci.* **2016,** *154*, 3-19.
158. Malard, L. M.; Pimenta, M. A.; Dresselhaus, G.; Dresselhaus, M. S., Raman spectroscopy in graphene. *Phys. Rep.* **2009,** *473*, 51-87.
159. Ferrari, A. C.; Meyer, J. C.; Scardaci, V.; Casiraghi, C.; Lazzeri, M.; Mauri, F.; Piscanec, S.; Jiang, D.; Novoselov, K. S.; Roth, S.; Geim, A. K., Raman spectrum of graphene and graphene layers. *Phys. Rev. Lett.* **2006,** *97*, 187401-187404.
160. Iijima, S.; Yudasaka, M.; Yamada, R.; Bandow, S.; Suenaga, K.; Kokai, F.; Takahashi, K., Nano-aggregates of single-walled graphitic carbon nano-horns. *Chem. Phys. Lett.* **1999,** *309*, 165-170.
161. Wang, Y.; Alsmeyer, D. C.; Mccreery, R. L., Raman-Spectroscopy of Carbon Materials - Structural Basis of Observed Spectra. *Chem. Mater.* **1990,** *2*, 557-563.
162. Fujimori, T.; Urita, K.; Aoki, Y.; Kanoh, H.; Ohba, T.; Yudasaka, M.; Iijima, S.; Kaneko, K., Fine nanostructure analysis of single-wall carbon nanohorns by surface-enhanced Raman scattering. *J. Phys. Chem. C* **2008,** *112*, 7552-7556.
163. Zhu, S. Y.; Xu, G. B., Single-walled carbon nanohorns and their applications. *Nanoscale* **2010,** *2*, 2538-2549.
164. Mayo, M.; Griffith, K. J.; Pickard, C. J.; Morris, A. J., Ab Initio Study of Phosphorus Anodes for Lithium- and Sodium-Ion Batteries. *Chem. Mater.* **2016,** *28*, 2011-2021.
165. Zhang, Y.; Wang, H. W.; Luo, Z. Z.; Tan, H. T.; Li, B.; Sun, S. N.; Li, Z.; Zong, Y.; Xu, Z. C. J.; Yang, Y. H.; Khor, K. A.; Yan, Q. Y., An Air-Stable Densely Packed Phosphorene-Graphene Composite Toward Advanced Lithium Storage Properties. *Adv. Energy Mater.* **2016,** *6*, 1600453.
166. Datta, D.; Li, J. W.; Shenoy, V. B., Defective Graphene as a High-Capacity Anode Material for Na- and Ca-Ion Batteries. *ACS Appl. Mater. Interfaces* **2014,** *6*, 1788-1795.
167. Bommier, C.; Surta, T. W.; Dolgos, M.; Ji, X., New Mechanistic Insights on Na-Ion Storage in Nongraphitizable Carbon. *Nano Lett.* **2015,** *15*, 5888-92.
168. Popov, I. A.; Bozhenko, K. V.; Boldyrev, A. I., Is graphene aromatic? *Nano Res.* **2012,** *5*, 117-123.

169. Yu, X. F.; Giorgi, G.; Ushiyama, H.; Yamashita, K., First-principles study of fast Na diffusion in Na3P. *Chem. Phys. Lett.* **2014,** *612*, 129-133.
170. Yabuuchi, N.; Matsuura, Y.; Ishikawa, T.; Kuze, S.; Son, J. Y.; Cui, Y. T.; Oji, H.; Komaba, S., Phosphorus Electrodes in Sodium Cells: Small Volume Expansion by Sodiation and the Surface-Stabilization Mechanism in Aprotic Solvent. *Chemelectrochem* **2014,** *1*, 580-589.
171. Balogun, M. S.; Luo, Y.; Qiu, W. T.; Liu, P.; Tong, Y. X., A review of carbon materials and their composites with alloy metals for sodium ion battery anodes. *Carbon* **2016,** *98*, 162-178.
172. Wang, L. P.; Yu, L. H.; Wang, X.; Srinivasan, M.; Xu, Z. C. J., Recent developments in electrode materials for sodium-ion batteries. *J. Mater. Chem. A* **2015,** *3*, 9353-9378.
173. Xia, Q. B.; Li, W. J.; Miao, Z. C.; Chou, S. L.; Liu, H. K., Phosphorus and Phosphide Nanomaterials for Sodium-Ion Batteries. *Nano Res.* **2017,** *10*, 4055-4081.
174. Bridgman, P., TWO NEW MODIFICATIONS OF PHOSPHORUS. *J. Am. Chem. Soc.* **1914,** *36*, 1344-1363.
175. Krebs, H.; Weitz, H.; Worms, K., On the structure and properties of the semimetals. VIII. the catalytic representation of the black phosphorus. *Z. Anorg. Allg. Chem* **1955,** *280*, 119-33.
176. Lange, S.; Schmidt, P.; Nilges, T., Au3SnP7@black phosphorus: An easy access to black phosphorus. *Inorg. Chem.* **2007,** *46*, 4028-4035.
177. Eswaraiah, V.; Zeng, Q. S.; Long, Y.; Liu, Z., Black Phosphorus Nanosheets: Synthesis, Characterization and Applications. *Small* **2016,** *12*, 3480-3502.
178. Jiang, Q. Q.; Xu, L.; Chen, N.; Zhang, H.; Dai, L. M.; Wang, S. Y., Facile Synthesis of Black Phosphorus: an Efficient Electrocatalyst for the Oxygen Evolving Reaction. *Angew. Chem. Int. Edit.* **2016,** *55*, 13849-13853.
179. Larcher, D.; Tarascon, J. M., Towards greener and more sustainable batteries for electrical energy storage. *Nat. Chem.* **2015,** *7*, 19-29.
180. Tian, B.; Tian, B.; Smith, B.; Scott, M.; Lei, Q.; Hua, R.; Tian, Y.; Liu, Y., Facile bottom-up synthesis of partially oxidized black phosphorus nanosheets as metal-free photocatalyst for hydrogen evolution. *Proc. Natl. Acad. Sci. U S A* **2018**, 201800069.
181. Xia, F.; Wang, H.; Jia, Y., Rediscovering black phosphorus as an anisotropic layered material for optoelectronics and electronics. *Nat. Commun.* **2014,** *5*, 4458.
182. Avsar, A.; Vera-Marun, I. J.; Tan, J. Y.; Watanabe, K.; Taniguchi, T.; Neto, A. H. C.; Ozyilmaz, B., Air-Stable Transport in Graphene-Contacted, Fully Encapsulated Ultrathin Black Phosphorus-Based Field-Effect Transistors. *ACS Nano* **2015,** *9*, 4138-4145.
183. Liu, H.; Du, Y. C.; Deng, Y. X.; Ye, P. D., Semiconducting black phosphorus: synthesis, transport properties and electronic applications. *Chem. Soc. Rev.* **2015,** *44*, 2732-2743.

184. Liu, H. W.; Zou, Y. Q.; Tao, L.; Ma, Z. L.; Liu, D. D.; Zhou, P.; Liu, H. B.; Wang, S. Y., Sandwiched Thin-Film Anode of Chemically Bonded Black Phosphorus/Graphene Hybrid for Lithium-Ion Battery. *Small* **2017,** *13*, 1700758.
185. Wang, L. X.; Jiang, Z. Q.; Li, W.; Gu, X.; Huang, L., Hybrid phosphorene/graphene nanocomposite as an anode material for Na-ion batteries: a first-principles study. *J. Phys. D Appl. Phys.* **2017,** *50*, 165501.
186. Kulish, V. V.; Malyi, O. I.; Persson, C.; Wu, P., Phosphorene as an anode material for Na-ion batteries: a first-principles study. *Phys. Chem. Chem. Phys.* **2015,** *17*, 13921-13928.
187. Zhang, Y.; Sun, W. P.; Luo, Z. Z.; Zheng, Y.; Yu, Z. W.; Zhang, D.; Yang, J.; Tan, H. T.; Zhu, J. X.; Wang, X. L.; Yan, Q. Y.; Dou, S. X., Functionalized few-layer black phosphorus with super-wettability towards enhanced reaction kinetics for rechargeable batteries. *Nano Energy* **2017,** *40*, 576-586.
188. Sun, J.; Lee, H. W.; Pasta, M.; Yuan, H. T.; Zheng, G. Y.; Sun, Y. M.; Li, Y. Z.; Cui, Y., A Phosphorene-Graphene Hybrid Material as a High-Capacity Anode for Sodium-Ion Batteries. *Nat. Nanotechnol.* **2015,** *10*, 980-985.
189. Chen, T. W.; Zhao, P.; Guo, X.; Zhang, S. L., Two-Fold Anisotropy Governs Morphological Evolution and Stress Generation in Sodiated Black Phosphorus for Sodium Ion Batteries. *Nano Lett.* **2017,** *17*, 2299-2306.
190. Liu, H. W.; Tao, L.; Zhang, Y. Q.; Xie, C.; Zhou, P.; Liu, H. B.; Chen, R.; Wang, S. Y., Bridging Covalently Functionalized Black Phosphorus on Graphene for High-Performance Sodium-Ion Battery. *ACS Appl. Mater. Interfaces* **2017,** *9*, 36849-36856.
191. Chen, Y.; Jiang, G. B.; Chen, S. Q.; Guo, Z. N.; Yu, X. F.; Zhao, C. J.; Zhang, H.; Bao, Q. L.; Wen, S. C.; Tang, D. Y.; Fan, D. Y., Mechanically Exfoliated Black Phosphorus as a New Saturable Absorber for Both Q-switching and Mode-locking Laser Operation. *Opt. Express* **2015,** *23*, 12823-12833.
192. Castellanos-Gomez, A.; Vicarelli, L.; Prada, E.; Island, J. O.; Narasimha-Acharya, K. L.; Blanter, S. I.; Groenendijk, D. J.; Buscema, M.; Steele, G. A.; Alvarez, J. V.; Zandbergen, H. W.; Palacios, J. J.; van der Zant, H. S. J., Isolation and Characterization of Few-Layer Black Phosphorus. *2D Mater.* **2014,** *1*, 025001.
193. Island, J. O.; Steele, G. A.; van der Zant, H. S. J.; Castellanos-Gomez, A., Environmental Instability of Few-Layer Black Phosphorus. *2D Mater.* **2015,** *2*, 011002.
194. Brent, J. R.; Savjani, N.; Lewis, E. A.; Haigh, S. J.; Lewis, D. J.; O'Brien, P., Production of Few-Layer Phosphorene by Liquid Exfoliation of Black Phosphorus. *Chem. Commun.* **2014,** *50*, 13338-13341.
195. Hanlon, D.; Backes, C.; Doherty, E.; Cucinotta, C. S.; Berner, N. C.; Boland, C.; Lee, K.; Harvey, A.; Lynch, P.; Gholamvand, Z.; Zhang, S. F.; Wang, K. P.; Moynihan, G.; Pokle, A.; Ramasse, Q. M.; McEvoy, N.; Blau, W. J.; Wang, J.; Abellan, G.; Hauke, F.; Hirsch, A.; Sanvito, S.; O'Regan, D. D.; Duesberg, G. S.; Nicolosi, V.; Coleman, J.

N., Liquid exfoliation of solvent-stabilized few-layer black phosphorus for applications beyond electronics. *Nat. Commun.* **2015,** *6*, 8563.
196. Kang, J.; Wood, J. D.; Wells, S. A.; Lee, J. H.; Liu, X. L.; Chen, K. S.; Hersam, M. C., Solvent Exfoliation of Electronic-Grade, Two-Dimensional Black Phosphorus. *ACS Nano* **2015,** *9*, 3596-3604.
197. Ramireddy, T.; Xing, T.; Rahman, M. M.; Chen, Y.; Dutercq, Q.; Gunzelmann, D.; Glushenkov, A. M., Phosphorus-Carbon Nanocomposite Anodes for Lithium-Ion and Sodium-Ion Batteries. *J. Mater. Chem. A* **2015,** *3*, 5572-5584.
198. Hembrarn, K. P. S. S.; Jung, H.; Yeo, B. C.; Pai, S. J.; Kim, S.; Lee, K. R.; Han, S. S., Unraveling the Atomistic Sodiation Mechanism of Black Phosphorus for Sodium Ion Batteries by First-Principles Calculations. *J. Phys. Chem. C* **2015,** *119*, 15041-15046.
199. Xu, G. L.; Chen, Z. H.; Zhong, G. M.; Liu, Y. Z.; Yang, Y.; Ma, T. Y.; Ren, Y.; Zuo, X. B.; Wu, X. H.; Zhang, X. Y.; Amine, K., Nanostructured Black Phosphorus/Ketjenblack Multiwalled Carbon Nanotubes Composite as High Performance Anode Material for Sodium-Ion Batteries. *Nano Lett.* **2016,** *16*, 3955-3965.
200. Cohn, A. P.; Share, K.; Carter, R.; Oakes, L.; Pint, C. L., Ultrafast solvent-assisted sodium ion intercalation into highly crystalline few-layered graphene. *Nano Lett.* **2015,** *16*, 543-548.
201. Xie, X. Q.; Ao, Z. M.; Su, D. W.; Zhang, J. Q.; Wang, G. X., MoS2/Graphene Composite Anodes with Enhanced Performance for Sodium-Ion Batteries: The Role of the Two-Dimensional Heterointerface. *Adv. Funct. Mater.* **2015,** *25*, 1393-1403.
202. Pomerantseva, E.; Gogotsi, Y., Two-Dimensional Heterostructures for Energy Storage. *Nat. Energy* **2017,** *2*, 17089.
203. Oakes, L.; Carter, R.; Hanken, T.; Cohn, A. P.; Share, K.; Schmidt, B.; Pint, C. L., Interface strain in vertically stacked two-dimensional heterostructured carbon-MoS2 nanosheets controls electrochemical reactivity. *Nat. Commun.* **2016,** *7*, 11796.
204. Zou, X. M.; Huang, C. W.; Wang, L. F.; Yin, L. J.; Li, W. Q.; Wang, J. L.; Wu, B.; Liu, Y. Q.; Yao, Q.; Jiang, C. Z.; Wu, W. W.; He, L.; Chen, S. S.; Ho, J. C.; Liao, L., Dielectric Engineering of a Boron Nitride/Hafnium Oxide Heterostructure for High-Performance 2D Field Effect Transistors. *Adv. Mater.* **2016,** *28*, 2062-2069.
205. Nouri, M. B.; Moradi, M., Presentation and Investigation of a New Two Dimensional Heterostructure Phononic Crystal to Obtain Extended Band Gap. *Physica B.* **2016,** *489*, 28-32.
206. Xia, F. N.; Wang, H.; Xiao, D.; Dubey, M.; Ramasubramaniam, A., Two-Dimensional Material Nanophotonics. *Nat. Photonics* **2014,** *8*, 899-907.
207. Sun, Z. P.; Martinez, A.; Wang, F., Optical Modulators With 2D Layered Materials. *Nat. Photonics* **2016,** *10*, 227-238.
208. Avouris, P., Graphene: Electronic and Photonic Properties and Devices. *Nano Lett.* **2010,** *10*, 4285-4294.

209. Frank, I. W.; Tanenbaum, D. M.; Van der Zande, A. M.; McEuen, P. L., Mechanical Properties of Suspended Graphene Sheets. *J. Vac. Sci. Technol. B* **2007,** *25*, 2558-2561.
210. Paton, K. R.; Varrla, E.; Backes, C.; Smith, R. J.; Khan, U.; O'Neill, A.; Boland, C.; Lotya, M.; Istrate, O. M.; King, P.; Higgins, T.; Barwich, S.; May, P.; Puczkarski, P.; Ahmed, I.; Moebius, M.; Pettersson, H.; Long, E.; Coelho, J.; O'Brien, S. E.; McGuire, E. K.; Sanchez, B. M.; Duesberg, G. S.; McEvoy, N.; Pennycook, T. J.; Downing, C.; Crossley, A.; Nicolosi, V.; Coleman, J. N., Scalable production of large quantities of defect-free few-layer graphene by shear exfoliation in liquids. *Nat. Mater.* **2014,** *13*, 624-630.
211. Hernandez, Y.; Nicolosi, V.; Lotya, M.; Blighe, F. M.; Sun, Z. Y.; De, S.; McGovern, I. T.; Holland, B.; Byrne, M.; Gun'ko, Y. K.; Boland, J. J.; Niraj, P.; Duesberg, G.; Krishnamurthy, S.; Goodhue, R.; Hutchison, J.; Scardaci, V.; Ferrari, A. C.; Coleman, J. N., High-yield production of graphene by liquid-phase exfoliation of graphite. *Nat. Nanotechnol.* **2008,** *3*, 563-568.
212. Choucair, M.; Thordarson, P.; Stride, J. A., Gram-scale production of graphene based on solvothermal synthesis and sonication. *Nat. Nanotechnol.* **2009,** *4*, 30-33.
213. Ginés, L.; Mandal, S.; Cheng, C.-L.; Sow, M.; Williams, O. A., Positive Zeta Potential of Nanodiamonds. *Nanoscale* **2017,** *9*, 12549-12555.
214. Guo, Z.; Zhang, H.; Lu, S.; Wang, Z.; Tang, S.; Shao, J.; Sun, Z.; Xie, H.; Wang, H.; Yu, X. F., From black phosphorus to phosphorene: basic solvent exfoliation, evolution of Raman scattering, and applications to ultrafast photonics. *Adv. Funct. Mater.* **2015,** *25*, 6996-7002.
215. Yang, M. Q.; Xu, Y. J.; Lu, W. H.; Zeng, K. Y.; Zhu, H.; Xu, Q. H.; Ho, G. W., Self-Surface Charge Exfoliation and Electrostatically Coordinated 2D Hetero-Layered Hybrids. *Nat. Commun.* **2017,** *8*, 14224.
216. Fang, Y. X.; Guo, S. J.; Zhu, C. Z.; Zhai, Y. M.; Wang, E. K., Self-Assembly of Cationic Polyelectrolyte-Functionalized Graphene Nanosheets and Gold Nanoparticles: A Two-Dimensional Heterostructure for Hydrogen Peroxide Sensing. *Langmuir* **2010,** *26*, 11277-11282.
217. Yang, S. B.; Feng, X. L.; Ivanovici, S.; Mullen, K., Fabrication of Graphene-Encapsulated Oxide Nanoparticles: Towards High-Performance Anode Materials for Lithium Storage. *Angew. Chem. Int. Edit.* **2010,** *49*, 8408-8411.
218. Park, H.; Noh, S. H.; Lee, J. H.; Lee, W. J.; Jaung, J. Y.; Lee, S. G.; Han, T. H., Large Scale Synthesis and Light Emitting Fibers of Tailor-Made Graphene Quantum Dots. *Sci. Rep.* **2015,** *5*, 14163.
219. Wilson, N. R.; Pandey, P. A.; Beanland, R.; Young, R. J.; Kinloch, I. A.; Gong, L.; Liu, Z.; Suenaga, K.; Rourke, J. P.; York, S. J.; Sloan, J., Graphene Oxide: Structural Analysis and Application as a Highly Transparent Support for Electron Microscopy. *ACS Nano* **2009,** *3*, 2547-2556.

220. Flores, E.; Ares, J. R.; Castellanos-Gomez, A.; Barawi, M.; Ferrer, I. J.; Sanchez, C., Thermoelectric Power of Bulk Black-Phosphorus. *Appl Phys Lett* **2015,** *106*, 022102.
221. Wu, Z. S.; Ren, W. C.; Gao, L. B.; Liu, B. L.; Jiang, C. B.; Cheng, H. M., Synthesis of High-Quality Graphene with a Pre-Determined Number of Layers. *Carbon* **2009,** *47*, 493-499.
222. Liu, H. T.; Zhang, L.; Guo, Y. L.; Cheng, C.; Yang, L. J.; Jiang, L.; Yu, G.; Hu, W. P.; Liu, Y. Q.; Zhu, D. B., Reduction of Graphene Oxide to Highly Conductive Graphene by Lawesson's Reagent and its Electrical Applications. *J. Mater. Chem. C* **2013,** *1*, 3104-3109.
223. Kim, F.; Cote, L. J.; Huang, J. X., Graphene Oxide: Surface Activity and Two-Dimensional Assembly. *Adv. Mater.* **2010,** *22*, 1954-1958.
224. Gunjakar, J. L.; Kim, I. Y.; Lee, J. M.; Lee, N. S.; Hwang, S. J., Self-assembly of layered double hydroxide 2D nanoplates with graphene nanosheets: an effective way to improve the photocatalytic activity of 2D nanostructured materials for visible light-induced O-2 generation. *Energy Environ. Sci.* **2013,** *6*, 1008-1017.
225. Oakes, L.; Westover, A.; Mahjouri-Samani, M.; Chatterjee, S.; Puretzky, A. A.; Rouleau, C.; Geohegan, D. B.; Pint, C. L., Uniform, Homogenous Coatings of Carbon Nanohorns on Arbitrary Substrates from Common Solvents. *ACS Appl. Mater. Interfaces* **2013,** *5*, 13153-13160.
226. Oakes, L.; Zulkifli, D.; Azmi, H.; Share, K.; Hanken, T.; Carter, R.; Pint, C. L., One Batch Exfoliation and Assembly of Two-Dimensional Transition Metal Dichalcogenide Nanosheets Using Electrophoretic Deposition. *J. Electrochem. Soc.* **2015,** *162*, D3063-D3070.
227. Sarkar, P.; Nicholson, P. S., Electrophoretic Deposition (EPD): Mechanisms, Kinetics, and Application to Ceramics. *J. Am. Ceram. Soc.* **1996,** *79*, 1987-2002.
228. Wu, N.; She, X.; Yang, D.; Wu, X.; Su, F.; Chen, Y., Synthesis of Network Reduced Graphene Oxide in Polystyrene Matrix by a Two-Step Reduction Method for Superior Conductivity of the Composite. *J. Mater. Chem.* **2012,** *22*, 17254-17261.
229. Fan, Z.; Wang, K.; Wei, T.; Yan, J.; Song, L.; Shao, B., An Environmentally Friendly and Efficient Route for the Reduction of Graphene Oxide by Aluminum Powder. *Carbon* **2010,** *48*, 1686-1689.
230. Pawbake, A. S.; Erande, M. B.; Jadkar, S. R.; Late, D. J., Temperature Dependent Raman Spectroscopy of Electrochemically Exfoliated Few Layer Black Phosphorus Nanosheets. *RSC Adv.* **2016,** *6*, 76551-76555.
231. Shen, Z.; Sun, S.; Wang, W.; Liu, J.; Liu, Z.; Jimmy, C. Y., A Black–Red Phosphorus Heterostructure for Efficient Visible-Light-Driven Photocatalysis. *J. Mater. Chem. A* **2015,** *3*, 3285-3288.
232. Sugai, S.; Shirotani, I., Raman and infrared reflection spectroscopy in black phosphorus. *Solid state communications* **1985,** *53*, 753-755.

233. Appalakondaiah, S.; Vaitheeswaran, G.; Lebegue, S.; Christensen, N. E.; Svane, A., Effect of van der Waals interactions on the structural and elastic properties of black phosphorus. *Phys. Rev. B* **2012,** *86*, 035105.
234. Favron, A.; Gaufrès, E.; Fossard, F.; Tang, N. Y.; Lévesque, P. L.; Loiseau, A.; Leonelli, R.; Francoeur, S.; Martel, R., Photooxidation and Quantum Confinement Effects in Exfoliated Black Phosphorus. *Nat. Mater.* **2015,** *14*, 826-833.
235. Hernandez, Y.; Nicolosi, V.; Lotya, M.; Blighe, F. M.; Sun, Z.; De, S.; McGovern, I.; Holland, B.; Byrne, M.; Gun'Ko, Y. K., High-yield production of graphene by liquid-phase exfoliation of graphite. *Nat. Nanotechnol.* **2008,** *3*, 563-568.
236. Kim, Y.; Park, Y.; Choi, A.; Choi, N. S.; Kim, J.; Lee, J.; Ryu, J. H.; Oh, S. M.; Lee, K. T., An amorphous red phosphorus/carbon composite as a promising anode material for sodium ion batteries. *Adv. Mater.* **2013,** *25*, 3045-3049.
237. Dahbi, M.; Yabuuchi, N.; Fukunishi, M.; Kubota, K.; Chihara, K.; Tokiwa, K.; Yu, X.-f.; Ushiyama, H.; Yamashita, K.; Son, J.-Y., Black phosphorus as a high-capacity, high-capability negative electrode for sodium-ion batteries: investigation of the electrode/electrolyte interface. *Chem. Mater.* **2016,** *28*, 1625-1635.
238. David, L.; Singh, G., Reduced Graphene Oxide Paper Electrode: Opposing Effect of Thermal Annealing on Li and Na Cyclability. *J. Phys. Chem. C* **2014,** *118*, 28401-28408.
239. David, L.; Bhandavat, R.; Singh, G., MoS2/Graphene Composite Paper for Sodium-Ion Battery Electrodes. *ACS Nano* **2014,** *8*, 1759-1770.
240. Wu, Y. T.; Nie, P.; Wu, L. Y.; Dou, H.; Zhang, X. G., 2D MXene/SnS2 composites as high-performance anodes for sodium ion batteries. *Chem. Eng. J.* **2018,** *334*, 932-938.
241. Zhang, Y. D.; Zhu, P. Y.; Huang, L. L.; Xie, J.; Zhang, S. C.; Cao, G. S.; Zhao, X. B., Few-Layered SnS2 on Few-Layered Reduced Graphene Oxide as Na-Ion Battery Anode with Ultralong Cycle Life and Superior Rate Capability. *Adv. Funct. Mater.* **2015,** *25*, 481-489.
242. Xie, X.; Kretschmer, K.; Anasori, B.; Sun, B.; Wang, G.; Gogotsi, Y., Porous Ti3C2T x MXene for Ultrahigh-Rate Sodium-Ion Storage with Long Cycle Life. *ACS Appl. Nano Mater.* **2018,** *1*, 505-511.
243. Tan, C.; Zhang, H., Two-dimensional transition metal dichalcogenide nanosheet-based composites. *Chem. Soc. Rev.* **2015,** *44*, 2713-2731.
244. Bruce, P. G.; Scrosati, B.; Tarascon, J. M., Nanomaterials for Rechargeable Lithium Batteries. *Angew. Chem. Int. Edit.* **2008,** *47*, 2930-2946.
245. Ji, X. L.; Lee, K. T.; Nazar, L. F., A Highly Ordered Nanostructured Carbon-Sulphur Cathode for Lithium-Sulphur Batteries. *Nat. Mater.* **2009,** *8*, 500-506.
246. Manthiram, A.; Fu, Y. Z.; Su, Y. S., Challenges and Prospects of Lithium-Sulfur Batteries. *Accounts Chem. Res.* **2013,** *46*, 1125-1134.

247. Manthiram, A.; Fu, Y. Z.; Chung, S. H.; Zu, C. X.; Su, Y. S., Rechargeable Lithium-Sulfur Batteries. *Chem. Rev.* **2014,** *114*, 11751-11787.
248. Yang, Y.; McDowell, M. T.; Jackson, A.; Cha, J. J.; Hong, S. S.; Cui, Y., New Nanostructured Li2S/Silicon Rechargeable Battery with High Specific Energy. *Nano Lett.* **2010,** *10*, 1486-1491.
249. Choi, N. S.; Chen, Z. H.; Freunberger, S. A.; Ji, X. L.; Sun, Y. K.; Amine, K.; Yushin, G.; Nazar, L. F.; Cho, J.; Bruce, P. G., Challenges Facing Lithium Batteries and Electrical Double-Layer Capacitors. *Angew. Chem. Int. Edit.* **2012,** *51*, 9994-10024.
250. Liang, Z.; Zheng, G. Y.; Li, W. Y.; Seh, Z. W.; Yao, H. B.; Yan, K.; Kong, D. S.; Cui, Y., Sulfur Cathodes with Hydrogen Reduced Titanium Dioxide Inverse Opal Structure. *ACS Nano* **2014,** *8*, 5249-5256.
251. Yang, Y.; Yu, G. H.; Cha, J. J.; Wu, H.; Vosgueritchian, M.; Yao, Y.; Bao, Z. A.; Cui, Y., Improving the Performance of Lithium-Sulfur Batteries by Conductive Polymer Coating. *ACS Nano* **2011,** *5*, 9187-9193.
252. Ji, L. W.; Rao, M. M.; Aloni, S.; Wang, L.; Cairns, E. J.; Zhang, Y. G., Porous Carbon Nanofiber-Sulfur Composite Electrodes for Lithium/Sulfur Cells. *Energy Environ. Sci.* **2011,** *4*, 5053-5059.
253. Jayaprakash, N.; Shen, J.; Moganty, S. S.; Corona, A.; Archer, L. A., Porous Hollow Carbon@Sulfur Composites for High-Power Lithium-Sulfur Batteries. *Angew. Chem. Int. Edit.* **2011,** *50*, 5904-5908.
254. Fu, Y. Z.; Su, Y. S.; Manthiram, A., Highly Reversible Lithium/Dissolved Polysulfide Batteries with Carbon Nanotube Electrodes. *Angew. Chem. Int. Edit.* **2013,** *52*, 6930-6935.
255. Song, J. X.; Xu, T.; Gordin, M. L.; Zhu, P. Y.; Lv, D. P.; Jiang, Y. B.; Chen, Y. S.; Duan, Y. H.; Wang, D. H., Nitrogen- Doped Mesoporous Carbon Promoted Chemical Adsorption of Sulfur and Fabrication of High- Areal- Capacity Sulfur Cathode with Exceptional Cycling Stability for Lithium- Sulfur Batteries. *Adv. Funct. Mater.* **2014,** *24*, 1243-1250.
256. Park, J.; Moon, J.; Kim, C.; Kang, J. H.; Lim, E.; Park, J.; Lee, K. J.; Yu, S.-H.; Seo, J.-H.; Lee, J., Graphene Quantum Dots: Structural Integrity and Oxygen Functional Groups for High Sulfur/Sulfide Utilization in Lithium Sulfur Batteries. *NPG Asia Mater.* **2016,** *8*, e272.
257. Liang, C. D.; Dudney, N. J.; Howe, J. Y., Hierarchically Structured Sulfur/Carbon Nanocomposite Material for High-Energy Lithium Battery. *Chem. Mater.* **2009,** *21*, 4724-4730.
258. Zhang, B.; Qin, X.; Li, G. R.; Gao, X. P., Enhancement of Long Stability of Sulfur Cathode by Encapsulating Sulfur into Micropores of Carbon Spheres. *Energy Environ. Sci.* **2010,** *3*, 1531-1537.

259. Li, Z.; Huang, Y. M.; Yuan, L. X.; Hao, Z. X.; Huang, Y. H., Status and Prospects in Sulfur-Carbon Composites as Cathode Materials for Rechargeable Lithium-Sulfur Batteries. *Carbon* **2015,** *92*, 41-63.
260. Chen, Y.; Lu, S. T.; Wu, X. H.; Liu, J., Flexible Carbon Nanotube-Graphene/Sulfur Composite Film: Free-Standing Cathode for High-Performance Lithium/Sulfur Batteries. *J. Phys. Chem. C* **2015,** *119*, 10288-10294.
261. Chen, Y.; Lu, S. T.; Zhou, J.; Wu, X. H.; Qin, W.; Ogoke, O.; Wu, G., 3D Graphene Framework Supported Li2S Coated with Ultra-Thin Al2O3 Films: Binder-Free Cathodes for High-Performance Lithium Sulfur Batteries. *J. Mater. Chem. A* **2017,** *5*, 102-112.
262. Wang, D. W.; Zhou, G. M.; Li, F.; Wu, K. H.; Lu, G. Q.; Cheng, H. M.; Gentle, I. R., A Microporous-Mesoporous Carbon with Graphitic Structure for a High-Rate Stable Sulfur Cathode in Carbonate Solvent-Based Li-S Batteries. *Phys. Chem. Chem. Phys.* **2012,** *14*, 8703-8710.
263. Sun, L.; Li, M. Y.; Jiang, Y.; Kong, W. B.; Jiang, K. L.; Wang, J. P.; Fan, S. S., Sulfur Nanocrystals Confined in Carbon Nanotube Network As a Binder-Free Electrode for High-Performance Lithium Sulfur Batteries. *Nano Lett.* **2014,** *14*, 4044-4049.
264. Zhou, G. M.; Pei, S. F.; Li, L.; Wang, D. W.; Wang, S. G.; Huang, K.; Yin, L. C.; Li, F.; Cheng, H. M., A Graphene-Pure-Sulfur Sandwich Structure for Ultrafast, Long-Life Lithium-Sulfur Batteries. *Adv. Mater.* **2014,** *26*, 625-631.
265. Sun, L.; Kong, W. B.; Li, M. Y.; Wu, H. C.; Jiang, K. L.; Li, Q. Q.; Zhang, Y. H.; Wang, J. P.; Fan, S. S., Cross-Stacked Carbon Nanotube Film as an Additional Built-in Current Collector and Adsorption Layer for High-Performance Lithium Sulfur Batteries. *Nanotechnology* **2016,** *27*, 075401.
266. Evers, S.; Nazar, L. F., Graphene-Enveloped Sulfur in a One Pot Reaction: A Cathode with Good Coulombic Efficiency and High Practical Sulfur Content. *Chem. Commun.* **2012,** *48*, 1233-1235.
267. Tao, X.; Wang, J.; Ying, Z.; Cai, Q.; Zheng, G.; Gan, Y.; Huang, H.; Xia, Y.; Liang, C.; Zhang, W.; Cui, Y., Strong Sulfur Binding with Conducting Magneli-Phase Ti(n)O2(n-1) Nanomaterials for Improving Lithium-Sulfur Batteries. *Nano Lett.* **2014,** *14*, 5288-5294.
268. Liang, X.; Hart, C.; Pang, Q.; Garsuch, A.; Weiss, T.; Nazar, L. F., A Highly Efficient Polysulfide Mediator for Lithium-Sulfur Batteries. *Nat. Commun.* **2015,** *6*, 5682.
269. Song, J. X.; Gordin, M. L.; Xu, T.; Chen, S. R.; Yu, Z. X.; Sohn, H.; Lu, J.; Ren, Y.; Duan, Y. H.; Wang, D. H., Strong Lithium Polysulfide Chemisorption on Electroactive Sites of Nitrogen-Doped Carbon Composites For High-Performance Lithium-Sulfur Battery Cathodes. *Angew. Chem. Int. Edit.* **2015,** *54*, 4325-4329.

270. Su, Y. S.; Manthiram, A., A New Approach to Improve Cycle Performance of Rechargeable Lithium-Sulfur Batteries by Inserting a Free-Standing MWCNT Interlayer. *Chem. Commun.* **2012,** *48*, 8817-8819.
271. Su, Y. S.; Manthiram, A., Lithium-Sulphur Batteries with a Microporous Carbon Paper as a Bifunctional Interlayer. *Nat. Commun.* **2012,** *3*, 1166.
272. Wang, X. F.; Wang, Z. X.; Chen, L. Q., Reduced Graphene Oxide Film as a Shuttle-Inhibiting Interlayer in a Lithium-Sulfur Battery. *J. Power Sources* **2013,** *242*, 65-69.
273. Bruce, P. G.; Freunberger, S. A.; Hardwick, L. J.; Tarascon, J. M., Li-O2 and Li-S Batteries with High Energy Storage. *Nat. Mater.* **2011,** *11*, 19-29.
274. Yang, Y.; Zheng, G. Y.; Cui, Y., Nanostructured sulfur cathodes. *Chem. Soc. Rev.* **2013,** *42*, 3018-3032.
275. Whittingham, M. S., Electrical Energy-Storage and Intercalation Chemistry. *Science* **1976,** *192*, 1126-1127.
276. Dahn, J. R.; Zheng, T.; Liu, Y. H.; Xue, J. S., Mechanisms for Lithium Insertion in Carbonaceous Materials. *Science* **1995,** *270*, 590-593.
277. Goodenough, J. B.; Park, K. S., The Li-Ion Rechargeable Battery: A Perspective. *J. Am. Chem. Soc.* **2013,** *135*, 1167-1176.
278. Xu, T.; Song, J. X.; Gordin, M. L.; Sohn, H.; Yu, Z. X.; Chen, S. R.; Wang, D. H., Mesoporous Carbon-Carbon Nanotube-Sulfur Composite Microspheres for High-Areal-Capacity Lithium-Sulfur Battery Cathodes. *ACS Appl. Mater. Interfaces* **2013,** *5*, 11355-11362.
279. Lv, D. P.; Zheng, J. M.; Li, Q. Y.; Xie, X.; Ferrara, S.; Nie, Z. M.; Mehdi, L. B.; Browning, N. D.; Zhang, J. G.; Graff, G. L.; Liu, J.; Xiao, J., High Energy Density Lithium-Sulfur Batteries: Challenges of Thick Sulfur Cathodes. *Adv. Energy Mater.* **2015,** *5*, 1402290.
280. Fang, R. P.; Zhao, S. Y.; Hou, P. X.; Cheng, M.; Wang, S. G.; Cheng, H. M.; Liu, C.; Li, F., 3D Interconnected Electrode Materials with Ultrahigh Areal Sulfur Loading for Li-S Batteries. *Adv. Mater.* **2016,** *28*, 3374-3382.
281. Ye, X. M.; Ma, J.; Hu, Y. S.; Wei, H. Y.; Ye, F. F., MWCNT Porous Microspheres with an Efficient 3D Conductive Network for High Performance Lithium-Sulfur Batteries. *J. Mater. Chem. A* **2016,** *4*, 775-780.
282. Lu, S. T.; Chen, Y.; Wu, X. H.; Wang, Z. D.; Li, Y., Three-Dimensional Sulfur/Graphene Multifunctional Hybrid Sponges for Lithium-Sulfur Batteries with Large Areal Mass Loading. *Sci. Rep.* **2014,** *4*, 4629.
283. Singhal, R.; Chung, S. H.; Manthiram, A.; Kalra, V., A Free-Standing Carbon Nanofiber Interlayer for High-Performance Lithium-Sulfur Batteries. *J. Mater. Chem. A* **2015,** *3*, 4530-4538.
284. Shaibani, M.; Akbari, A.; Sheath, P.; Easton, C. D.; Banerjee, P. C.; Konstas, K.; Fakhfouri, A.; Barghamadi, M.; Musameh, M. M.; Best, A. S.; Ruther, T.; Mahon, P. J.;

Hill, M. R.; Hollenkamp, A. F.; Majumder, M., Suppressed Polysulfide Crossover in Li-S Batteries through a High-Flux Graphene Oxide Membrane Supported on a Sulfur Cathode. *ACS Nano* **2016,** *10*, 7768-7779.
285. Chung, S. H.; Chang, C. H.; Manthiram, A., A Carbon-Cotton Cathode with Ultrahigh-Loading Capability for Statically and Dynamically Stable Lithium-Sulfur Batteries. *ACS Nano* **2016,** *10*, 10462-10470.
286. Qie, L.; Zu, C. X.; Manthiram, A., A High Energy Lithium-Sulfur Battery with Ultrahigh-Loading Lithium Polysulfide Cathode and its Failure Mechanism. *Adv. Energy Mater.* **2016,** *6*, 1502459.
287. Qie, L.; Manthiram, A., Uniform Li2S Precipitation on N,O-Codoped Porous Hollow Carbon Fibers for High-Energy-Density Lithium-Sulfur Batteries with Superior Stability. *Chem. Commun.* **2016,** *52*, 10964-10967.
288. Sun, H. Y.; Xu, Z.; Gao, C., Multifunctional, Ultra-Flyweight, Synergistically Assembled Carbon Aerogels. *Adv. Mater.* **2013,** *25*, 2554-2560.
289. Dong, L. B.; Yang, Q.; Xu, C. J.; Li, Y.; Yang, D. M.; Hou, F.; Yin, H. F.; Kang, F. Y., Facile Preparation of Carbon Nanotube Aerogels with Controlled Hierarchical Microstructures and Versatile Performance. *Carbon* **2015,** *90*, 164-171.
290. Bryning, M. B.; Milkie, D. E.; Islam, M. F.; Hough, L. A.; Kikkawa, J. M.; Yodh, A. G., Carbon Nanotube Aerogels. *Adv. Mater.* **2007,** *19*, 661-664.
291. Luo, S.; Luo, Y.; Wu, H.; Li, M.; Yan, L.; Jiang, K.; Liu, L.; Li, Q.; Fan, S.; Wang, J., Self-assembly of 3D Carbon Nanotube Sponges: A Simple and Controllable Way to Build Macroscopic and Ultralight Porous Architectures. *Adv. Mater.* **2016,** *29*, 1603549.
292. Gui, X.; Wei, J.; Wang, K.; Cao, A.; Zhu, H.; Jia, Y.; Shu, Q.; Wu, D., Carbon Nanotube Sponges. *Adv. Mater.* **2010,** *22*, 617-621.
293. Carter, R.; Oakes, L.; Muralidharan, N.; Cohn, A. P.; Douglas, A.; Pint, C. L., Polysulfide Anchoring Mechanism Revealed by Atomic Layer Deposition of V2O5 and Sulfur-Filled Carbon Nanotubes for Lithium-Sulfur Batteries. *ACS Appl. Mater. Interfaces* **2017,** *9*, 7185-7192.
294. Carter, R. E.; Oakes, L.; Muralidharan, N.; Pint, C. L., Isothermal Sulfur Condensation into Carbon Scaffolds: Improved Loading, Performance, and Scalability for Lithium Sulfur Battery Cathodes. *J. Phys. Chem. C* **2017**, DOI: 10.1021/acs.jpcc.7b01117.
295. Hagen, M.; Hanselmann, D.; Ahlbrecht, K.; Maca, R.; Gerber, D.; Tubke, J., Lithium-Sulfur Cells: The Gap between the State-of-the-Art and the Requirements for High Energy Battery Cells. *Adv. Energy. Mater.* **2015,** *5*.
296. Hagen, M.; Hanselmann, D.; Ahlbrecht, K.; Maca, R.; Gerber, D.; Tubke, J., Lithium-Sulfur Cells: The Gap between the State-of-the-Art and the Requirements for High Energy Battery Cells. *Adv. Energy Mater.* **2015,** *5*, 1401986.

297. Oakes, L.; Hanken, T.; Carter, R.; Yates, W.; Pint, C. L., Roll-to-Roll Nanomanufacturing of Hybrid Nanostructures for Energy Storage Device Design. *ACS Appl. Mater. Interfaces* **2015,** *7*, 14201-14210.
298. Li, M.; Carter, R.; Oakes, L.; Douglas, A.; Muralidharan, N.; Pint, C. L., Role of carbon defects in the reversible alloying states of red phosphorus composite anodes for efficient sodium ion batteries. *J. Mater. Chem. A* **2017,** *5*, 5266-5272.
299. Muralidharan, N.; Li, M. Y.; Carter, R. E.; Galioto, N.; Pint, C. L., Ultralow Frequency Electrochemical-Mechanical Strain Energy Harvester Using 2D Black Phosphorus Nanosheets. *ACS Energy Lett.* **2017,** *2*, 1797-1803.
300. Li, M.; Muralidharan, N.; Moyer, K.; Pint, C., Solvent Mediated Hybrid 2D Materials: Black Phosphorus-Graphene Heterostructured Building Blocks Assembled for Sodium Ion Batteries. *Nanoscale* **2018,** *10*, 10443-10449.
301. Luo, S.; Yu, Y.; Li, M. Y.; Wu, H. C.; Zhao, F.; Jiang, K. L.; Wang, J. P.; Kang, F. Y.; Fan, S. S., Synergistic effect of manganese oxide nanoparticles and graphene nanosheets in composite anodes for lithium ion batteries. *Mater. Res. Express.* **2015,** *2*, 015503.
302. De Volder, M. F.; Tawfick, S. H.; Baughman, R. H.; Hart, A. J., Carbon nanotubes: present and future commercial applications. *science* **2013,** *339*, 535-539.
303. Zhu, H.; Xu, C.; Wu, D.; Wei, B.; Vajtai, R.; Ajayan, P., Direct synthesis of long single-walled carbon nanotube strands. *Science* **2002,** *296*, 884-886.
304. Jiang, H.; Lee, P. S.; Li, C., 3D carbon based nanostructures for advanced supercapacitors. *Energy Environ. Sci.* **2013,** *6*, 41-53.
305. Joo, S. H.; Choi, S. J.; Oh, I.; Kwak, J.; Liu, Z.; Terasaki, O.; Ryoo, R., Ordered nanoporous arrays of carbon supporting high dispersions of platinum nanoparticles. *Nature* **2001,** *412*, 169.
306. Acar, F.; Malkoc, E., The removal of chromium (VI) from aqueous solutions by Fagus orientalis L. *Bioresour. Technol.* **2004,** *94*, 13-15.
307. Eastmond, D. A.; MacGregor, J. T.; Slesinski, R. S., Trivalent chromium: assessing the genotoxic risk of an essential trace element and widely used human and animal nutritional supplement. *Crit. Rev. Toxicol.* **2008,** *38*, 173-190.
308. Gu, H.; Rapole, S. B.; Sharma, J.; Huang, Y.; Cao, D.; Colorado, H. A.; Luo, Z.; Haldolaarachchige, N.; Young, D. P.; Walters, B., Magnetic polyaniline nanocomposites toward toxic hexavalent chromium removal. *RSC Adv.* **2012,** *2*, 11007-11018.
309. Stern, A. H.; Bagdon, R. E.; Hazen, R. E.; Marzulli, F. N., Risk assessment of the allergic dermatitis potential of environmental exposure to hexavalent chromium. *J. Toxicol. Environ. Health A* **1993,** *40*, 613-641.
310. Saha, R.; Nandi, R.; Saha, B., Sources and toxicity of hexavalent chromium. *J. Coord. Chem.* **2011,** *64*, 1782-1806.
311. Zhang, X.-H.; Zhang, X.; Wang, X.-C.; Jin, L.-F.; Yang, Z.-P.; Jiang, C.-X.; Chen, Q.; Ren, X.-B.; Cao, J.-Z.; Wang, Q., Chronic occupational exposure to hexavalent

chromium causes DNA damage in electroplating workers. *BMC Public Health* **2011,** *11*, 224.
312. Gibb, H. J.; Lees, P. S.; Pinsky, P. F.; Rooney, B. C., Lung cancer among workers in chromium chemical production. *Am. J. Ind. Med.* **2000,** *38*, 115-126.
313. Tang, W.-W.; Zeng, G.-M.; Gong, J.-L.; Liang, J.; Xu, P.; Zhang, C.; Huang, B.-B., Impact of humic/fulvic acid on the removal of heavy metals from aqueous solutions using nanomaterials: a review. *Sci. Total Environ.* **2014,** *468*, 1014-1027.
314. Gupta, V. K.; Saleh, T. A., Sorption of pollutants by porous carbon, carbon nanotubes and fullerene-An overview. *Environ. Sci. Pollut. Res.* **2013,** *20*, 2828-2843.
315. Mauter, M. S.; Elimelech, M., Environmental applications of carbon-based nanomaterials. *Environ. Sci. Technol.* **2008,** *42*, 5843-5859.
316. Mubarak, N.; Sahu, J.; Abdullah, E.; Jayakumar, N., Removal of heavy metals from wastewater using carbon nanotubes. *Sep. Purif. Rev.* **2014,** *43*, 311-338.
317. Pillay, K.; Cukrowska, E.; Coville, N., Multi-walled carbon nanotubes as adsorbents for the removal of parts per billion levels of hexavalent chromium from aqueous solution. *J. Hazard. Mater.* **2009,** *166*, 1067-1075.
318. Sakulthaew, C.; Chokejaroenrat, C.; Poapolathep, A.; Satapanajaru, T.; Poapolathep, S., Hexavalent chromium adsorption from aqueous solution using carbon nano-onions (CNOs). *Chemosphere* **2017,** *184*, 1168-1174.
319. Wu, Y.; Luo, H.; Wang, H.; Wang, C.; Zhang, J.; Zhang, Z., Adsorption of hexavalent chromium from aqueous solutions by graphene modified with cetyltrimethylammonium bromide. *J. Colloid. Interface Sci.* **2013,** *394*, 183-191.
320. Hu, J.; Chen, C.; Zhu, X.; Wang, X., Removal of chromium from aqueous solution by using oxidized multiwalled carbon nanotubes. *J. Hazard. Mater.* **2009,** *162*, 1542-1550.
321. Karthikeyan, T.; Rajgopal, S.; Miranda, L. R., Chromium (VI) adsorption from aqueous solution by Hevea Brasilinesis sawdust activated carbon. *J. Hazard. Mater.* **2005,** *124*, 192-199.
322. Jung, C.; Heo, J.; Han, J.; Her, N.; Lee, S.-J.; Oh, J.; Ryu, J.; Yoon, Y., Hexavalent chromium removal by various adsorbents: powdered activated carbon, chitosan, and single/multi-walled carbon nanotubes. *Sep. Purif. Technol.* **2013,** *106*, 63-71.
323. Qiu, B.; Xu, C.; Sun, D.; Wei, H.; Zhang, X.; Guo, J.; Wang, Q.; Rutman, D.; Guo, Z.; Wei, S., Polyaniline coating on carbon fiber fabrics for improved hexavalent chromium removal. *RSC Adv.* **2014,** *4*, 29855-29865.
324. Ihsanullah; Al-Khaldi, F. A.; Abu-Sharkh, B.; Abulkibash, A. M.; Qureshi, M. I.; Laoui, T.; Atieh, M. A., Effect of acid modification on adsorption of hexavalent chromium (Cr (VI)) from aqueous solution by activated carbon and carbon nanotubes. *Desalin. Water Treat.* **2016,** *57*, 7232-7244.

325. Welch, C. M.; Nekrassova, O.; Compton, R. G., Reduction of hexavalent chromium at solid electrodes in acidic media: reaction mechanism and analytical applications. *Talanta* **2005,** *65*, 74-80.
326. Patterson, R. R.; Fendorf, S.; Fendorf, M., Reduction of hexavalent chromium by amorphous iron sulfide. *Environ. Sci. Technol.* **1997,** *31*, 2039-2044.
327. Cheung, K.; Gu, J.-D., Mechanism of hexavalent chromium detoxification by microorganisms and bioremediation application potential: a review. *Int. Biodeterior. Biodegradation* **2007,** *59*, 8-15.
328. Lv, X.; Xu, J.; Jiang, G.; Xu, X., Removal of chromium (VI) from wastewater by nanoscale zero-valent iron particles supported on multiwalled carbon nanotubes. *Chemosphere* **2011,** *85*, 1204-1209.
329. Zhu, J.; Wei, S.; Gu, H.; Rapole, S. B.; Wang, Q.; Luo, Z.; Haldolaarachchige, N.; Young, D. P.; Guo, Z., One-pot synthesis of magnetic graphene nanocomposites decorated with core@ double-shell nanoparticles for fast chromium removal. *Environ. Sci. Technol.* **2011,** *46*, 977-985.
330. Shakoori, A.; Makhdoom, M.; Haq, R., Hexavalent chromium reduction by a dichromate-resistant gram-positive bacterium isolated from effluents of tanneries. *Appl. Microbiol. Biotechnol.* **2000,** *53*, 348-351.
331. Gheju, M.; Iovi, A., Kinetics of hexavalent chromium reduction by scrap iron. *J. Hazard. Mater.* **2006,** *135*, 66-73.
332. Chuang, S.-M.; Ya, V.; Feng, C.-L.; Lee, S.-J.; Choo, K.-H.; Li, C.-W., Electrochemical Cr (VI) reduction using a sacrificial Fe anode: Impacts of solution chemistry and stoichiometry. *Sep. Purif. Technol.* **2018,** *191*, 167-172.
333. Li, S.; Hu, Z.; Xie, S.; Liu, H.; Liu, J., Removal of Cr (VI) From Electroplating Industry Effluent via Electrochemical Reduction. *Int. J. Electrochem. Sci* **2018,** *13*, 655-663.
334. Rodríguez, F. J.; Gutiérrez, S.; Ibanez, J. G.; Bravo, J. L.; Batina, N., The efficiency of toxic chromate reduction by a conducting polymer (polypyrrole): influence of electropolymerization conditions. *Environ. Sci. Technol.* **2000,** *34*, 2018-2023.
335. Chaudhary, A. J.; Goswami, N. C.; Grimes, S. M., Electrolytic removal of hexavalent chromium from aqueous solutions. *J. Chem. Technol. Biotechnol.* **2003,** *78*, 877-883.
336. Golder, A. K.; Chanda, A. K.; Samanta, A. N.; Ray, S., Removal of hexavalent chromium by electrochemical reduction–precipitation: investigation of process performance and reaction stoichiometry. *Sep. Purif. Technol.* **2011,** *76*, 345-350.
337. Gao, P.; Chen, X.; Shen, F.; Chen, G., Removal of chromium (VI) from wastewater by combined electrocoagulation–electroflotation without a filter. *Sep. Purif. Technol.* **2005,** *43*, 117-123.

338. Xia, L.; Akiyama, E.; Frankel, G.; McCreery, R., Storage and release of soluble hexavalent chromium from chromate conversion coatings equilibrium aspects of Cr VI concentration. *J. Electrochem. Soc.* **2000,** *147*, 2556-2562.
339. Yadav, M.; Xu, Q., Catalytic chromium reduction using formic acid and metal nanoparticles immobilized in a metal–organic framework. *Chem. Commun.* **2013,** *49*, 3327-3329.
340. Leita, L.; Margon, A.; Pastrello, A.; Arčon, I.; Contin, M.; Mosetti, D., Soil humic acids may favour the persistence of hexavalent chromium in soil. *Environ. Pollut.* **2009,** *157*, 1862-1866.
341. Rhee, S.; Kang, M.; Kim, H.; Moon, C., Removal of aquatic chromate ion involving rehydration reaction of calcined layered double hydroxide (Mg-Al-CO3). *Environ. Technol.* **1997,** *18*, 231-236.
342. Duan, W.; Chen, G.; Chen, C.; Sanghvi, R.; Iddya, A.; Walker, S.; Liu, H.; Ronen, A.; Jassby, D., Electrochemical removal of hexavalent chromium using electrically conducting carbon nanotube/polymer composite ultrafiltration membranes. *J. Memb. Sci.* **2017,** *531*, 160-171.
343. Douglas, A.; Carter, R.; Li, M.; Pint, C. L., Toward Small-Diameter Carbon Nanotubes Synthesized from Captured Carbon Dioxide: Critical Role of Catalyst Coarsening. *ACS Appl. Mater. Interfaces* **2018,** *10*, 19010-19018.
344. Ren, J.; Licht, S., Tracking airborne CO 2 mitigation and low cost transformation into valuable carbon nanotubes. *Sci. Rep.* **2016,** *6*, 27760.
345. Assegie, A. A.; Cheng, J.-H.; Kuo, L.-M.; Su, W.-N.; Hwang, B.-J., Polyethylene oxide film coating enhances lithium cycling efficiency of an anode-free lithium-metal battery. *Nanoscale* **2018,** *10*, 6125-6138.
346. Qian, J.; Adams, B. D.; Zheng, J.; Xu, W.; Henderson, W. A.; Wang, J.; Bowden, M. E.; Xu, S.; Hu, J.; Zhang, J. G., Anode-free rechargeable lithium metal batteries. *Adv. Funct. Mater.* **2016,** *26*, 7094-7102.
347. Cohn, A. P.; Muralidharan, N.; Carter, R.; Share, K.; Pint, C. L., Anode-free sodium battery through in situ plating of sodium metal. *Nano Lett.* **2017,** *17*, 1296-1301.
348. Li, M. Y.; Carter, R.; Douglas, A.; Oakes, L.; Pint, C. L., Sulfur Vapor-Infiltrated 3D Carbon Nanotube Foam for Binder-Free High Areal Capacity Lithium-Sulfur Battery Composite Cathodes. *ACS Nano* **2017,** *11*, 4877-4884.
349. Muralidharan, N.; Afolabi, J.; Share, K.; Li, M.; Pint, C. L., A Fully Transient Mechanical Energy Harvester. *Adv. Mater. Technol.* **2018**, 1800083.
350. Muralidharan, N.; Brock, C. N.; Cohn, A. P.; Schauben, D.; Carter, R. E.; Oakes, L.; Walker, D. G.; Pint, C. L., Tunable Mechanochemistry of Lithium Battery Electrodes. *ACS Nano* **2017,** *11*, 6243-6251.
351. Muralidharan, N.; Carter, R.; Oakes, L.; Cohn, A. P.; Pint, C. L., Strain engineering to modify the electrochemistry of energy storage electrodes. *Sci. Rep.* **2016,** *6*, 27542.

352. Kim, S.; Choi, S. J.; Zhao, K.; Yang, H.; Gobbi, G.; Zhang, S.; Li, J., Electrochemically driven mechanical energy harvesting. *Nat. Commun.* **2016,** *7*, 10146.
353. Cannarella, J.; Arnold, C. B., Toward Low-Frequency Mechanical Energy Harvesting Using Energy-Dense Piezoelectrochemical Materials. *Adv. Mater.* **2015,** *27*, 7440-7444.
354. Oakes, L.; Cohn, A. P.; Westover, A. S.; Pint, C. L., Electrophoretic stabilization of freestanding pristine graphene foams with carbon nanotubes for enhanced optical and electrical response. *Mater. Lett.* **2015,** *159*, 261-264.
355. Oakes, L.; Hanken, T.; Carter, R.; Yates, W.; Pint, C. L., Roll-to-Roll Nanomanufacturing of Hybrid Nanostructures for Energy Storage Device Design. *ACS Appl. Mater. Interfaces* **2015,** *7*, 14201-14210.